# Title: Uncovering molecular iron compounds in the living human brain.

**Authors:** Shir Filo[1], Rona Shaharabani[1], Daniel Bar Hanin[1], Masha Adam[1], Eliel Ben-David[2], Hanan Schoffman[3], Nevo Margalit[4], Naomi Habib[1], Tal Shahar[3,4†], Aviv Mezer[1†]

**Affiliations:**

[1]The Edmond and Lily Safra Center for Brain Sciences, The Hebrew University of Jerusalem, Israel;

[2]The Department of Radiology; [3]The Laboratory of Molecular Neuro-Oncology and [4]The Department of Neurosurgery, Shaare Zedek Medical Center, Faculty of Medicine, The Hebrew University of Jerusalem, Israel

† Equal contributions.

**Abstract:** Strict iron regulation is essential for normal brain function. The main iron compounds responsible for iron homeostasis, transferrin and ferritin, are distributed heterogeneously across the brain and are implicated in aging, neurodegenerative diseases and cancer. However, non-invasive discrimination between iron compounds, such as transferrin and ferritin, remains a challenge. We present a novel magnetic resonance imaging (MRI) technology for mapping of iron compounds in the living brain (the r1-r2* relaxivity). The specificity of the r1-r2* relaxivity to the presence of ferritin and transferrin is validated by both bottom-up and top-down approaches, incorporating *in vitro*, *in vivo* and *ex vivo* analyses. *In vitro*, our MRI approach reveals the distinct paramagnetic properties of ferritin and transferrin. In the *in vivo* human brain, we validate our approach against *ex vivo* iron compounds quantification and gene expression. Our approach predicts the transferrin-ferritin fraction across brain regions and in aging. It reveals brain tumors' iron homeostasis, and enhances the distinction between tumor tissue and non-pathological tissue without contrast agents. Therefore, our approach may allow for non-invasive research and diagnosis of iron homeostasis in living human brains.

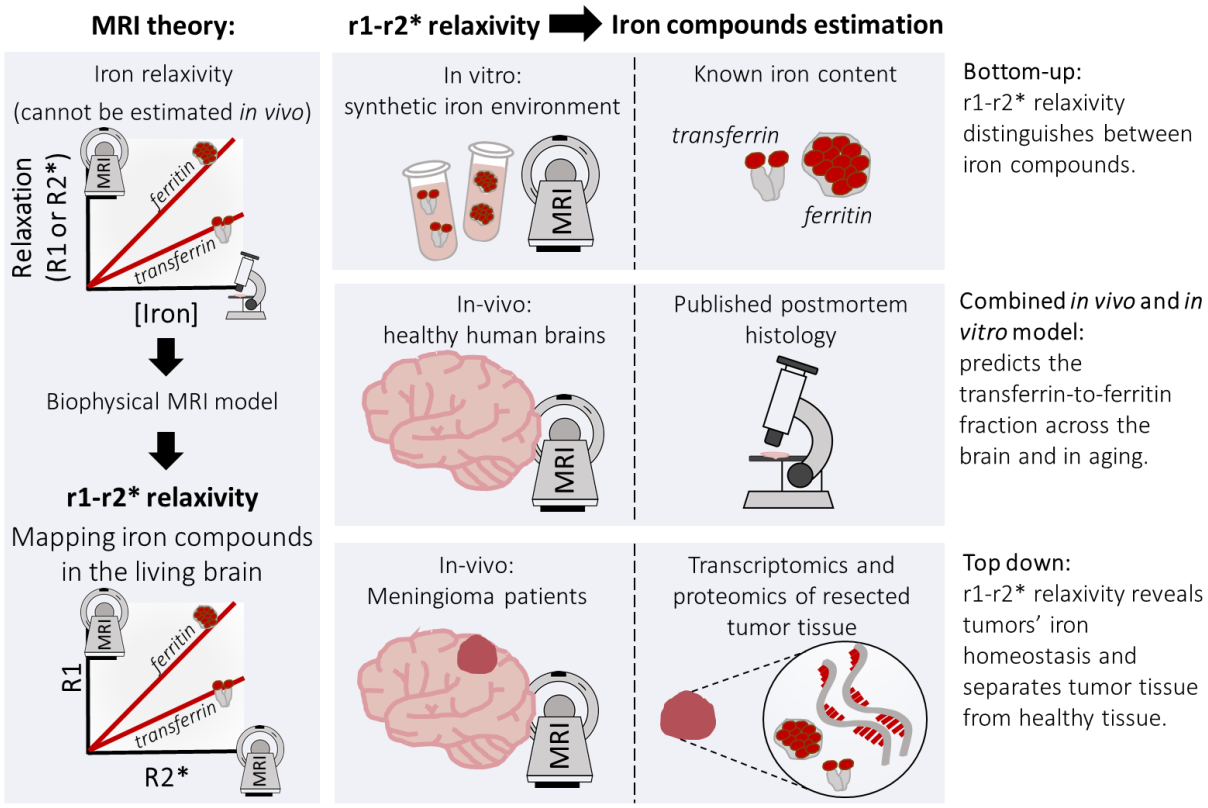


***Graphical abstract:*** *Uncovering molecular iron compounds in the living human brain.*

## Introduction:

Iron is the most abundant trace element in the human body[1]. It participates in fundamental processes such as oxygen transport, cellular metabolism, myelin formation and the synthesis of neurotransmitters[1–4]. Therefore, strict iron regulation is essential for maintaining normal brain function. The two iron compounds most involved in iron homeostasis are transferrin and ferritin[3]. Transferrin, the main iron transport protein, carries iron from the blood into brain tissue, while ferritin, the main iron storage protein, stores excess iron atoms. Importantly, these two iron-binding proteins are distributed heterogeneously between cell types and across brain regions[3,5–7].

Transferrin and ferritin play a major role in normal aging and in neurodegenerative diseases such as Parkinson's disease (PD), Alzheimer's disease (AD), multiple sclerosis, Friedreich's ataxia, aceruloplasminaemia, neuroferritinopathy, Huntington's disease, and restless legs syndrome[1,2,5–10]. When iron concentrations exceed the capacity of iron-binding proteins, this can lead to oxidative stress and cellular damage[10]. For example, the ratio of transferrin to iron, which reflects iron mobilization capacity, differs between elderly controls and patients (AD and PD) in a brain-region–dependent manner[7]. In addition, specifically in the substantia nigra and the locus coeruleus, reduction in neuromelanin-iron complexes is considered a biomarker for PD and AD[11,12].

Disruptions in the homeostasis of iron compounds, including ferritin and transferrin, also have been reported in cancer cells[13,14]. Tumor cell proliferation requires a modulated expression of proteins involved in iron uptake. In addition, iron may affect the immune surveillance of tumors[15]. Therefore, the availability of iron in the tumor cells' microenvironment may affect their survival and growth rate, and subsequently the course of the disease. For example, meningioma brain tumors[16], compared to non-pathological tissue, were shown to contain a higher concentration of ferrimagnetic particles and abnormal expression of iron-related genes[17,18]. These findings suggest there are detectable differences in iron homeostasis between brain tumors and normal brain tissue.

The extensive implications of impaired iron homeostasis in normal aging, neurodegeneration and carcinogenesis suggest that assessment of different iron compounds in the living brain would be highly valuable for diagnosis, therapeutic monitoring, and understanding pathogenesis of diseases[4]. Iron's paramagnetic properties make magnetic resonance imaging (MRI) a perfect candidate for non-invasive estimation of iron content in brain tissue. In particular, iron is a major contributor to the longitudinal and effective transverse relaxation rates, R1 and R2* respectively[19–22]. These relaxation rates can be measured using quantitative MRI (qMRI) techniques[23–26]. Indeed, *in vivo* studies often use these qMRI measurements as a proxy for iron presence in brain tissue[21,27–31]. However, a major limitation of current MRI techniques is that they do not have the sensitivity to discriminate between different molecular compounds of iron in the brain, such as ferritin and transferrin[4].

Early *in vitro* and postmortem works suggest that different iron environments can be distinguished by their iron relaxivity[31–34]. The iron relaxivity is defined as the dependency of MR relaxation rates on the iron concentration[35]. It was shown that iron relaxivity varies with the specific environment in which the iron resides[31–34]. However, a major limitation of this approach is that it requires direct estimation of the tissue iron concentration, which can only be acquired *in vitro* or postmortem. Therefore, until now the phenomenon of iron relaxivity could not be studied in living humans.

Here we propose an *in vivo* iron relaxivity approach for mapping different iron compounds in the brain. Our approach fully relies on MRI parameters, and does not require estimation of the tissue iron concentration, thereby allowing for the first time non-invasive measurements of transferrin and ferritin in the living brain. We exploit the distinct iron relaxivities of the MR relaxation rates, R1 and R2*, to construct a biophysical model of their linear interdependency, which we label the r1-r2* relaxivity. Using the r1-r2* relaxivity, we argue that the distinct iron relaxivity of different iron compounds, such as transferrin and ferritin, can be estimated *in vivo*. We confirm this hypothesis based on a novel validation framework. First, we used a bottom-up strategy in which we evaluated the r1-r2* relaxivity of different iron compounds *in vitro*. Next, we used a top-down strategy in which we measured the r1-r2* relaxivity in human brains *in vivo* and compared it to *ex vivo* quantification of iron compounds and gene expression, both at the group and the

single-subject levels. We tested the ability of our approach to enhance the distinction between tumor tissue and non-pathological tissue, and to reveal the state of iron homeostasis in tumors. In the healthy brain, we constructed a biophysical model integrating both *in vivo* and *in vitro* measurements of the r1-r2* relaxivity. Our model accurately predicted the distribution of ferritin relative to transferrin across brain regions and in aging. Therefore, we provide a well-validated MRI framework with great implications for the non-invasive research and diagnosis of normal and impaired iron homeostasis in living human brains (see graphical abstract).

## Results:

### *The theoretical basis for the r1-r2* relaxivity.*

The iron relaxivity of a specific iron compound is defined based on the linear relationship between the relaxation rates (R1 and R2*) and the iron compound's concentration ($[IC]$)[35]:

$$R_1 = r_{(1,IC)}[IC] + c_1 \qquad R_2^* = r_{(2,IC)}[IC] + c_2$$

The slopes of these linear dependencies, $r_{(1,IC)}$ and $r_{(2,IC)}$, represent the iron relaxivities of R1 and R2*, which were shown to have different values for different iron environments[31–34]. $c_1$ and $c_2$ are constants. Notably, the iron relaxivities require estimation of the iron compound's concentration ($[IC]$), thereby limiting this approach to *in vitro* and *ex vivo* studies.

Here we propose a theory which advances the iron relaxivity model and provides *in vivo* iron relaxivity measurements for identifying different iron compounds in the brain. We take advantage of the fact that R1 and R2* are governed by different molecular and mesoscopic mechanisms[36–38], and therefore each of them may have a distinct iron relaxivity in the presence of paramagnetic substances. Based on our theoretical framework ("*In vivo* iron relaxivity model" in Methods), the linear dependency of R1 on R2* can be described by the following equation:

$$R_1 = \frac{r_{(1,IC)}}{r_{(2,IC)}} * R_2^* + constant$$

The slope of this linear dependency ($\frac{r_{(1,IC)}}{r_{(2,IC)}}$) represents the ratio of the iron relaxivities, $r_1$ and $r_2^*$, which are sensitive to the molecular compound of iron. Therefore, we define this MRI-based

slope as the r1-r2* relaxivity ($\frac{r_{(1,IC)}}{r_{(2,IC)}}$) and hypothesize it reveals the distinct properties of different iron compounds.

*In vitro validation for the sensitivity of the iron relaxivity to molecular iron compounds.*

Before implementing this approach in the living human brain, we validated our theory by manufacturing *in vitro* samples of different iron compounds in a synthetic cellular membrane environment. These samples were scanned in the MRI to verify that different iron compounds have different iron relaxivities. We then tested whether our r1-r2* relaxivity theory could reveal these different relaxivities.

We prepared samples of transferrin and ferritin in different cellular-like environments (free in water or adjacent to liposomes and proteins, to achieve physiological iron concentrations the transferrin concentrations are higher than the ones measured *in vivo*[3,4]). These highly controlled synthetic iron samples were scanned for R1 and R2* mapping. We found that both R1 and R2* increased with the concentration of iron compounds (**Figure 1a-b**). The rate of this increase, defined as the iron relaxivity, was different for different iron compounds (**Figure 1a-c**, $p(ANCOVA)<10^{-50}$). We show that R1 and R2* change both with the type and concentration of iron, thereby making it impossible to distinguish between iron compounds with these measurements. For example, R1 increased with the ferritin concentration, but also was higher for ferritin compared to transferrin (**Figure 1a-b**, **Sup. Figure 1a-b**). Consequently, similar R1 values can be obtained for ferritin and transferrin, depending on their concentrations (**Sup. Figure 1b**). This ambiguity can be resolved by the iron relaxivity, which differentiated ferritin from transferrin, and was consistent when computed over samples with higher or lower concentrations (**Sup. Figure 1c**). Therefore, we find that the iron relaxivity reflects changes in the molecular compound of iron and is independent of the iron concentration.

Since ferritin binds more iron than does transferrin by three orders of magnitude[3], we wanted to exclude the possibility that their different relaxivities were being driven by their different iron ion concentration.

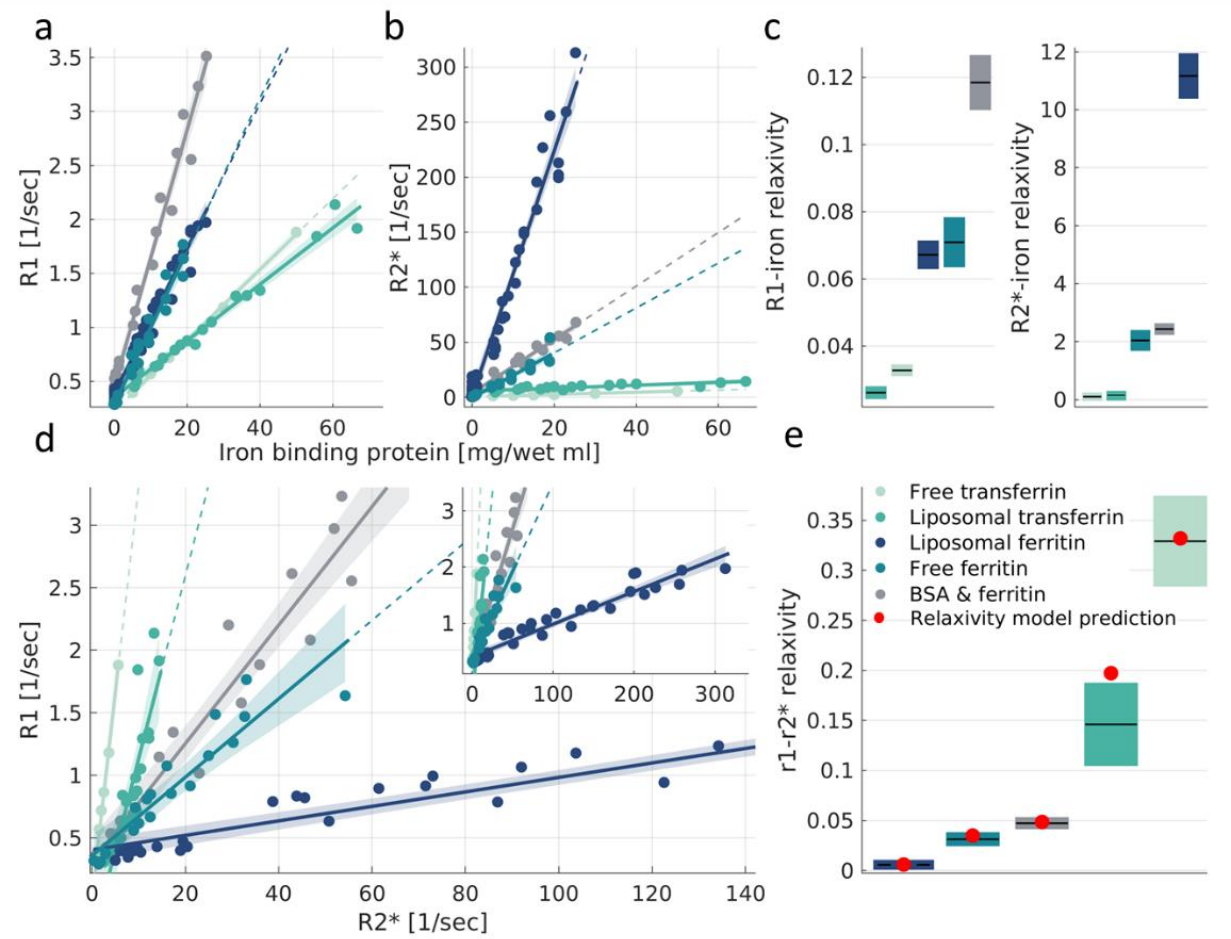


Figure 1: *In vitro validation of the non-invasive framework for assessing brain iron compounds.* ***(a-b)*** *The dependency of R1 and R2* on the iron-binding protein concentration for different iron compounds: free ferritin, liposomal ferritin, bovine serum albumin (BSA)-ferritin mixture, free transferrin and liposomal transferrin. Data points represent samples with varying iron-binding protein concentrations relative to the water fraction ([mg/wet ml]). The linear relationships between relaxation rates and iron-binding protein concentrations are marked by lines. We define the slopes of these lines as the iron relaxivities. Dashed lines represent extrapolation of the linear fit. Shaded areas represent the 95% confidence bounds.* ***(c)*** *The iron relaxivity of R1 and R2* is different for different iron compounds ($p(ANCOVA) < 10^{-50}$). Iron relaxivities are calculated by taking the slopes of the linear relationships shown in (a,b), and are measured in [$sec^{-1}$/(mg/wet ml)]. For each box, the central mark is the iron relaxivity (slope); the box shows the 95% confidence bounds of the linear fit.* ***(d)*** *The dependency of R1 on R2* for different iron compounds. Data points represent samples with varying iron-binding protein concentrations relative to the water fraction. The linear relationships of R1 and R2* are marked by lines. The slopes of these lines are the r1-r2* relaxivities, which do not require iron concentration estimation and therefore can be estimated in vivo. Dashed lines represent extrapolation of the linear fit. Shaded areas represent the 95% confidence bounds. The inset shows a zoom-out of the main figure, presenting the entire range of measured R2* values* ***(e)*** *The r1-r2* relaxivities are different for different iron compounds ($p(ANCOVA) < 10^{-38}$). For each box, the central mark is the r1-r2* relaxivity, and the box shows the 95% confidence bounds of the linear fit. Red dots indicate the successful prediction of the experimental r1-r2* relaxivity from the ratio between the iron relaxivities of R1 and R2* ($\frac{r_{(1,IC)}}{r_{(2,IC)}}$, shown in c). This validates our theoretical in vivo relaxivity model.*

We estimated the iron ion concentrations for these two iron compounds (see Methods), and verified that ferritin and transferrin indeed have different iron relaxivities even when accounting for the discrepancies in iron binding (**Sup. Section 1**).

*The r1-r2* relaxivity reveals the distinct iron relaxivities of different iron compounds.*

In agreement with previous findings[31–34], our *in vitro* experiments indicate that iron relaxivity can be used to identify different iron compounds. While the iron relaxivity cannot be estimated *in vivo*, as it requires measurements of iron concentrations, the r1-r2* relaxivity only relies on MRI measurements that can be estimated *in vivo*. Based on our theory, we argue that two iron compounds with different iron relaxivities also should differ in their r1-r2* relaxivities. We validated this hypothesis using synthetic iron-containing samples. As predicted by our theoretical model, iron compounds with different iron-relaxivities had different r1-r2* relaxivities (**Figure 1d-e**, p(ANCOVA )<$10^{-38}$). Notably, as suggested by our theoretical formulation, the r1-r2* relaxivity provides a good MRI approximation for the ratio between the iron relaxivities of R1 and R2* ($\frac{r_{(1,IC)}}{r_{(2,IC)}}$, **Figure 1e**). Similar to the iron relaxivities, the r1-r2* relaxivity is consistent across iron concentrations (**Sup. Figure 1d**). Hence, the r1-r2* relaxivity is specific to individual iron compounds and not to general iron concentration like R1 and R2* by themselves.

In addition, we validated that the r1-r2* relaxivity is sensitive to the paramagnetic properties of iron-binding proteins. We found that apo-transferrin (transferrin which is not bound to iron) has a much smaller r1-r2* relaxivity compared to iron-bound transferrin (p(ANCOVA)<$10^{-8}$; **Sup. Figure 4**). This implies that it is transferrin's paramagnetic properties that induce the r1-r2* relaxivity that we measure.

As brain tissue includes both ferritin and transferrin simultaneously, we calculated the r1-r2* relaxivity of ferritin-transferrin mixtures (**Sup. Section 4.2**). We found that changing the transferrin-ferritin ratio leads to considerable changes in the r1-r2* relaxivity, even in mixtures with low ratio of transferrin compared to ferritin as in the brain[3]. Importantly, these changes were above the detection limit of the *in vitro* r1-r2* relaxivity measurement (**Sup. Figure 8**).

Taken together, these results validate our theory, indicating that the r1-r2* relaxivity can be used to measure iron relaxivity *in vivo* for exposing the distinct paramagnetic properties of different iron compounds.

Other than iron, another major contributor to R1 and R2* is the myelin content[4,19,25,29,39–44]. Since myelin is composed mainly of lipids, we tested the effect of the myelin fraction on the iron relaxivity by varying the liposomal fractions in our *in vitro* experiments. We found that the r1-r2* relaxivities are stable for different liposomal fractions and lipid types (for more details see **Sup. section 2**). These results highlight the specificity of the r1-r2* relaxivity to differences in the compound of iron, unlike the ambiguous measurements of R1 or R2* independently.

***The r1-r2* relaxivity provides a new MRI contrast in the in vivo human brain.***

Following the *in vitro* validation, we used the r1-r2* relaxivity to measure the *in vivo* iron relaxivity in the living human brain. For this aim we calculated the linear dependency of R1 on R2* across voxels of different anatomically-defined ROIs (see "r1-r2* relaxivity computation for ROIs in the human brain" in Methods). We found distinct r1-r2* relaxivities for different brain regions (**Figure 2a**). This indicates a heterogeneous distribution of the *in vivo* iron relaxivity across the brain, which is consistent across healthy subjects (age 27±2 years, N=21, **Figure 2b**) and is reproducible in scan-rescan experiments (**Sup. Figure 9**). In agreement with our *in vitro* results, which indicated that the r1-r2* relaxivity provides different information compared to R1 and R2*, in the *in vivo* human brain we find that the r1-r2* relaxivity produces a new contrast, statistically different from R1 and R2* (**Figure 2b-c**; $p<0.05$ for the two-sample Kolmogorov–Smirnov test comparing the r1-r2* relaxivity distribution to R1, and $p<0.001$ comparing it to R2*). While the r1-r2* relaxivity is calculated for an anatomically-defined ROI in the brain, a demonstration of a voxel-wise r1-r2* relaxivity map based on each voxel's local neighborhood, as well as comparison to the R1 and R2* contrasts, can be found in **Sup. Section 3**.

The sensitivity of R1 and R2* to the myelin content is known to produce contrasts that are governed mainly by the differences between white-matter and gray-matter tissues[4,19,25,29,39–43]. As expected, we find a strong distinction between gray-matter and white-matter regions in R1

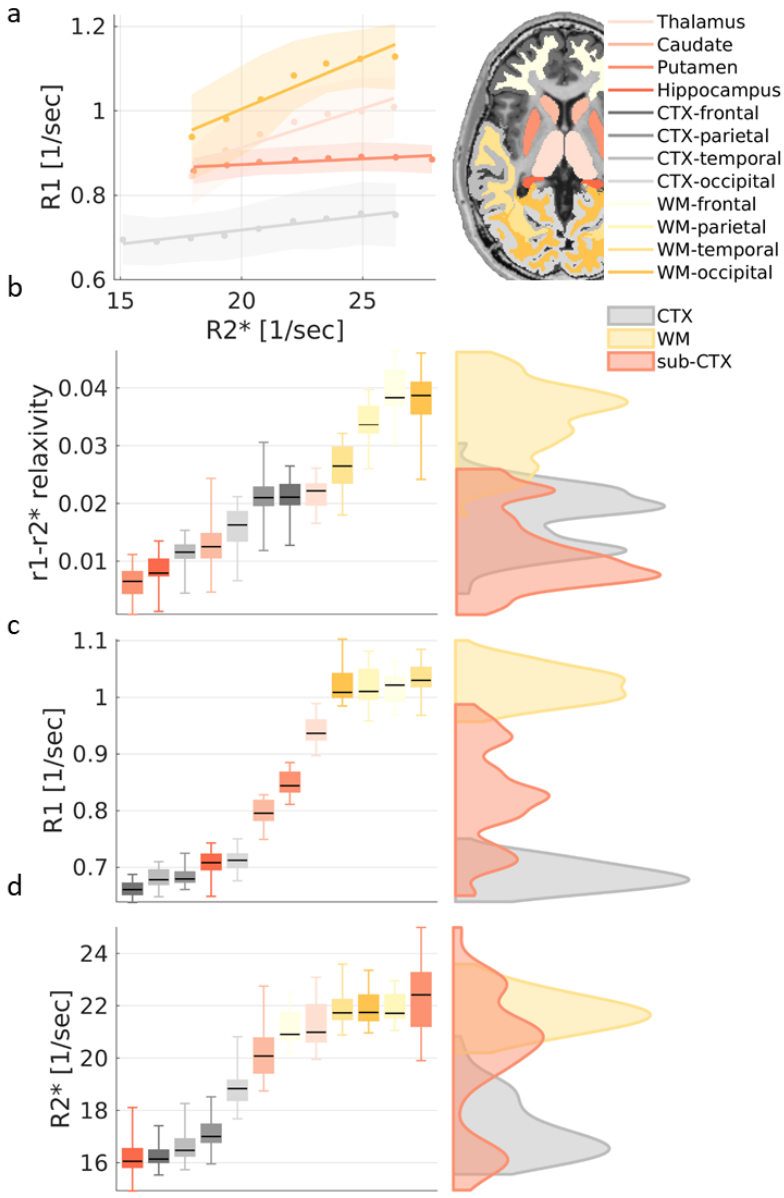


Figure 2: The *in vivo r1-r2* relaxivity provides a novel contrast in the brain.* ***(a)*** *The dependency of R1 on R2* in four representative brain regions (WM-occipital, CTX-occipital, Thalamus & Putamen) of a single subject. R2* and R1 were binned (dots represent the median; shaded areas represent the mean absolute deviation), and a linear fit was calculated. The slopes of the linear fit represent the dependency of R1 on R2* (r1-r2* relaxivity) and vary across brain regions.* ***(b)*** *The r1-r2* relaxivity across the brain. Left: the reliability of the method in different brain regions as observed by the variation in the r1-r2* relaxivity across normal subjects (age 27±2, N=21). The 25th, 50th and 75th percentiles and extreme data points are shown for each box. Right: the contrast of the r1-r2* relaxivity across the brain. Red, yellow and gray distributions represent the values of the r1-r2* relaxivities in sub-cortical (sub-CTX), white-matter (WM) and cortical (CTX) brain regions, respectively.* ***(c-d)*** *Similar analyses for R1 and R2* values, in which the gray-matter vs. white-matter contrast is much more dominant compared to the r1-r2* relaxivity. Hence, the r1-r2* relaxivity provides new information compared to R1 and R2*, beyond the WM-GM. Results in this entire figure are for ROIs in the left hemisphere. WM=white-matter, CTX=cortex.*

and R2* values (**Figure 2c-d**). However, the contrast of the r1-r2* relaxivity across the brain shows a novel spatial pattern and reveals differences between brain regions beyond the typical white matter—gray matter differentiation. For example, we found the temporal, parietal and occipital white-matter regions to be indistinguishable in terms of their R1 and R2* values (p(ANOVA)>0.4), but these regions were separable based on their different r1-r2* relaxivities (p(ANOVA)<$10^{-10}$, **Sup. Figure 11**). Another evidence for the fact that the r1-r2* relaxivity is less sensitive to the myelin content compared to R1 and R2* comes from comparisons to in-vivo myelin markers. The qMRI measurements of the macromolecular tissue volume (MTV)[45], which was shown to approximate the myelin content [46–50], and mean diffusivity (MD), which is sensitive to myelin characteristics[51], are both highly correlated with R1 and R2* but are not significantly correlated with the r1-r2* relaxivity (**Sup. Figure 12-Sup. Figure 13**). In order to further investigate the effect of myelin on the r1-r2* relaxivity, we performed a set of numerical simulations in which we consider the contributions of multiple brain tissue components to the relaxivity measurement (**Sup. Section 4.3**). As in the *in vivo* brain, we found that changes in the myelin concentration substantially affect the simulated measurements of R1 and R2*. However, myelin-related changes were not the main component governing the simulated measurement of the r1-r2* relaxivity, and in simulations of physiological conditions they could not explain the variability in the r1-r2* relaxivity across the brain.

***The r1-r2* relaxivity enhances the distinction between tumor tissues and non-pathological tissue.***

While the r1-r2* relaxivity forms a unique pattern of changes across the brain, it needs to be established that this contrast contains meaningful information, that can complement the contrasts of R1 and R2*. For this aim, we evaluated the MRI contrast between pathological and normal-appearing tissues of patients with meningioma brain tumors (N=18, **Figure 3a-b**). The diagnosis of brain tumors and their delineation from the surrounding non-pathological tissue is routinely performed using contrast-enhanced MRI, which requires the injection of an external gadolinium (Gd)-based contrast agent with paramagnetic properties[52]. As expected, when using Gd-based contrast, tumor tissue was distinct from white-matter and gray-matter tissues (**Figure 3c**, Cohen's d=1.4, p<$10^{-4}$ for tumor-gray matter; Cohen's d=1.18, p<$10^{-3}$ for tumor-white matter). Recently renewed concerns about the long-term safety of Gd-based agents[53,54],

highlight the need for Gd-free MRI techniques that can serve as safe alternatives[55]. However, without Gd-agent injection, both for R1 and R2* values the biggest effect size was observed between white-matter and gray-matter tissues, with no significant difference between gray-matter and tumor tissues (Cohen's $d<0.45$, $p>0.08$ for R1, Cohen's $d<0.11$, $p>0.65$ for R2*, **Figure 3d-e**). This demonstrates the poor performances of R1 and R2* in Gd-free tumor tissue delineation. Importantly, the r1-r2* relaxivity greatly enhanced the contrast between tumor tissue and non-pathological tissue, without contrast agent injection (**Figure 3f**, Cohen's $d=1.5$, $p<10^{-5}$ for tumor-gray matter; Cohen's $d=4.32$, $p<10^{-11}$ for tumor-white matter). This Gd-free enhancement was comparable in size to the effect of Gd-based contrast. These results emphasize the improved sensitivity of the r1-r2* relaxivity to the unique tumor microenvironment, which may have wide clinical implications as a safe alternative for contrast agents' injections.

***The r1-r2* relaxivity is associated with unique biological pathways and gene expression profiles.***

To further examine how the biological information obtained by the r1-r2* relaxivity differs from the information contained in R1 and R2*, we examined the associations of these *in vivo* MRI measurements with underlying gene-expression profiles for the same tissue. To this end, we analyzed cases in which the MRI scans of the meningioma patients were followed by surgical interventions, to obtain matching resected tumor tissue samples that we profiled by bulk RNA-sequencing. For these tumor samples (N=17), we performed an unbiased analysis to identify genes and molecular pathways that could be linked with the *in vivo* measured MRI parameters. For each gene we calculated the correlation between the expression level and the *in vivo* MRI measurements (r1-r2* relaxivity, R1 and R2*) across patients. We then performed gene set enrichment analysis (GSEA)[56,57] to identify molecular functions that are significantly associated with each MRI measurement. In total, we found 9, 55 and 59 significantly enriched gene sets for R1, R2* and the r1-r2* relaxivity, respectively ($p<0.01$ after familywise error rate (FWER) correction; **Sup. Table 1**). These gene sets define genes linked to a specific biological pathway. Almost half of the significant gene sets were exclusively associated with the r1-r2* relaxivity, and not with R1 or R2* (**Sup. Figure 14**). The enrichment score represents the degree to which the genes within a set were positively or negatively correlated with MRI measurements. In examining

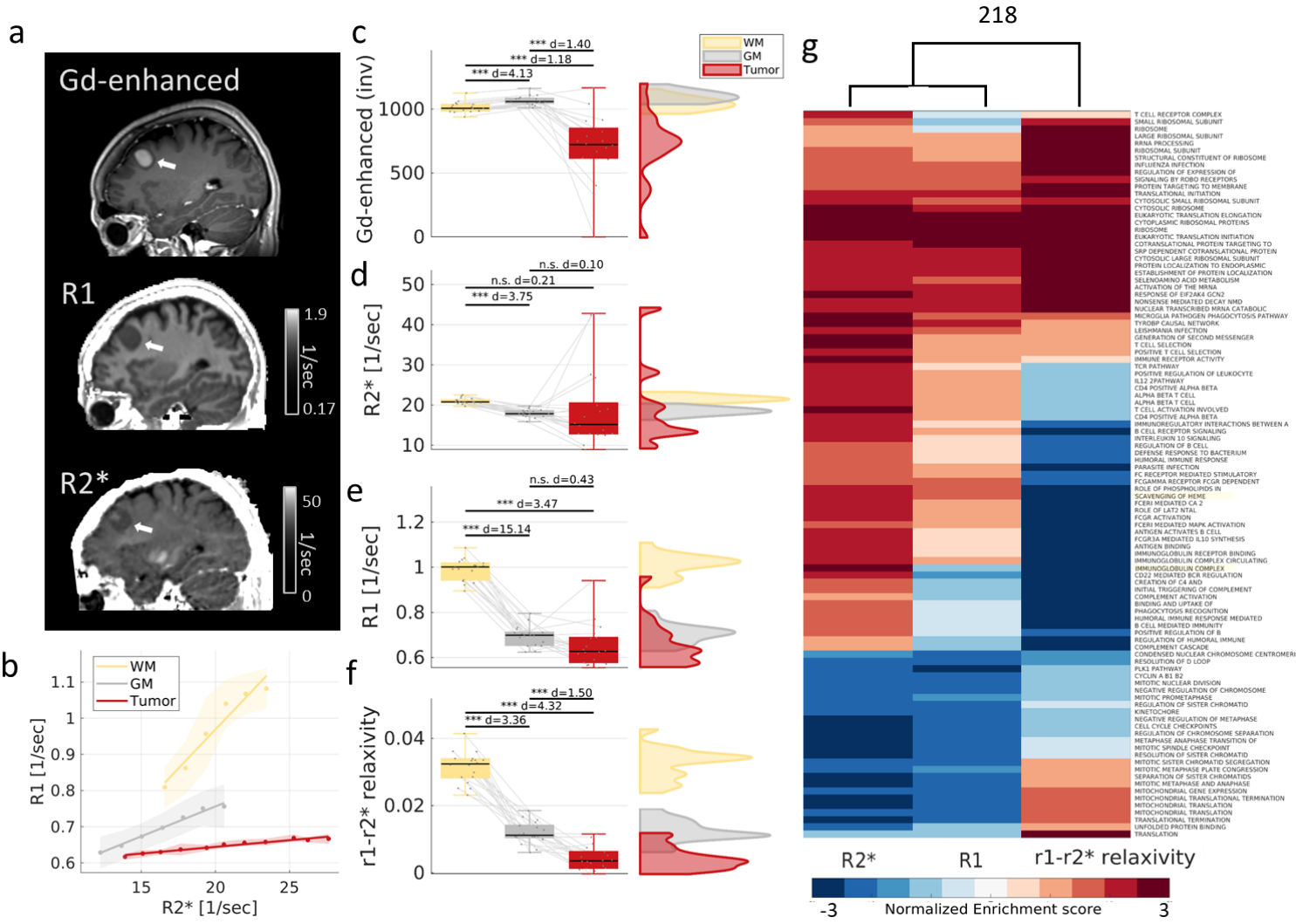


**Figure 3: Application of the r1-r2* relaxivity on meningioma brain tumors. (a)** From top to bottom: Gd-enhanced T1-weighted image, R1 map and R2* map in a representative subject with a meningioma brain tumor (white arrow). **(b)** The dependency of R1 on R2* (r1-r2* relaxivity) for the white matter (WM, frontal), gray matter (GM, frontal) and tumor tissue of the same subject. Tumor tissue exhibits distinct r1-r2* relaxivity relative to non-pathological tissue, as evident by the slopes of the R1-R2* linear dependency. **(c)** The Gd-enhanced contrast (inverted for visualization, a.u.) between the white matter (WM), gray matter (GM) and tumor tissues (Tumor). Left: each box shows the variation in the Gd-enhanced T1-weighted contrast across patients (N=18) for each of the three tissue categories (colors). The 25th, 50th and 75th percentiles and extreme data points are shown. The d-values represent the effect size (Cohen's d) of the differences between tissue types, and the significance level is based on a t-test. Gray lines extend between Gd-enhanced T1-weighted values of the same patient. Right: the distribution of the Gd-enhanced T1-weighted values between WM, GM and tumor tissue across patients. Estimates in non-pathological tissues are for the tumor-free hemisphere. The Gd-enhanced contrast was inverted for visualization purposes. **(d-f)** A similar analysis for R2*, R1 and the r1-r2* relaxivity. Only the r1-r2* relaxivity produces significant differences between tumor and GM tissues without contrast agents **(g)** Gene set enrichment analysis for the correlation of MRI with gene expression. Rows show significant biological pathways, columns represent R1, R2* and the r1-r2* relaxivity. The dendrogram shows hierarchical clustering of the normalized enrichment scores. The r1-r2* relaxivity clustered separately from R1 and R2* and is therefore enriched for unique biological pathways. The two most enriched pathways for the r1-r2* relaxivity are highlighted in yellow. *p<0.05; **p<0.01; ***p<0.001

the associations of MRI measures to biological pathways, as reflected in the enrichment score, we found that the r1-r2* relaxivity clustered separately from R1 and R2* (**Figure 3g**). The clustering results were replicated when performed on the p-value of the enrichment, or on the subset of genes within the top enrichment pathways. This implies that the r1-r2* relaxivity reflects unique cellular and molecular properties, undetectable by the separate analysis of R1 and R2*. Therefore, the *in vivo* r1-r2* relaxivity provides a unique dimension for measuring microstructure and gene expression features across the brain.

The gene enrichment analysis that we performed on resected brain tumors (**Figure 3g**) can provide insights into the biological pathways associated with the r1-r2* relaxivity. The two most enriched pathways for the r1-r2* relaxivity were "immunoglobulin complex" (normalized enrichment score (NES)= -3.62, FWER p-value<0.001; **Sup. Figure 15a**) and "scavenging of heme from plasma" (NES= -3.27, FWER p-value<0.001; **Sup. Figure 15b**). While the former may relate to the response of the immune system to the cancerous process[58,59], the latter involves the absorption of free heme, a source of redox-active iron[60]. This iron-related pathway was not significantly associated with R1 or R2* (p>0.01). Moreover, we examined the main genes involved in iron regulation: transferrin receptor (TFRC), ferritin heavy-chain polypeptide 1 (FTH1) and ferritin light-chain polypeptide (FTL)[61,62]. Both TFRC and FTH1 were included in the subset of genes within the top enrichment pathways for the r1-r2* relaxivity, but were not found to be associated with R1 or R2*. These findings provide evidence at the level of gene-expression for the sensitivity of the r1-r2* relaxivity to iron compounds.

***The r1-r2* relaxivity reveals differences in iron homeostasis between tumor tissues.***

We further validated the sensitivity of the r1-r2* relaxivity to iron compounds at the proteomics level. We compared *in vivo* MRI values of tumor tissue to its transferrin/ferritin ratio which serves as a proxy for iron homeostasis. The levels of transferrin and ferritin were measured in resected tumor samples by western-blot analysis. Neither R1 nor R2* showed significant differences between tumors with low and high transferrin/ferritin ratios (**Figure 4a**). However, the r1-r2* relaxivity was significantly higher for tumors with high transferrin/ferritin ratio compared

to tumors with low transferrin/ferritin ratio ($p<0.01$, **Figure 4a**). Therefore, as established by both gene expression and proteomics analyses, the r1-r2* relaxivity measured *in vivo* detects pathological disruptions in iron homeostasis which were previously only observable *ex vivo*.

***The r1-r2* relaxivity correlates with the transferrin/iron ratio across the brain and in aging.***

Next, we tested the sensitivity of the *r1-r2* relaxivity* to the distribution of iron compounds across the normal brain and in aging. We aggregated previously reported postmortem histological data describing iron, ferritin and transferrin concentrations in different brain regions of young (aged 27-64 years, N>=7) and older (aged 65-88 years, N>=8) adults[5,7,9]. We performed a group-level comparison between these postmortem findings and the *in vivo* r1-r2* relaxivity, which we measured in the same brain regions and age groups (healthy young subjects aged 23-63 years, N=26; older subjects aged 65-77 years, N=13). We excluded the pallidum from this analysis (see **Sup. Section 5**). As expected, R2* was significantly correlated with iron concentration ($R^2$=0.41, p-value(FDR)<0.05; **Sup. Figure 16**). We further estimated the state of iron homeostasis based on the transferrin/iron and ferritin/iron fractions. These measures were not correlated with R2* or R1 (**Figure 4b**). However, the transferrin/iron ratio, serving as a marker for iron mobilization[7], was significantly correlated with the r1-r2* relaxivity across brain regions and age groups ($R^2$=0.59, p-value(FDR)<0.001, **Figure 4b**). Importantly, the r1-r2* relaxivity was not correlated with the absolute ferritin, transferrin or iron concentrations (**Sup. Figure 16-Sup. Figure 18**). This result indicates that the r1-r2* relaxivity is specific to the interplay between iron compounds. Therefore, the r1-r2* relaxivity, unlike R1 and R2*, is sensitive to the transferrin/iron ratio across the brain and can capture the effect of aging on this iron homeostasis marker.

***The r1-r2* relaxivity predicts the transferrin-to-ferritin fraction across the brain and in aging.***

Finally, we modeled the separate contributions of transferrin and ferritin to the observed *in vivo* iron relaxivity in the human brain. We assumed fast-exchange between ferritin and transferrin compartments, and therefore the r1-r2* relaxivity measured in a specific brain region represents the sum of the r1-r2* relaxivities of ferritin and transferrin, weighted by their fraction in this region (Eq. 7 in Methods). If we set the r1-r2* relaxivities of ferritin and transferrin to the ones estimated *in vitro* for liposomal samples (Eq. 9-10 in Methods), we get a model with no free

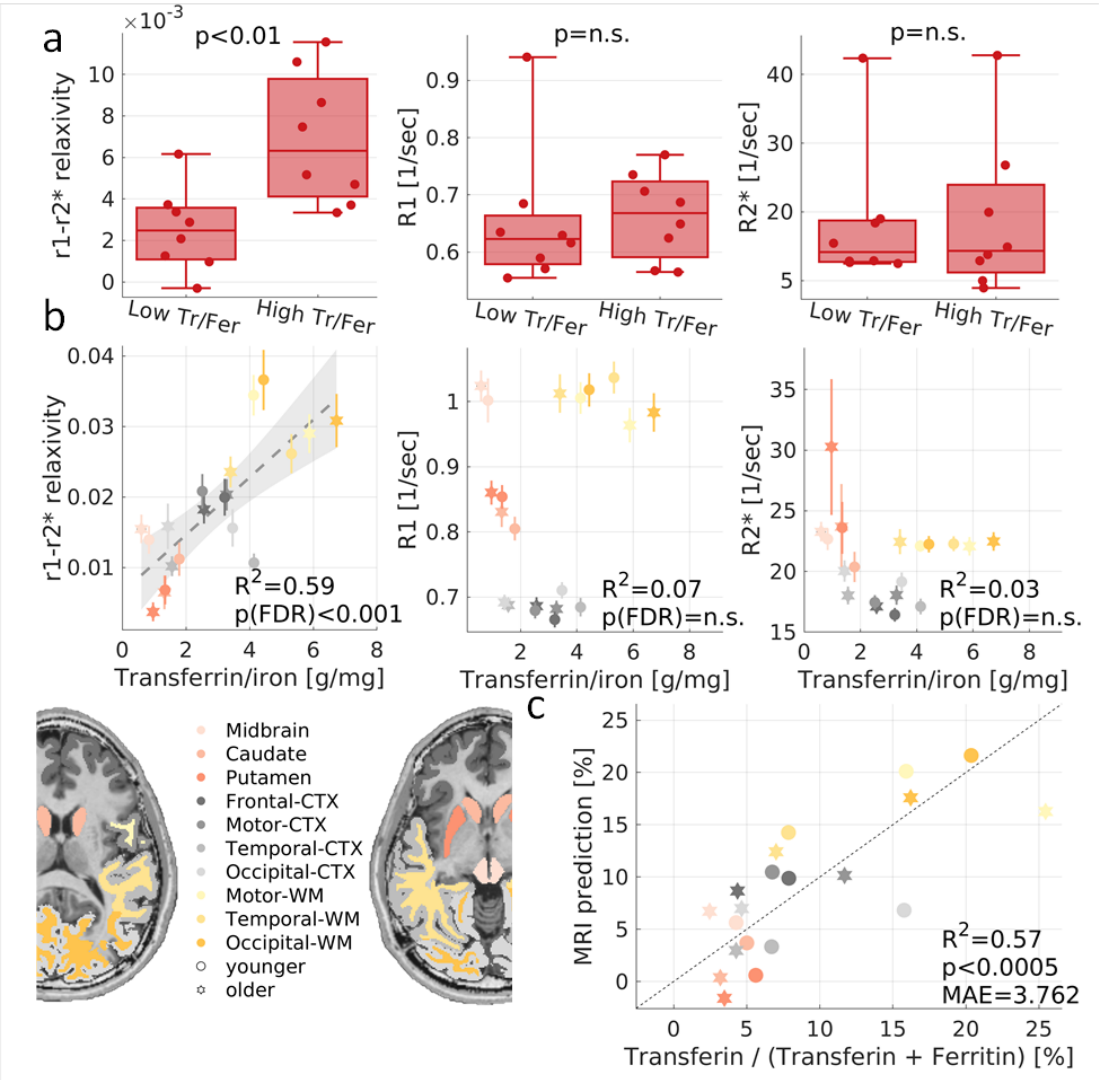


**Figure 4: Validation of the *in vivo* r1-r2* relaxivity against iron compounds estimated on surgical specimens of meningiomas and postmortem brains. (a)** The r1-r2* relaxivity, R1 and R2* measured *in vivo* for tumor tissues (N=16) classified as having either low or high transferrin-to-ferritin ratios (Tf/Fer). Tf/Fer ratio was estimated using western-blot analysis following surgical resection of the tissue. The threshold between groups was set to 1 based on the median across subjects. While R1 and R2* cannot distinguish between the groups with different Tf/Fer ratios, the r1-r2* relaxivities are higher in tissue with a high Tf/Fer ratio. p-values presented are for two-sample t-tests. **(b)** The transferrin/iron ratio (postmortem, from the literature[5,7,9] in different brain regions of younger (aged 27-64 years, N>=7) and older (aged 65-88 years, N>=8) subjects vs. the r1-r2* relaxivity, R1 and R2* measured *in vivo* across younger (aged 23-63 years, N =26) and older (aged 65-77 years, N=13) subjects (different marker shapes) in 10 brain regions (different colors). Only the r1-r2* relaxivity is correlated with the transferrin/iron ratio. **(c)** Fully- constrained model predicts the fractions of iron-binding proteins in the *in vivo* human brain. The *in vivo* r1-r2* relaxivity measured in each brain area was modeled as a weighted sum of the r1-r2* relaxivities of transferrin and ferritin (Eq. 10). Rearranging the model allows for the MRI prediction of the transferrin fraction (y-axis) for younger and older subjects (different symbols) in 10 brain regions (different colors). There are no free parameters in the model. The x-axis shows the transferrin fraction measured postmortem[5,7,9]. MAE=mean absolute error. *WM=white-matter, CTX=cortex.*

parameters, that allows predicting the transferrin-ferritin fraction without any fitting process (Eq. 8 in Methods, for a more detailed discussion on possible biophysical models for the r1-r2* relaxivity *in vitro* and *in vivo*, and assessment of the myelin contribution to these models, see **Sup. Section 4.4**). Remarkably, the *in vivo* predictions of this fully-constrained model for the transferrin-ferritin fraction corresponded to the histological measurements across brain regions and age groups (**Figure 4c**; F-test, $p<0.005$, mean absolute error (MAE)=3.8%; the pallidum was excluded, see **Sup. section 5**). This finding was replicated on an independent dataset scanned with a different scanner (**Sup. Figure 39**). We corroborated these findings with numerical simulations of the r1-r2* relaxivity of brain tissue. In these simulations we further demonstrated that the measured changes in the r1-r2* relaxivity across the brain can be induced by changes in the transferrin-ferritin fraction (**Sup. Section 4.3**). Moreover, we find that the effect of the transferrin-ferritin fraction on the r1-r2* relaxivity is not confounded by the myelin concentration and is well above the detection limit of this MRI measurement (**Sup. Figure 9**). Therefore, the *in vivo* r1-r2* relaxivity reveals important characteristics of the iron environment previously inaccessible with MRI.

## Discussion

We present a new relaxivity approach for increasing the sensitivity of MRI to different molecular compounds of iron. First, we confirm *in vitro* that different iron compounds induce different relaxivities, which can be estimated with MRI using the r1-r2* relaxivity. When examining R1 and R2* independently, we find the molecular state of iron is confounded by the strong effects of iron and myelin concentrations. However, we show that the r1-r2* relaxivity resolves this ambiguity and reveals the intrinsic paramagnetic properties of different iron compounds. In the human brain, we show that the r1-r2* relaxivity provides a new MRI contrast. This contrast is useful for enhancing the distinction between tumor tissue and non-pathological tissue. We further demonstrate that this new contrast allows for the detection of biological properties previously inaccessible to conventional MRI approaches. We confirm this finding by associating *in vivo* MRI measurements with RNA sequencing and protein expression levels in tumor tissues. This unique *in vivo* to *ex vivo* strategy, along with group-level analysis on healthy subjects, are used to establish the sensitivity of r1-r2* relaxivity to molecular iron compounds in the brain.

The r1-r2* relaxivity predicts the inhomogeneous distribution of iron compounds due to aging and across the brain, and reveals the state of iron homeostasis in tumors.

Relaxivity commonly is employed to characterize MR contrast agents[63]. While most contrast agents induce relaxation based on their paramagnetic or superparamagnetic properties, some agents elevate the R1 relaxation rate more efficiently while others elevate R2*. R1 relaxation mechanisms are affected by local molecular interactions, while R2* is sensitive to more global effects of extended paramagnetic interactions at the mesoscopic scale[36]. In this work, we show that by contrasting these two different mechanisms, we obtain a rich description of the endogenous iron environment without the injection of an external contrast agent.

The concept of iron relaxivity, and its ability to distinguish between molecular environments of iron, was previously suggested by several postmortem and *in vitro* studies[31–34]. We reproduce these results in our *in vitro* experiments and further demonstrate that different iron compounds have different iron relaxivity. Moreover, Ogg et al.[31] calculated the iron relaxivity by comparing postmortem measurements of iron concentration for different age groups to the typical R1 values in those age groups. They found that this approximation of iron relaxivity was higher in the gray matter and white matter than in sub-cortical structures. Remarkably, we replicate this result in living subjects, based on our novel approach for estimating the iron relaxivity *in vivo*. The theoretical derivation we propose for the r1-r2* relaxivity shows that it represents the ratio of the iron relaxivities of R1 and R2*. This theory was supported by our *in vitro* experiments. Therefore, the *in vivo* iron relaxivity approach for measuring iron compounds is based on substantial theoretical grounds[31–34]. We exploit the different relaxation rates for a biophysical model of their linear interdependency, thus allowing for the estimation of iron relaxivity in the living brain for the first time.

In this work, we focus on the contributions of ferritin and transferrin to the iron relaxivity contrast. These two iron-binding proteins are the most common iron compounds in the brain, with extensive implications for iron homeostasis[3,5–7]. Since transferrin binds three orders of magnitude less iron than does ferritin[3], transferrin's levels in the brain previously were assumed to be insufficient to affect the MRI signal[3,4]. *In vitro*, we find that the R2* values of transferrin

samples are much lower than the R2* values of ferritin. On the other hand, we find that the R1 values of transferrin and ferritin are on the same order of magnitude. We show that transferrin and ferritin induce different relaxivities, even when accounting for the discrepancies in iron-binding. This implies that, similarly to different contrast agents, the physical mechanisms by which these two iron compounds interact with the surrounding water environment are inherently different. To further confirm that the strong transferrin effect on R1 is related to its paramagnetic properties and not the presence of the protein itself, we tested MRI measurements of apo-transferrin (transferrin unbound to iron). In this case, the R1 effect of transferrin vanished. Therefore, iron bound to transferrin induces strong R1 relaxivity, which can be detected by the r1-r2* relaxivity to allow differentiation between iron compounds. Moreover, evaluating ferritin-transferrin mixtures we find that both iron compounds affect the r1-r2* relaxivity measurements. The transferrin concentrations in our *in vitro* experiments were relatively high, in order to achieve physiological iron concentrations[3,4]. While in the human brain transferrin concentrations are lower[3,4], we show that the effect of the transferrin-ferritin fraction on the r1-r2* relaxivity is measurable *in vivo*. First, we claim that the r1-r2* relaxivity is sensitive to the homeostasis between iron compounds, and not to their absolute concentrations. Indeed, the r1-r2* relaxivity is not correlated with the absolute ferritin, transferrin or iron concentrations, but it allows to predict the transferrin-ferritin fraction across brain regions and age groups, as well as in meningioma tumors. To further validate that the r1-r2* relaxivity is sensitive to the transferrin-ferritin fraction, even when accounting for the low prevalence of transferrin in the brain, we generated a simulation of a brain-like environment which contains multiple tissue components (Sup. Section 4.2). Assuming physiological ferritin and transferrin concentrations, we found that changes in the ferritin-transferrin fraction led to considerable changes in the r1-r2* relaxivity. This effect could not be attributed to the absolute concentrations of ferritin and transferrin, only to the ratio between them. Moreover, we found that the changes in the r1-r2* relaxivity produced by different physiological transferrin-ferritin ratios are well above the detection limit of this MRI measurement. Therefore, we show *in vitro*, *in vivo*, *ex vivo* and in numerical simulations, that the r1-r2* relaxivity measurement allows to detect changes in the interplay between ferritin and transferrin under physiological conditions.

Our results indicate that ferritin and transferrin govern the r1-r2* relaxivity contrast in the brain. Using a model of their separate contributions to the observed r1-r2* relaxivity *in vivo*, we predicted the transferrin-ferritin fractions across brain regions and age groups. Moreover, we found that the r1-r2* relaxivity is higher for tumors with a higher transferrin-ferritin ratio. Nevertheless, our approach might be generalizable to other iron compounds. We show that liposomes with ferrous ions have distinct iron relaxivities compared to liposomes with transferrin. Other iron compounds that exist in the brain, such as hemoglobin, hemosiderin, neuromelanin, magnetite, ferric ion, lactoferrin and melanotransferrin [4], might have distinct iron relaxivities as well. Moreover, other characteristics of the iron environment such as iron compounds' cluster sizes, spatial distributions and iron loadings, could all have an additional effect on the iron relaxivity. While we used transferrin and ferritin to explain a considerable amount of the variability in the r1-r2* relaxivity in the brain, other iron compounds could affect this measurement. For example, catecholamine neurons of the substantia nigra and locus coeruleus are rich in neuromelanin-iron complexes[4,64] which could contribute to the r1-r2* relaxivity measurement in these regions (see also **Sup. section 5** regarding the pallidum). In order to model the separate contributions to the MRI signal of additional iron compounds, it would be necessary to increase the dimensionality of the *in vivo* iron relaxivity measurement. In addition to R1 and R2*, other qMRI parameters known to be sensitive to iron include quantitative susceptibility mapping (QSM) and R2[3,4]. In addition, it was suggested that magnetization transfer (MT) measurements are affected by neuromelanin-iron complexes[12,65]. The linear interdependencies of these other iron-related MRI measurements may uncover additional features of the iron environment[66]. Therefore, we speculate that the concept we introduce here, of exposing the iron relaxivities *in vivo* based on the linear dependency of R1 on R2* (the r1-r2* relaxivity), can be generalized to further increase MRI's specificity for iron using additional complementary measurements. For example, in a previous work we implemented a different aspect of relaxivity for the detection of lipid composition, based on the linear dependency of qMRI parameters on the macromolecular tissue volume (MTV)[45]. Here, we demonstrate that the r1-r2* relaxivity and the dependency of R1 on MTV provide two orthogonal microstructural axes (**Sup. section 2**). The dependency of R1 on MTV changes according to the lipid types, even in the

presence of iron, while the r1-r2* relaxivity is insensitive to the lipid types and provides better distinctions between iron compounds.

The strength of our relaxivity approach is demonstrated by comparing the r1-r2* relaxivity to the individual R1 and R2* measurements. R1 and R2*, along with most qMRI parameters, are known to suffer from low biological specificity[4,19,25,29,39–41]. The common MRI contrast between gray matter and white matter usually is associated with myelin, while an additional and often correlated effect is attributed to the iron concentration[4]. We demonstrate, *in vitro* and *in vivo* and in numerical simulations, that the r1-r2* relaxivity reduces this ambiguity and reveals the sensitivity of MRI to properties of the molecular iron environment, otherwise confounded by myelin and iron concentrations. *In vitro*, we show that the r1-r2* relaxivity is stable across iron and liposomal concentrations. *In vivo*, we show that the great contrast between white matter and gray matter usually observed in R1 and R2* is no longer as substantial in the r1-r2* relaxivity. In return, this measurement does enhance the contrast between pathological tissue and normal tissue and is associated with distinct gene expression pathways. Furthermore, the meningioma tumor environment is not myelinated, and still we find variability in the r1-r2* relaxivity between tumors, which is explained by their different transferrin-ferritin ratios. Another evidence for the minimal effect of myelin on the r1-r2* relaxivity is that the qMRI measurements of MTV[45], which was shown to approximate the myelin content [46–50], and mean diffusivity (MD), which is sensitive to myelin characteristics[51], are both highly correlated with R1 and R2* but not with the r1-r2* relaxivity. In brain tissue numerical simulations, we show that the myelin content substantially affects the measurements of R1 and R2*, but it is not the main component governing the measurement of the r1-r2* relaxivity, and in simulations of physiological conditions it cannot by itself explain the measured variability in the r1-r2* relaxivity across the brain (**Sup. section 4.3**). Finally, evaluating different biophysical models for the r1-r2* relaxivity, we found that adding the myelin contribution to the model is not necessary in order to explain the r1-r2* relaxivity measured across the brain (**Sup. section 4.4**). Nonetheless, the iron and myelin contents of brain tissue are tightly related, as iron is required for the formation of myelin[4], and thus it could be that the r1-r2* relaxivity contains some residual contribution of the myelin content. Simulating an extreme case in which iron and myelin are completely correlated,

we still find that the r1-r2* relaxivity changes with the transferrin-ferritin fraction. Taken together, our results indicate that the correlations between MRI and various iron-related histological measurements are specific for the r1-r2* relaxivity and are undetectable by R1 and R2* alone. Hence, the relaxivity framework reveals distinct biological features otherwise undetectable in standard qMRI measurements. Its implications can be generalized further to boost MRI's specificity and support a more comprehensive *in vivo* histology with qMRI.

While the field of *in vivo* histology with MRI is rapidly growing, ground-truth validation remains a great challenge. Here we propose a cutting-edge validation strategy combining both bottom-up and top-down approaches in which we incorporate *in vitro*, *in vivo* and *ex vivo* analyses. For the bottom-up analysis, we developed a unique, synthetic biological system that allows us to examine the biophysical interpretation of the r1-r2* relaxivity in highly controlled *in vitro* settings. For the top-down analysis, we tested whether our interpretation remains valid in the context of the extremely complex biological tissue. We compared the r1-r2* relaxivity measured *in vivo* to histological measurements of iron compounds and gene expression. This comparison was done both at the group level, based on previously reported findings, and at the single-subject level, by analyzing resected tumor tissues. To our knowledge, this is the first time that qMRI parameters measured *in vivo* have been compared to *ex vivo* iron histology and gene expression of the same human tissue. Moreover, our bottom-up and top-down approaches converged onto the proposed biophysical model, which combined *in vitro* and *in vivo* measurements of the r1-r2* relaxivity, to successfully predict the transferrin-ferritin fraction in the brain. This result was replicated on an independent dataset. Taken together, the different validation strategies all indicate that the r1-r2* relaxivity increases the specificity of MRI to different molecular compounds of iron, highlighting the robustness of our findings.

Our proposed approach for measuring iron compounds *in vivo* using the r1-r2* relaxivity may have wide clinical and scientific implications. First, the r1-r2* relaxivity provides a new contrast for imaging the brain, which is associated with 45 distinct gene sets, not associated with R1 or R2* by themselves. Moreover, we show that the r1-r2* relaxivity, which captures paramagnetic properties, enhances the contrast between tumor tissue and normal-appearing white-matter and gray-matter tissues. In agreement with these findings, meningioma tumors have been

shown to contain a higher concentration of ferrimagnetic particles and an abnormal expression of iron-related genes compared to non-pathological brain tissue[17,18]. Indeed, the contrast enhancement we saw with the r1-r2* relaxivity is similar to the one observed for Gd-enhanced imaging, which is based on the altered relaxivity in the presence of paramagnetic agents[67]. Concerns regarding the safety of Gd-based contrast agents raise the need for Gd-free diagnosis of brain tumors[53,54]. Adjusting our approach for clinical imaging might offer safer alternatives for brain tumor diagnosis.

Finally, the sensitivity of the r1-r2* relaxivity to different molecular compounds of iron in the brain may have clinical implications for neurodegenerative diseases. Alterations in the distribution of molecular iron compounds can lead to cellular damage which is disease-specific[10]. In particular, the ratio of transferrin to iron was shown to differ between elderly controls and patients diagnosed with either Parkinson's disease (PD) or Alzheimer's disease (AD)[7]. We found that the transferrin-iron ratio is correlated with the r1-r2* relaxivity across brain regions and age groups. This result, in addition to our other validation strategies, demonstrate the sensitivity of the r1-r2* relaxivity to the iron homeostasis in the brain and in the aging process. Therefore, our approach can add a new important layer of information to existing *in vivo* PD and AD biomarkers such as neuromelanin MRI[12] and may further advance the research, diagnosis and treatment of neurodegenerative diseases[1,2,5–9].

## Conclusion:

We present a novel MRI contrast, based on the r1-r2* relaxivity, for the non-invasive mapping of different iron compounds in the human brain. This new technology can differentiate between tumor tissue and non-pathological tissue without injecting contrast agents, and can detect biological properties inaccessible to conventional MRI approaches. We validated the sensitivity of the r1-r2* relaxivity to the molecular state of iron using both bottom-up and top-down approaches while integrating *in vitro*, *in vivo* and *ex vivo* analyses. We show that our MRI technology reveals the intrinsic paramagnetic properties of different iron compounds. Furthermore, our approach can be used to predict the distribution of iron compounds across brain regions and age groups, and to reveal differences in iron homeostasis in pathological

476 tissues. Therefore, this approach may further advance our understanding of the impaired iron
477 homeostasis in cancer, normal aging and neurodegenerative diseases, and may open new
478 avenues for the non-invasive research and diagnosis of the living human brain.

479

480

481 ## Methods:

482 ***In vivo iron relaxivity model***:
483 The iron relaxivity model assumes a linear relationship between relaxation rates and iron
484 concentration[31–34].
485 This linear relationship for two different iron compounds *a* and *b* in concentrations [a] and [b]
486 can be expressed using the following equations:

487 $$(1)\ R_1 = r_{(1,a)}[a] + c_{(1,a)} \qquad R_1 = r_{(1,b)}[b] + c_{(1,b)}$$
488 $$(2)\ R_2^* = r_{(2,a)}[a] + c_{(2,a)} \qquad R_2^* = r_{(2,b)}[b] + c_{(2,b)}$$

489 where $r_{(1/2,a/b)}$ represents the R1-iron relaxivity or the R2*-iron relaxivity of the a or b iron
490 compound, and $c$ is the corresponding constant.
491 The two iron compounds are distinguished by their iron relaxivities under the assumption:

492 $$(3)\ r_{(1,a)} \neq r_{(1,b)} \qquad and/or \qquad r_{(2,a)} \neq r_{(2,b)}$$

493 Rearranging Eq. 2:

494 $$(4)\ [a] = \frac{R_2^* - c_{(2,a)}}{r_{(2,a)}} \qquad [b] = \frac{R_2^* - c_{(2,b)}}{r_{(2,b)}}$$

495 Substituting Eq. 4 in Eq. 1:

496 $$(5)\ R_1 = \frac{r_{(1,a)}}{r_{(2,a)}} R_2^* + const \qquad R_1 = \frac{r_{(1,b)}}{r_{(2,b)}} R_2^* + const$$

497 where $\frac{r_{(1,a)}}{r_{(2,a)}}$ and $\frac{r_{(1,b)}}{r_{(2,b)}}$ represent the linear dependencies of R1 on R2* (r1-r2* relaxivities) of the
498 two iron compounds *a* and *b*. Importantly, the MRI-measured r1-r2* relaxivity serves as an *in*
499 *vivo* estimator of iron relaxivity and reveals intrinsic properties of the iron compounds.

500 Assuming that the iron relaxivity of R1 provides a different separation between the two iron
501 compounds *a* and *b* compared to the iron relaxivity of R2*:

$$\frac{r_{(1,a)}}{r_{(2,a)}} \neq \frac{r_{(1,b)}}{r_{(2,b)}}$$

These two iron compounds *a* and *b* then can be distinguished by their r1-r2* relaxivities (i.e., the *in vivo* iron relaxivity).

## Fully constrained model for the contribution of transferrin and ferritin to the *in vivo* iron relaxivities:

The r1-r2* relaxivity measurement is defined as the linear dependency of R1 on R2* within an ROI in the brain. This is equivalent to the total change in R1 relative to the total change in R2* ($\frac{\Delta R_1}{\Delta R_2^*}$). Assuming the r1-r2* relaxivity measured in a specific region of interest (ROI) in the brain, $(\frac{\Delta R_1}{\Delta R_2^*})_{ROI}$, represents a weighted sum of the r1-r2* relaxivities of *N* different iron compounds:

$$(6)\quad (\frac{\Delta R_1}{\Delta R_2^*})_{ROI} = \sum_{i=1}^{N} f_i * \frac{r_{(1,i)}}{r_{(2,i)}}$$

such that $f_i$ represents the relative fraction of the i'th iron compound in the given ROI ($\sum_{i=1}^{N} f_i = 1$), and $\frac{r_{(1,i)}}{r_{(2,i)}}$ is the r1-r2* relaxivity of the i'th iron compound (Eq. 5).

As ferritin (Ft) and transferrin (Tf) are the most abundant iron compounds in the brain, we can approximate Eq. 6 with their r1-r2* relaxivity:

$$(7)\quad (\frac{\Delta R_1}{\Delta R_2^*})_{ROI} \approx (1-f) * \frac{r_{(1,Ft)}}{r_{(2,Ft)}} + f * \frac{r_{(1,Tf)}}{r_{(2,Tf)}}$$

Where $f$ is the transferrin fraction ($f = \frac{[Tf]}{[Tf]+[Ft]}$ and $(1-f) = \frac{[Ft]}{[Tf]+[Ft]}$, $[Tf]$ and $[Ft]$ are the transferrin and ferritin concentrations). $\frac{r_{(1,Tf)}}{r_{(2,Tf)}}$ and $\frac{r_{(1,Ft)}}{r_{(2,Ft)}}$ are the r1-r2* relaxivities of transferrin and ferritin correspondingly (Eq. 5).

Rearranging the equations allows us to predict the transferrin-ferritin fraction ($f$) in a given ROI in the brain from the r1-r2* relaxivities:

$$(8)\quad f = \frac{[Tf]}{[Tf]+[Ft]} \approx \frac{(\frac{\Delta R_1}{\Delta R_2^*})_{ROI} - \frac{r_{(1,Ft)}}{r_{(2,Ft)}}}{\frac{r_{(1,Tf)}}{r_{(2,Tf)}} - \frac{r_{(1,Ft)}}{r_{(2,Ft)}}}$$

The r1-r2* relaxivities of ferritin and transferrin can be estimated from our *in vitro* experiments with liposomal ferritin and liposomal transferrin (**Figure 1**):

$$(9)\quad \frac{r_{(1,Ft)}}{r_{(2,Ft)}} = 0.006$$

$$(10)\quad \frac{r_{(1,Tf)}}{r_{(2,Tf)}} = 0.147$$

The r1-r2* relaxivity measured in a specific ROI in the brain ($(\frac{\Delta R_1}{\Delta R_2^*})_{ROI}$) can be estimated from *in vivo* MRI scans.

After fixing the model's coefficients in Eq. 8 to the ones estimated for iron compounds in liposomal phantoms in-vitro and for brain ROIs *in vivo*, there are no free parameters. Therefore, Eq. 8 represents a fully constrained model that allows for the estimation of the transferrin fraction in different brain regions without requiring any fitting.

A more detailed derivation of this model and its biophysical implications, a discussion on other possible biophysical models for the r1-r2* relaxivity *in vitro* and *in vivo*, and assessment of the myelin contribution to these models, can be found in Sup. Section 4.

## Phantom samples experiments:

### Phantom system:

We prepared samples of four different iron compounds: transferrin (holo-transferrin human, Sigma), apo-transferrin (apo-transferrin human, Sigma), ferritin (equine spleen, Sigma), and ferrous (iron (II) sulfate heptahydrate, Sigma). These samples were prepared in three different molecular environments: liposomes, 18.2 MΩ-cm water, and bovine serum albumin (BSA, Sigma)[68,69]. For each combination of iron compound and molecular environment, we made different samples by varying both the iron compound concentration and the lipid/BSA-water fractions. For liposomal/BSA environments, the iron compounds concentrations were divided by the water-lipid or water-BSA fractions to get units of [mg/wet ml]. The liposomes were made from a mixture of soy phosphatidylcholine (PC) and egg sphingomyelin (SM) purchased from Lipoid and used without further purification. Additional results with PC and PC-cholesterol (Sigma) liposomes are presented in Sup. Section 2. The lipid samples were mixed in chloroform at desired mole ratios and evaporated under reduced pressure (8 mbar) in a Buchi rotary evaporator vacuum system (Flawil, Switzerland). The resulting lipid film was resuspended in a 10 mM ammonium bicarbonate solution, lyophilized, and subsequently hydrated in the reassembly buffer. To achieve the desired lipid-protein concentration, the protein solution (~50 mg/ml in water) was diluted to the right concentration and subsequently was added to the lyophilized lipid powder. For the BSA phantoms, samples were prepared by dissolving lyophilized BSA in 18.2 MΩ-cm water at the desired concentrations.

Samples were placed in a 2-ml glass vials glued to a glass box, which was then filled with ~1% SeaKem® LE Agarose (Ornat) and 0.1% gadolinium (Gadoteric acid (Dotarem, Guerbet)) dissolved in distilled water (DW). The purpose of the agarose with gadolinium (Agar-Gd) was to stabilize the vials and to create a smooth area in the space surrounding the samples that minimalized air-sample interfaces.

## MRI acquisition for phantoms:

Data were collected on a 3T Siemens MAGNETOM Skyra scanner equipped with a 32-channel head receive-only coil at the ELSC Neuroimaging Unit at the Hebrew University.

*Quantitative R1 & MTV:* 3D Spoiled gradient echo (SPGR) images were acquired with different flip angles (FA = 4°, 8°, 16°, and 30°). The TE/TR were 4.45/18 ms. The scan resolution was 0.5 mm x 0.5 mm x 0.6 mm. For calibration, we acquired an additional spin-echo inversion recovery (SEIR) scan. This scan was done on a single slice, with an adiabatic inversion pulse and inversion times of TI = 2,000, 1,200, 800, 400, and 50 ms. The TE/TR were 73/2,540 ms. The scan resolution was 1.2 mm x 1.2 mm x 2.0 mm.

*Quantitative R2*:* SPGR images were acquired with different flip angles (α = 4°, 8°, 16°, and 30°). The TR was 27 ms and 5 echoes were equally spaced between 4.45 and 20.85 ms. The scan resolution was 0.5 mm x 0.5 mm x 0.6 mm.

## Estimation of qMRI parameters for phantoms:

*Quantitative R1 & MTV mapping:* R1 and MTV estimations for the lipid samples were computed with the mrQ [45] (https://github.com/mezera/mrQ) and Vista Lab (https://github.com/vistalab/vistasoft/wiki) software packages. The mrQ software was modified to suit the phantom system[69]. The modification utilizes the fact that the Agar-Gd mixture which fills the box around the vials is homogeneous, and therefore can be assumed to have a constant R1 value. We used this gold-standard R1 value generated from the SEIR scan to correct for the excite bias in the SPGR scans.

A mask labeling the different phantom samples was generated based on MATLAB's "imfindcircles" function, and was filtered to remove voxels with extremely high and low signals. Voxels were filtered based on a fixed threshold on the SPGR signal at FA=16. In addition, we also filtered out those voxels in which the SPGR signal at FA=16 was two median absolute deviations away from the median value. We further edited this mask manually, removing voxels with susceptibility artifacts resulting from the vials and air pockets. To fit the R1 and proton density of each phantom sample, we calculated the median values of the SPGR signal as well as the excite and receive biases across all the voxels of each sample. These median values were used in the Vista Lab function "relaxFitT1" to find the median R1 and proton density of each sample. proton density values then were calibrated using the proton density of a water-filled vial in order to calculate the MTV values.

*Quantitative R2* mapping:* We used the SPGR scans with multiple echoes to estimate R2*. Fitting was done by taking the median values of the SPGR signal across all the voxels of the phantom sample for each TE. To label the different samples, we used the same mask that was used to calculate R1 and MTV. We then used an exponential fitting process to find R2*. As we

had four SPGR scans with variable flip angles, we averaged the R2* values acquired from each of these scans for increased signal to noise ratio.

### r1-r2* relaxivity computation for phantoms:

For each iron compound in each molecular environment, we computed the linear dependency of R1 on R2* across samples with varying iron-binding proteins concentrations relative to the water fractions. We fitted the following linear model across samples:

$$R1 = a * R2^* + b$$

The slope of this linear model ($a$) represents the r1-r2* relaxivity. $b$ is constant. This process was implemented in MATLAB.

### Estimation of total iron content in phantoms:

We estimated the iron content of our transferrin and ferritin samples using the following equation:

$$iron\ \left(\frac{mg}{ml}\right) = \frac{iron\ binding\ protein\ \left(\frac{mg}{ml}\right)}{protein\ molecular\ weight\ \left(\frac{mg}{mol}\right)} * \frac{iron\ ions}{protein} * iron\ molecular\ weight\ \left(\frac{mg}{mol}\right)$$

Transferrin contains 2 iron ions per protein molecule[3], and its molecular weight was estimated as $76*10^6$ mg/mol (based on manufacturer information). The iron loading of ferritin was estimated as 2,250 iron ions per protein molecule (based on manufacturer information) and its molecular weight was estimated as $440*10^6$ mg/mol[3]. The molecular weight of iron was set to $55.847*10^3$ mg/mol.

This resulted in the following equation for converting iron-binding protein concentrations into iron concentrations:

1 mg/ml transferrin = 1.4 µg/ml iron

1 mg/ml ferritin = 0.29 mg/ml iron

### MRI human dataset:

### Healthy Human subjects:

We scanned 26 young adults (aged 27 ± 10 years, 10 females), and 13 older adults (aged 70 ± 3 years, 4 females). Healthy volunteers were recruited from the community surrounding the Hebrew University of Jerusalem. The experimental procedure was approved by the Helsinki Ethics Committee of Hadassah Hospital, Jerusalem, Israel. Written informed consent was obtained from each participant prior to the procedure. This data was first used in our previous work[68].

### Meningioma patients:

630 During the study period May 2019 to August 2020, we recruited 19 patients who had undergone
631 surgery for the resection of brain meningiomas. All patients had preoperative qMRI scans in
632 addition to their clinical brain MRI assessment. One subject, with a titanium cranial fixation plate
633 adjacent to the tumor, was excluded from the study due to local disruption of the magnetic field.
634 The final cohort included 18 patients (11 females). Imaging studies were anonymized before they
635 were transferred for further analysis. Brain meningioma surgical specimens, available for 16
636 patients, were obtained from the fresh frozen tissue biobank of the Department of
637 Neurosurgery, Shaare Zedek Medical Center, Jerusalem, Israel, and were transferred on dry ice
638 for western-blot and gene expression analyses. Study participants provided informed consent
639 according to an institutional review board.

640 MRI acquisition for healthy human subjects:

641 Data were collected on a 3T Siemens MAGNETOM Skyra scanner equipped with a 32-channel
642 head receive-only coil at the ELSC Neuroimaging Unit at the Hebrew University.

643 *Quantitative R1, R2* & MTV mapping:* SPGR echo images were acquired with different flip angles
644 ($\alpha$ = 4°, 10°, 20° and 30°). Each image included 5 equally spaced echoes (TE=3.34-14.02 ms) and
645 the TR was 19 ms. The scan resolution was 1 mm isotropic. For calibration, we acquired an
646 additional spin-echo inversion recovery scan with an echo-planar imaging read-out (SEIR-epi).
647 This scan was done with a slab-inversion pulse and spatial-spectral fat suppression. For SEIR-epi,
648 the TE/TR were 49/2,920 ms. The TIs were 200, 400, 1,200, and 2,400 ms. We used 2-mm in-
649 plane resolution with a slice thickness of 3 mm. The EPI readout was performed using 2×
650 acceleration.

651 *Anatomical images:* 3D magnetization-prepared rapid gradient echo (MP-RAGE) scans were
652 acquired for 30 of the 39 healthy subjects. The scan resolution was 1 mm isotropic, the TE/TR
653 were 2.98/2,300 ms. Magnetization-prepared 2 rapid acquisition gradient echo (MP2RAGE)
654 scans were acquired for the remaining 9 subjects. The scan resolution was 1 mm isotropic, the
655 TE/TR were 2.98/5,000 ms.

656 *Whole-brain DTI measurements:* performed using a diffusion-weighted spin-echo EPI sequence
657 with isotropic 1.5-mm resolution. Diffusion weighting gradients were applied at 64 directions
658 and the strength of the diffusion weighting was set to b = 2000 s/mm2 (TE/TR=95.80/6,000 ms,
659 G=45 mT/m, $\delta$=32.25 ms, $\Delta$=52.02 ms). The data includes eight non-diffusion-weighted images
660 ($b$ = 0). In addition, we collected non-diffusion-weighted images with reversed phase-encode
661 blips. For two subjects (1 young, 1 old) we failed to acquire this correction data and they were
662 excluded from the diffusion analysis.

663 MRI acquisition for meningioma patients:

Data were collected on a 3T Siemens MAGNETOM Skyra scanner equipped with a 32-channel head receive-only coil at the Shaare Zedek Medical Center.

*Quantitative R1, R2* & MTV mapping:* SPGR echo images were acquired with different flip angles ($\alpha$ = 4°, 10°, 20° and 30°). Each image included 5 equally spaced echoes (TE=2.85-14.02 ms) and the TR was 18 ms. The scan resolution was 1.5 mm isotropic. For calibration, we acquired an additional SEIR-epi scan. This scan was done with a slab-inversion pulse and spatial-spectral fat suppression. For SEIR-epi, the TE/TR were 49/2,920 ms. The TIs were 200, 400, 1,200, and 2,400 ms. We used 2-mm in-plane resolution with a slice thickness of 3 mm. The EPI readout was performed using 2× acceleration.

*Gd-enhanced anatomical images:* Gd-enhanced MPRAGE scans were acquired. The scan resolution was 1 mm isotropic, the TE/TR were 2.4/1,800 ms. The contrast agent was either Multihance or Dotarem at a dose of 0.1 mmol/kg. Contrast agent injection and MPRAGE acquisition were done after the acquisition of the quantitative MRI protocol, or on a different day.

## Estimation of qMRI parameters for human subjects:

*Quantitative R1 & MTV mapping:* Whole-brain MTV and R1 maps, together with bias correction maps of B1+ and B1-, were computed using the mrQ software[45,70].

*Quantitative R2* mapping:* We used the SPGR scans with multiple echoes to estimate R2*. Fitting was performed with the MPM toolbox[71]. As we had four SPGR scans with variable flip angles, we averaged the R2* maps acquired from each of these scans for increased SNR.

*Quantitative MD mapping:* Diffusion analysis was done using the FDT toolbox in FSL [72,73]. Susceptibility and eddy current induced distortions were corrected using the reverse phase-encode data, with the eddy and topup commands[74,75]. MD maps were calculated using vistasoft (https://github.com/vistalab/vistasoft/wiki).

## Brain segmentation in healthy subjects:

Whole-brain segmentation was computed automatically using the FreeSurfer segmentation algorithm[76]. For subjects with MPRAGE scan, we used that as a reference; for the other subjects the MP2RAGE scan was used. These anatomical images were registered to the R1 space prior to the segmentation process, using a rigid-body alignment. FreeSurfer's estimates of subcortical gray-matter structures were replaced with estimates from FSL's FIRST tool[77].

## Brain segmentation in meningioma patients:

Tumor contouring was performed by the neurosurgeon (T.S.) using BrainLab's Elements software (BrainLab AG, Munich, Germany) over the Gd-enhanced MPRAGE images, and exported as a

DICOM file for further analysis. The contours of the tumors were registered to the R1 space using rigid-body segmentation. Cases that required manual adjustment were examined and approved for accuracy by the neurosurgeon (T.S.).

Whole-brain segmentation was computed automatically using the FreeSurfer segmentation algorithm[76]. We used the synthetic T1w image generated with mrQ as the reference image, from which we removed the skull and the tumor. We then ran FreeSurfer with the "-noskullstrip" flag. For each patient, we used FreeSurfer's segmentation in the tumor-free hemisphere. Estimates for the entire white matter and gray matter tissues were averaged across the different FreeSurfer parcellations in these regions.

### r1-r2* relaxivity computation for ROIs in the human brain:

We used MATLAB to compute the r1-r2* relaxivity in different brain areas. For each ROI, we extracted the R2* and R1 values from all voxels. R2* values were pooled into 36 bins spaced equally between 0 and 50 $s^{-1}$. This was done so that the linear fit would not be heavily affected by the density of the voxels in different R2* regimes. We removed any bins in which the number of voxels was smaller than 4% of the total voxel count in the ROI. The median R2* of each bin was computed, along with the R1 median. We used these data points to fit the following linear model across bins:

$$R1 = aR_2^* + b$$

The slope of this linear model ($a$) represents the r1-r2* relaxivity. $b$ is constant.

### Generating voxel-wise r1-r2* relaxivity maps:

In order to generate a voxel-wise map of the r1-r2* relaxivity in the brain, we calculated the local linear dependency of R1 on R2* using a moving-window approach. For each voxel within the brain mask, we extracted R1 and R2* values of that voxel and all its neighboring voxels (a box of 125 voxels total). If at least 10 of these voxels were inside the brain mask, we fit the following linear model across these voxels:

$$R1 = aR_2^* + b$$

The slope of this linear model ($a$) represents the local r1-r2* relaxivity of the voxel. $b$ is constant.

### Group-level comparison of qMRI parameters and histological measurements:

We aggregated data published in different papers[5,7,9] that describe ferritin, transferrin and iron concentrations in 11 brain regions. One of the papers[9] described the concentration of L-rich ferritin and H-rich ferritin independently and we combined these estimates for each ROI to get the total ferritin concentration. One of the papers[5] reported the iron level in units of [µmol Fe/ g protein] and we converted these measurements to units of [µg Fe/ g protein]. In order to use

this data for our analysis with we matched the brain regions reported in the literature with their corresponding FreeSurfer labels. We tested the correlations of the three qMRI parameters (R1, R2*, and the r1-r2* relaxivity) with six different histological features (transferrin, ferritin and iron concentrations, and the transferrin/iron, ferritin/iron and transferrin/(transferrin + ferritin) ratios) and with MTV. We then applied FDR correction for multiple (3×7=21) comparisons. The following table summarizes the data taken from the literature (reference for each measurement is shown) and the matching FreeSurfer labels:

| Brain Region | FreeSurfer labels[(f)] | Age group | Transferrin [ng/µg protein][(a)] | Ferritin [ng/µg protein] [(b)] | Iron [mg/g protein] [(c)] |
|---|---|---|---|---|---|
| Frontal CTX | 1003,1012,1014,1019 ,1020,1027,1028,1032 | younger | 3.88[7] | 45.34[9] | 1.21[7] |
| | | older | 4.09[7] | 89.77[9] | 1.59[7] |
| Caudate | 11 | younger | 3.21[7] | 60.92[9] | 1.79[7] |
| | | older | 4.44[7] | 135.12[9] | 3.34[7] |
| Putamen | 12 | younger | 3.49[7] | 58.63[9] | 2.59[7] |
| | | older | 4.47[7] | 124.12[9] | 4.62[7] |
| Substantia nigra (midbrain)[(d)] | 173 | younger | 2.45[7] | 54.96[9] | 2.92[7] |
| | | older | 3.42[7] | 135.12[9] | 5.70[7] |
| Globus pallidus[(e)] | 13 | younger | 4.82[7] | 28.40[9] | 7.39[7] |
| | | older | 5.10[7] | 215.27[9] | 4.07[7] |
| Gray superior temporal gyrus (Temporal CTX)[(d)] | 1001,1006,1007,1009, 1015,1016,1030,1033,1034 | younger | 1.84[5] | 25.65[5] | 0.45[5] |
| | | older | 1.08[5] | 24.20[5] | 0.69[5] |
| White superior temporal gyrus (Temporal WM)[(d)] | 3001,3006,3007,3009, 3015,3016,3034,3030,3033 | younger | 3.82[5] | 44.87[5] | 0.72[5] |
| | | older | 2.52[5] | 33.50[5] | 0.74[5] |
| Motor CTX | 1017,1022,1024,1031 | younger | 2.91[5] | 40.20[5] | 1.16[5] |
| | | older | 2.93[5] | 22.13[5] | 0.89[5] |
| Motor WM | 3024,3017,3022,3031 | younger | 5.75[5] | 30.38[5] | 1.39[5] |
| | | older | 7.34[5] | 21.51[5] | 1.25[5] |
| Occipital CTX | 1011,1013,1005,1021 | younger | 1.75[5] | 9.34[5] | 0.50[5] |
| | | older | 1.67[5] | 34.27[5] | 1.16[5] |
| Occipital WM | 3011,3013,3005,3021 | younger | 3.53[5] | 13.81[5] | 0.80[5] |
| | | older | 6.07[5] | 31.38[5] | 0.90[5] |

* WM= white matter, CTX=cortex

[a] Transferrin levels were determined by ELISA[7], or by SDS-PAGE and immunoassay with western blotting[5]. In both works transferrin levels were adjusted for total protein as determined with the Bio-Rad Protein Assay (Bio-Rad)[5,7].

[b] Ferritin levels were determined by immunoassays with slot blot technique, and were adjusted for total protein as determined with the Bio-Rad Protein Assay (Bio-Rad) in both works[5,9].

[c] Iron levels were determined by Ferrochem II Serum Iron / TIBC analyzer, and were adjusted for total protein as determined with the Bio-Rad Protein Assay (Bio-Rad)[5,7].

[d] To avoid very small and unreliable ROI segmentations, for the substantia nigra we used the entire midbrain, and for the gray/white superior temporal gyrus we used the entire temporal CTX/WM.

[e] The pallidum was removed from the main analysis (see **Sup. section 5**).

[f] These labels represent left-hemisphere ROIs, but the corresponding right-hemisphere labels were used as well. For each subject, we averaged the MRI measurements of both hemispheres of bilateral brain regions.

737 ## Western blot analysis of meningioma tissue:

738 Fresh frozen meningioma samples (40-50 mg) from 16 patients were homogenized in 200 µL of
739 RIPA buffer (Thermo Fisher Scientific) supplemented with protease inhibitor (Sigma-Aldrich,)
740 using a Bioruptor Pico sonication device (Diagenode) and protein extraction beads (Diagenode,
741 NJ, USA) according to the manufacturer instructions. Protein concentration was determined
742 using the Pierce assay (Thermo Fisher Scientific, MA, USA). Samples containing 20 µg of protein
743 were separated on 4-20% Tris-Glycine SDS-PAGE gel (Bio-Rad, CA, USA) and transferred to PVDF
744 membrane using Trans-Blot Turbo transfer system and transfer packs (Bio-Rad, Hercules, CA,
745 USA). Membranes were probed using Anti-Ferritin Light chain (#AB69090, Abcam, 1:1,000
746 dilution) and Anti-Transferrin (#AB82411, Abcam, 1:10,000 dilution) primary antibodies and
747 appropriate horseradish peroxidase-conjugated secondary antibody (Abcam, Cambridge, UK).
748 Membranes were treated with EZ-ECL (Biological industries, Beit-Ha'emek, Israel) and visualized
749 using ImageQuant LAS 4000 (GE Healthcare, IL, USA). Blot intensities were quantified using the
750 FIJI ImageJ software[78]. The ratio of transferrin/ferritin was based on the ratio in the blot
751 intensities of transferrin and ferritin. Due to the noisy nature of the western-blot analysis, we
752 averaged the estimates over six repetitions. We then used the median transferrin/ferritin ratio
753 across subjects (which was equal to 1) as the threshold between the two groups (low and high
754 transferrin/ferritin ratio).

755 ## RNA-sequencing of meningioma tissue:

756 RNA-seq libraries: Tumor samples from 17 patients (samples from 16 patients and a replicate for
757 one) were flash frozen and kept in -80c until processing. RNA isolation was done with the
758 following steps: First, frozen tissue was chopped and transferred with a 2ml lysis buffer
759 (Macherey-Nagel, 740955) five times through a needle attached to a 0.9 mm syringe to achieve

760 homogenization. Next, total RNA was extracted with NucleoSpin RNA kit (Macherey-Nagel,
761 740955), following the standard protocol. Finally, mRNA was isolated using the NEBNext Poly(A)
762 mRNA Magnetic Isolation Module (NEB E7490S), using 5ug of total RNA as an input and following
763 the standard protocol. The purified mRNA was used as input for cDNA library preparation, using
764 NEBNext® Ultra™ II Directional RNA Library Prep Kit for Illumina (NEB E7760), and following the
765 standard protocol. Quantification of the libraries was done by Qubit and TapeStation. Paired-end
766 sequencing of the libraries was performed on Nextseq 550.

767 Data processing: The demultiplexing of the samples was done with Illumina's bcl2fastq software.
768 The fastq files were next aligned to the human genome (hg38) using STAR and the transcriptome
769 alignment and gene counts were obtained with HTseq. For quality control RNAseQC software
770 was used. Quality control and data normalization was done in R using the DEseq2 package from
771 Bioconductor (version 3.13). The counts matrix per gene and sample were normalized using the
772 Variance stabilizing transformation. Genes with less than 5 counts were filtered out of the
773 analysis. The filtered and normalized matrix was used in all downstream analysis.

774 Gene set enrichment analysis (GSEA):

775 The final sequencing dataset included the expression of approximately 27,000 genes in 17 tumor
776 samples. We then excluded unannotated genes based on the gene ontology resource
777 (http://geneontology.org/) as well as genes with low (<6) expression levels, yielding 19,500
778 genes.

779 We used GSEA to further validate that the subset of highly correlated genes is not random, but
780 rather represents known biological pathways. For this aim, we calculated the correlations across
781 patients between the expression of each of the genes and one of the qMRI parameters (R1, R2*
782 or r1-r2* relaxivity). For each of the qMRI parameters, genes were ranked based on the *r* values
783 of the correlations, and the ranked list was used in the GSEAPranked toolbox[56,57]. The gene sets
784 databases used for this analysis included go, biocarta, kegg, pid, reactome and wikipathways.

785 The primary result of the GSEA is the enrichment score (ES), which reflects the degree to which a
786 gene set is overrepresented at the top or bottom of a ranked list of genes: A positive ES indicates
787 gene set enrichment at the top of the list, while a negative ES indicates gene set enrichment at
788 the bottom. The normalized ES (NES) accounts for differences in gene set size and in correlations
789 between gene sets and the expression dataset.

790 One tumor sample was excluded from the analysis, as the R1 and R2* values in the tumor were
791 relatively high, which led to the fact that no significantly enriched pathway were found for R1
792 and R2* (though we did detect significantly enriched pathways for the r1-r2* relaxivity).
793 Removing this outlier improved GSEA results for R1 and R2* and we therefore excluded this
794 subject.

Following the GSEA analysis, we found a total of 101 significantly enriched pathways for at least one of the R1, R2* and r1-r2* relaxivity. We then clustered those significantly enriched pathways using the "clustergram" function in MATLAB. In order to evaluate which genes are included within the top enrichment pathways for each MRI parameter, we used Leading Edge Analysis (as implemented in the GSEA toolbox).

## Data availability:

The data that support the findings of this study are available on request from the corresponding author (S.F.). The data are not publicly available due to them containing information that could compromise research participant privacy/consent.

## Code availability:

A toolbox for computing the r1-r2* relaxivity, including example data, is available at: [https://github.com/shirfilo/r1_r2s_rel_toolbox].

## References:

1. Thirupathi, A. & Chang, Y. Z. Brain iron metabolism and CNS diseases. in *Advances in Experimental Medicine and Biology* vol. 1173 1–19 (Springer New York LLC, 2019).

2. Bulk, M. *et al.* Quantitative comparison of different iron forms in the temporal cortex of Alzheimer patients and control subjects. *Sci. Rep.* **8**, 1–11 (2018).

3. Haacke, E. M. *et al.* Imaging iron stores in the brain using magnetic resonance imaging. *Magn. Reson. Imaging* **23**, 1–25 (2005).

4. Möller, H. E. *et al.* Iron, Myelin, and the Brain: Neuroimaging Meets Neurobiology. *Trends Neurosci.* (2019).

5. Connor, J. R., Snyder, B. S., Beard, J. L., Fine, R. E. & Mufson, E. J. Regional distribution of iron and iron-regulatory proteins in the brain in aging and Alzheimer's disease. *J. Neurosci. Res.* **31**, 327–335 (1992).

6. Connor, J. R., Boeshore, K. L., Benkovic, S. A. & Menzies, S. L. Isoforms of ferritin have a specific cellular distribution in the brain. *J. Neurosci. Res.* **37**, 461–465 (1994).

7. Loeffler, D. A. *et al.* Transferrin and Iron in Normal, Alzheimer's Disease, and Parkinson's

Disease Brain Regions. *J. Neurochem.* **65**, 710–716.

8. Zecca, L., Youdim, M. B. H., Riederer, P., Connor, J. R. & Crichton, R. R. Iron, brain ageing and neurodegenerative disorders. **5**, 863–873 (2004).

9. Connor, J. R., Snyder, B. S., Arosio, P., Loeffler, D. A. & LeWitt, P. A Quantitative Analysis of Isoferritins in Select Regions of Aged, Parkinsonian, and Alzheimer's Diseased Brains. *J. Neurochem.* **65**, 717–724 (1995).

10. Ward, R. J., Zucca, F. A., Duyn, J. H., Crichton, R. R. & Zecca, L. *The role of iron in brain ageing and neurodegenerative disorders*. *The Lancet Neurology* vol. 13 1045–1060 (2014).

11. Zarow, C., Lyness, S. A., Mortimer, J. A. & Chui, H. C. Neuronal loss is greater in the locus coeruleus than nucleus basalis and substantia nigra in Alzheimer and Parkinson diseases. *Arch. Neurol.* **60**, 337–341 (2003).

12. Sulzer, D. *et al.* Neuromelanin detection by magnetic resonance imaging (MRI) and its promise as a biomarker for Parkinson's disease. *NPJ Park. Dis.* **4**, 11 (2018).

13. Legendre, C. & Garcion, E. Iron metabolism: A double-edged sword in the resistance of glioblastoma to therapies. *Trends in Endocrinology and Metabolism* vol. 26 322–331 (2015).

14. Chen, Y., Fan, Z., Yang, Y. & Gu, C. Iron metabolism and its contribution to cancer (Review). *International Journal of Oncology* vol. 54 1143–1154 (2019).

15. Pfeifhofer-Obermair, C., Tymoszuk, P., Petzer, V., Weiss, G. & Nairz, M. Iron in the tumor microenvironment-connecting the dots. *Frontiers in Oncology* vol. 8 549 (2018).

16. Whittle, I. R., Smith, C., Navoo, P. & Collie, D. Meningiomas. in *Lancet* vol. 363 1535–1543 (2004).

17. Brem, F. *et al.* Magnetic iron compounds in the human brain: A comparison of tumour and hippocampal tissue. *J. R. Soc. Interface* **3**, 833–841 (2006).

18. Hänninen, M. M. *et al.* Expression of iron-related genes in human brain and brain tumors.

*BMC Neurosci.* **10**, 36 (2009).

19. Gelman, N., Ewing, J. R., Gorell, J. M., Spickler, E. M. & Solomon, E. G. Interregional variation of longitudinal relaxation rates in human brain at 3.0 T: Relation to estimated iron and water contents. *Magn. Reson. Med.* (2001).

20. Callaghan, M. F., Helms, G., Lutti, A., Mohammadi, S. & Weiskopf, N. A general linear relaxometry model of $R_1$ using imaging data. *Magn. Reson. Med.* **73**, 1309–1314 (2015).

21. Langkammer, C. *et al.* Quantitative MR imaging of brain iron: A postmortem validation study. *Radiology* **257**, 455–462 (2010).

22. Vymazal, J. *et al.* The relation between brain iron and NMR relaxation times: An in vitro study. *Magn. Reson. Med.* **35**, 56–61 (1996).

23. Cercignani, M., Dowell, N. G. & Tofts, P. S. *Quantitative MRI of the Brain : Principles of Physical Measurement*. (CRC Press, 2018).

24. Basser, P. J. & Pierpaoli, C. Microstructural and Physiological Features of Tissues Elucidated by Quantitative-Diffusion-Tensor MRI. *J. Magn. Reson. Ser. B* **111**, 209–219 (1996).

25. Weiskopf, N., Mohammadi, S., Lutti, A. & Callaghan, M. F. Advances in MRI-based computational neuroanatomy. *Curr. Opin. Neurol.* **28**, 313–322 (2015).

26. Weiskopf, N., Edwards, L. J., Helms, G., Mohammadi, S. & Kirilina, E. Quantitative magnetic resonance imaging of brain anatomy and in vivo histology. *Nat. Rev. Phys.* 1–19 (2021).

27. Ghadery, C. *et al.* R2* mapping for brain iron: Associations with cognition in normal aging. *Neurobiol. Aging* **36**, 925–932 (2015).

28. Vymazal, J. *et al.* T1 and T2 in the brain of healthy subjects, patients with Parkinson disease, and patients with multiple system atrophy: Relation to iron content. *Radiology* **211**, 489–495 (1999).

29. Lorio, S. *et al.* Disentangling in vivo the effects of iron content and atrophy on the ageing

human brain. *Neuroimage* **103**, 280–289 (2014).

30. Edwards, L. J., Kirilina, E., Mohammadi, S. & Weiskopf, N. Microstructural imaging of human neocortex in vivo. *NeuroImage* vol. 182 184–206 (2018).

31. Ogg, R. J. & Steen, R. G. Age-related changes in Brain T1 are correlated with iron concentration. *Magn. Reson. Med.* **40**, 749–753 (1998).

32. Wood, J. C., Fassler, J. D. & Meade, T. Mimicking liver iron overload using liposomal ferritin preparations. *Magn. Reson. Med.* **51**, 607–611 (2004).

33. Gossuin, Y., Muller, R. N. & Gillis, P. Relaxation induced by ferritin: a better understanding for an improved MRI iron quantification. *NMR Biomed.* **17**, 427–432 (2004).

34. Zhang, N. *et al.* A model for the analysis of competitive relaxation effects of manganese and iron in vivo. *NMR Biomed.* (2009).

35. Rohrer, M., Bauer, H., Mintorovitch, J., Requardt, M. & Weinmann, H.-J. Comparison of Magnetic Properties of MRI Contrast Media Solutions at Different Magnetic Field Strengths. *Invest. Radiol.* **40**, (2005).

36. Kiselev, V. G. & Novikov, D. S. Transverse NMR relaxation in biological tissues. *NeuroImage* vol. 182 149–168 (2018).

37. Brammerloh, M. *et al.* Measuring the iron content of dopaminergic neurons in substantia nigra with MRI relaxometry. *Neuroimage* **239**, 118255 (2021).

38. Birkl, C. *et al.* The influence of iron oxidation state on quantitative MRI parameters in post mortem human brain. *Neuroimage* **220**, (2020).

39. Callaghan, M. F. *et al.* Widespread age-related differences in the human brain microstructure revealed by quantitative magnetic resonance imaging. *Neurobiol. Aging* **35**, 1862–1872 (2014).

40. Heath, F., Hurley, S. A., Johansen-Berg, H. & Sampaio-Baptista, C. Advances in noninvasive myelin imaging. *Dev. Neurobiol.* **78**, 136–151 (2018).

41. Lutti, A., Dick, F., Sereno, M. I. & Weiskopf, N. Using high-resolution quantitative mapping of R1 as an index of cortical myelination. *Neuroimage* **93**, 176–188 (2014).

42. Stüber, C. *et al.* Myelin and iron concentration in the human brain: A quantitative study of MRI contrast. *Neuroimage* **93**, 95–106 (2014).

43. Callaghan, M. F., Helms, G., Lutti, A., Mohammadi, S. & Weiskopf, N. A general linear relaxometry model of R1 using imaging data. *Magn. Reson. Med.* **73**, 1309–14 (2015).

44. Kirilina, E. *et al.* Superficial white matter imaging: Contrast mechanisms and whole-brain in vivo mapping. *Sci. Adv.* **6**, aaz9281 (2020).

45. Mezer, A. *et al.* Quantifying the local tissue volume and composition in individual brains with magnetic resonance imaging. *Nat. Med.* **19**, 1667–72 (2013).

46. Mohammadi, S. & Callaghan, M. F. Towards in vivo g-ratio mapping using MRI: Unifying myelin and diffusion imaging. *J. Neurosci. Methods* **348**, 108990 (2021).

47. Berman, S., West, K. L., Does, M. D., Yeatman, J. D. & Mezer, A. A. Evaluating g-ratio weighted changes in the corpus callosum as a function of age and sex. *Neuroimage* **182**, 304–313 (2018).

48. Mancini, M. *et al.* An interactive meta-analysis of MRI biomarkers of Myelin. *Elife* **9**, 1–23 (2020).

49. Piredda, G. F., Hilbert, T., Thiran, J. & Kober, T. Probing myelin content of the human brain with MRI: A review. *Magn. Reson. Med.* **85**, 627–652 (2021).

50. Lévy, S. *et al.* Test-retest reliability of myelin imaging in the human spinal cord: Measurement errors versus region- and aging-induced variations. *PLoS One* **13**, (2018).

51. Peters, J. M. *et al.* White matter mean diffusivity correlates with myelination in tuberous sclerosis complex. *Ann. Clin. Transl. Neurol.* **6**, 1178–1190 (2019).

52. Essig, M. *et al.* Contrast-Enhanced Magnetic Resonance Imaging of Central Nervous System Tumors. *Top. Magn. Reson. Imaging* **17**, 89–106 (2006).

53. Gulani, V., Calamante, F., Shellock, F. G., Kanal, E. & Reeder, S. B. Gadolinium deposition in the brain: summary of evidence and recommendations. *The Lancet Neurology* vol. 16 564–570 (2017).

54. McDonald, R. J. *et al.* Gadolinium deposition in human brain tissues after contrast-enhanced MR imaging in adult patients without intracranial abnormalities. *Radiology* **285**, 546–554 (2017).

55. Falk Delgado, A. A. *et al.* Diagnostic value of alternative techniques to gadolinium-based contrast agents in MR neuroimaging—a comprehensive overview. *Insights into Imaging* vol. 10 1–15 (2019).

56. Subramanian, A. *et al.* Gene set enrichment analysis: A knowledge-based approach for interpreting genome-wide expression profiles. *Proc. Natl. Acad. Sci. U. S. A.* **102**, 15545–15550 (2005).

57. Mootha, V. K. *et al.* PGC-1α-responsive genes involved in oxidative phosphorylation are coordinately downregulated in human diabetes. *Nat. Genet.* **34**, 267–273 (2003).

58. Fang, L. *et al.* The immune cell infiltrate populating meningiomas is composed of mature, antigen-experienced T and B cells. *Neuro. Oncol.* **15**, 1479–1490 (2013).

59. Comtesse, N. *et al.* Complex humoral immune response against a benign tumor: Frequent antibody response against specific antigens as diagnostic targets. *Proc. Natl. Acad. Sci. U. S. A.* **102**, 9601–9606 (2005).

60. Chiabrando, D., Vinchi, F., Fiorito, V., Mercurio, S. & Tolosano, E. Heme in pathophysiology: A matter of scavenging, metabolism and trafficking across cell membranes. *Front. Pharmacol.* **5**, 1–24 (2014).

61. Rosager, A. M. *et al.* Transferrin receptor-1 and ferritin heavy and light chains in astrocytic brain tumors: Expression and prognostic value. *PLoS One* **12**, e0182954 (2017).

62. Sanchez, M. *et al.* Iron regulation and the cell cycle: identification of an iron-responsive element in the 3'-untranslated region of human cell division cycle 14A mRNA by a refined

microarray-based screening strategy. *J Biol Chem.* **281**, 22865–74 (2006).

63. De Leõn-Rodríguez, L. M., Martins, A. F., Pinho, M. C., Rofsky, N. M. & Sherry, A. D. Basic MR relaxation mechanisms and contrast agent design. *J. Magn. Reson. Imaging* **42**, 545–565 (2015).

64. Zecca, L. *et al.* The role of iron and copper molecules in the neuronal vulnerability of locus coeruleus and substantia nigra during aging. *Proc. Natl. Acad. Sci.* **101**, 9843–9848 (2004).

65. Trujillo, P. *et al.* Contrast mechanisms associated with neuromelanin-MRI. *Magn. Reson. Med.* **78**, 1790–1800 (2017).

66. Taege, Y. *et al.* Assessment of mesoscopic properties of deep gray matter iron through a model-based simultaneous analysis of magnetic susceptibility and R2* - A pilot study in patients with multiple sclerosis and normal controls. *Neuroimage* **186**, 308–320 (2019).

67. Zhou, Z. & Lu, Z. R. Gadolinium-based contrast agents for magnetic resonance cancer imaging. *Wiley Interdisciplinary Reviews: Nanomedicine and Nanobiotechnology* vol. 5 1–18 (2013).

68. Filo, S. *et al.* Disentangling molecular alterations from water-content changes in the aging human brain using quantitative MRI. *Nat. Commun.* **10**, (2019).

69. Shtangel, O. & Mezer, A. A. A phantom system for assessing the effects of membrane lipids on water proton relaxation. *NMR Biomed.* **33**, (2020).

70. Mezer, A., Rokem, A., Berman, S., Hastie, T. & Wandell, B. A. Evaluating quantitative proton-density-mapping methods. *Hum. Brain Mapp.* **37**, 3623–3635 (2016).

71. Weiskopf, N. *et al.* Quantitative multi-parameter mapping of R1, PD*, MT, and R2* at 3T: A multi-center validation. *Front. Neurosci.* (2013).

72. Smith, S. M. *et al.* Advances in functional and structural MR image analysis and implementation as FSL. *Neuroimage* (2004).

73. Behrens, T. E. J. *et al.* Characterization and propagation of uncertainty in diffusion-

weighted MR imaging. *Magn. Reson. Med.* (2003).

74. Andersson, J. L. R., Skare, S. & Ashburner, J. How to correct susceptibility distortions in spin-echo echo-planar images: Application to diffusion tensor imaging. *Neuroimage* **20**, 870–88 (2003).

75. Andersson, J. L. R. & Sotiropoulos, S. N. An integrated approach to correction for off-resonance effects and subject movement in diffusion MR imaging. *Neuroimage* **125**, 1063–1078 (2016).

76. Fischl, B. FreeSurfer. *Neuroimage* **62**, 774–781 (2012).

77. Patenaude, B., Smith, S. M., Kennedy, D. N. & Jenkinson, M. A Bayesian model of shape and appearance for subcortical brain segmentation. *Neuroimage* **56**, 907–22 (2011).

78. Schindelin, J. *et al.* Fiji: An open-source platform for biological-image analysis. *Nature Methods* vol. 9 676–682 (2012).

79. Donahue, K. M., Weisskoff, R. M. & Burstein, D. Water diffusion and exchange as they influence contrast enhancement. *J. Magn. Reson. Imaging* **7**, 102–110 (1997).

80. Rooney, W. D. *et al.* Magnetic field and tissue dependencies of human brain longitudinal1H2O relaxation in vivo. *Magn. Reson. Med.* **57**, 308–318 (2007).

81. Fullerton, G. D., Potter, J. L. & Dornbluth, N. C. NMR relaxation of protons in tissues and other macromolecular water solutions. *Magn. Reson. Imaging* **1**, 209–26 (1982).

82. Gossuin, Y., Gillis, P., Muller, R. N. & Hocq, A. Relaxation by clustered ferritin: a model for ferritin-induced relaxation in vivo. *NMR Biomed.* **20**, 749–756 (2007).

83. Ghugre, N. R., Coates, T. D., Nelson, M. D. & Wood, J. C. Mechanisms of Tissue–Iron Relaxivity: Nuclear Magnetic Resonance Studies of Human Liver Biopsy Specimens. *Magn. Reson. Med.* **54**, 1185 (2005).

84. Dlháň, Ľ., Kopáni, M. & Boča, R. Magnetic properties of iron oxides present in the human brain. *Polyhedron* **157**, 505–510 (2019).

85. Erikson, K. M., Syversen, T., Steinnes, E. & Aschner, M. Globus pallidus: A target brain region for divalent metal accumulation associated with dietary iron deficiency. *J. Nutr. Biochem.* **15**, 335–341 (2004).

# Supplementary Materials for

# "Uncovering molecular iron compounds in the living human brain"

# Contents

# Supplementary Figure 1

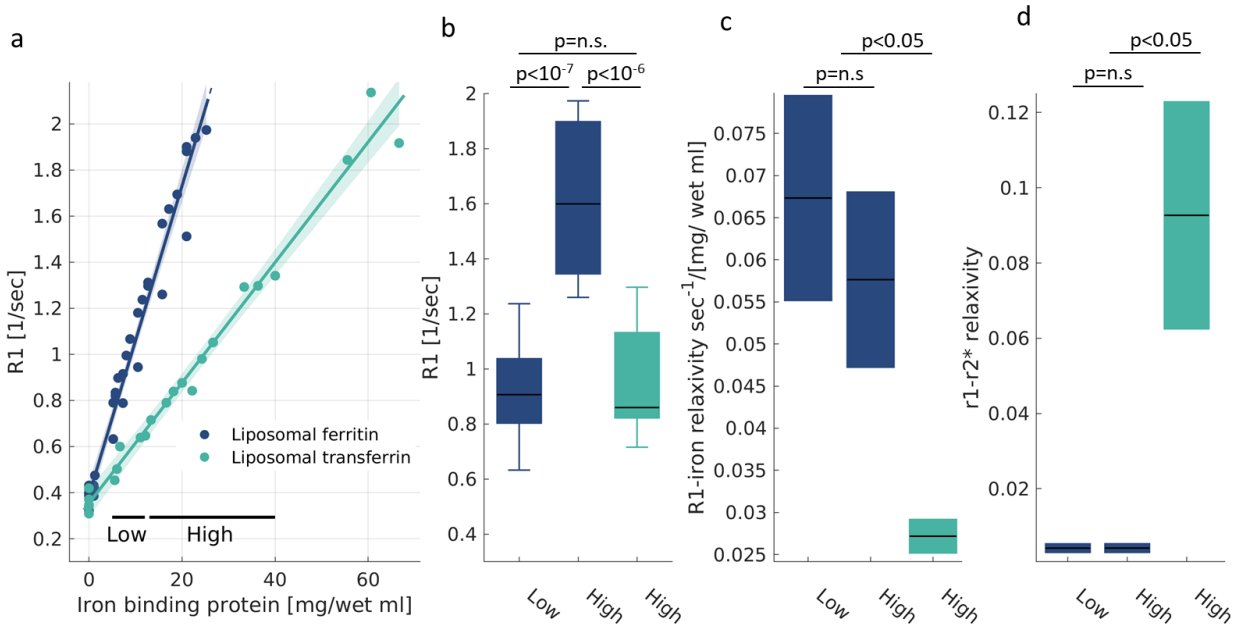


***Sup. Figure 1: The effect of iron concentration on different MR estimations. (a)*** *The dependency of R1 on the iron-binding protein concentration for liposomal ferritin and liposomal transferrin. Data points represent liposomal samples with varying iron-binding protein concentrations relative to the water fraction ([mg/wet ml]). The linear relationships between relaxation rates and iron-binding protein concentrations are marked by lines. The slopes of these lines are the iron relaxivities. Shaded areas represent the 95% confidence bounds.* ***(b)*** *The ambiguity in R1; R1 changes as a function of both iron compound and iron concentration. This is shown by calculating the median R1 value over samples with high and low iron-binding protein concentrations (marked in (a); concentration ranges were chosen so that the number of data points in each range is similar). We find that R1 is greater for a higher ferritin concentration than for a lower ferritin concentration, but also find that R1 is greater for ferritin than for transferrin. For each box, the central line marks the median, the box extends vertically between the 25th and 75th percentiles, and the whiskers extend to the most extreme data points.* ***(c-d)*** *The ambiguity in R1 is resolved by the R1-iron relaxivity (c) and the r1-r2* (d), which are consistent when computed over higher or lower ferritin concentrations, and are consistently different from the iron relaxivity of transferrin regardless the concentration. For each box, the central lines marks the iron relaxivity, and the box shows the 95% confidence bounds of the linear fit. p-values are for the ANCOVA test corrected for multiple comparisons.*

# Supplementary Section 1: The dependency of R1 and R2* on the iron concentration.

In ***Figure 1*** we computed the iron relaxivity as the dependency of R1 and R2* on the concentration of iron-binding proteins. We showed that different compounds of iron have different relaxivities. However, different proteins bind different amounts of iron. For example, ferritin binds three orders of magnitude more iron ions than does transferrin[3]. Therefore, we wanted to exclude the possibility that the different iron ion concentrations drive the different relaxivities of ferritin and transferrin.

We verified that the relaxivity changes according to the molecular type of iron, even when accounting for discrepancies in iron loading. We estimated the iron ion concentrations for ferritin and transferrin (see Methods section "Estimation of total iron content in phantoms") and tested whether those values can explain their different iron relaxivities. Importantly, after computing the iron relaxivity as the dependency of relaxation rates on the iron ion concentrations (rather than the concentration of iron-binding proteins), we still find that different iron compounds have distinct relaxivities (**Sup. Figure 2**, $p(ANCOVA)<10^{-44}$).

To further stress the sensitivity of the r1-r2* relaxivity to the type of iron, we compared the relaxivity of liposomal ferrous iron ($Fe^{2+}$) and iron bound to liposomal transferrin (**Sup. Figure 3**). Unlike ferritin and transferrin, these two iron compounds have relatively similar iron ion concentrations. Yet we find that they produce different iron relaxivities ($p(ANCOVA)<10^{-4}$). The r1-r2* relaxivities of these two iron compounds are different as well ($p(ANCOVA)<0.05$). Therefore, the iron relaxivity and the r1-r2* relaxivity are changing as a function of the molecular type of iron, even when accounting for the differences in iron binding between the different iron compounds.

# Supplementary Figure 2

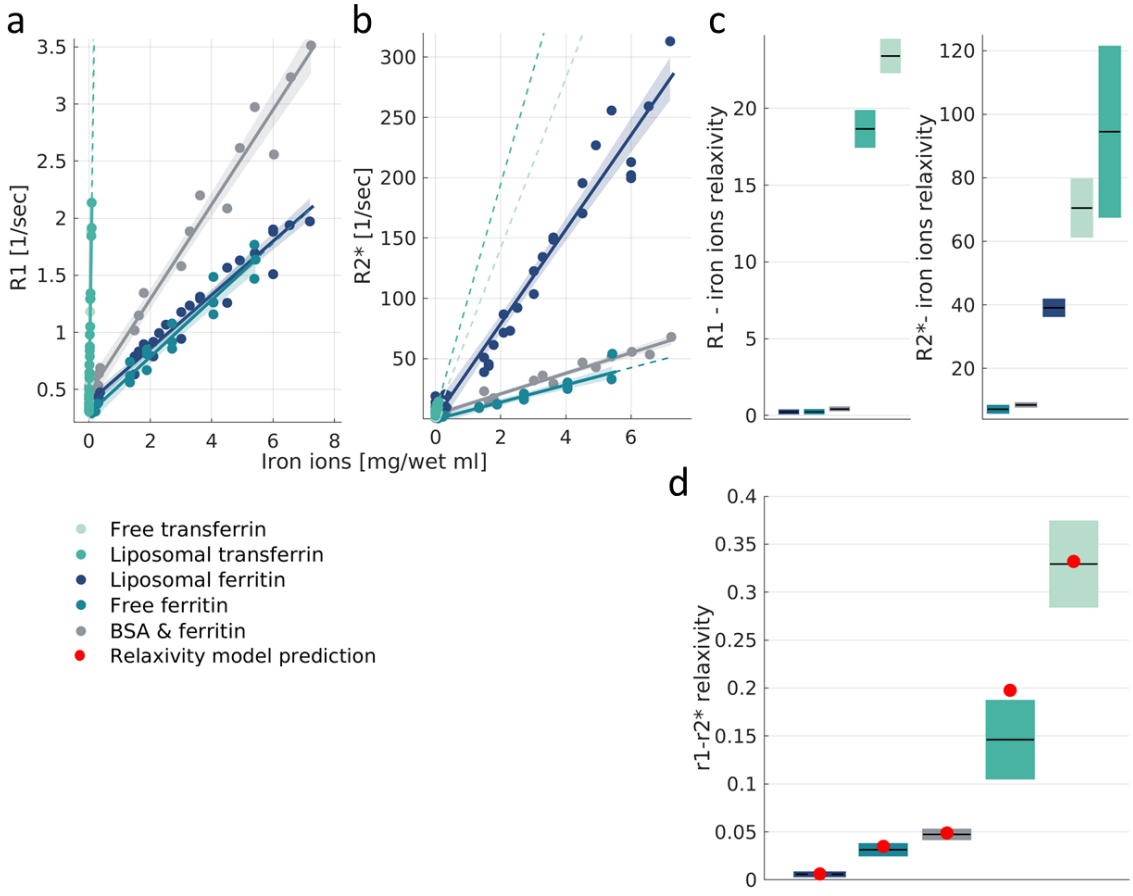


***Sup. Figure 2: The iron relaxivity and the r1-r2* relaxivity are sensitive to the molecular type of iron regardless of the differences in iron-binding. (a-b)*** *The dependency of R1 and R2* on the estimated iron concentration (see method section "Estimation of total iron content in phantoms") for five different iron compounds: free ferritin, liposomal-ferritin, Bovine Serum Albumin (BSA)-ferritin mixture, free transferrin and liposomal transferrin. Data points represent samples with varied estimated iron ion concentrations relative to the water fraction ([mg/wet ml]). The linear relationships between relaxation rates and iron concentration are marked by lines. The slopes of these lines are the iron relaxivities. Dashed lines represent extrapolations the linear fits, and shaded areas represent the 95% confidence bounds.* ***(c)*** *The iron relaxivities of R1 and R2* are different for different iron compounds ($p(ANCOVA)<10^{-44}$). Iron relaxivity is calculated here based on the estimated iron concentration (and not iron-binding proteins concentrations, as in* Figure 1*). To do so, we use the slope of the linear relationships shown in (a,b), expressed in [sec-1/(mg/wet ml)]. For each box the central lines marks the iron relaxivity, and the box shows the 95% confidence bounds of the linear fit.* ***(d)*** *The theoretical model successfully predicts the r1-r2* relaxivity even when it is based on the estimated iron concentration (and not iron-binding proteins concentrations, as in* Figure 1*). The model's prediction is based on the ratio between the iron relaxivities of R1 and R2* as shown in (c). For each box the central line marks the r1-r2* relaxivity, and the box shows the 95% confidence bounds of the linear fit. Red dots represent the prediction of the theoretical model.*

# Supplementary Figure 3

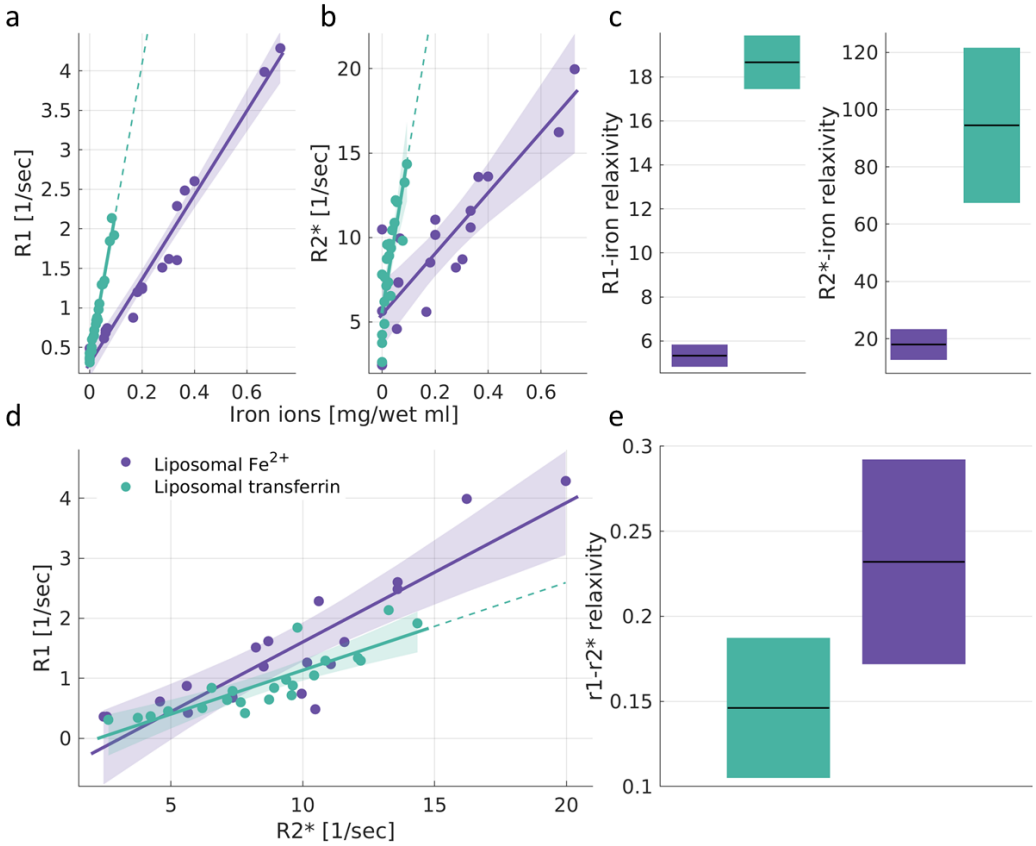


***Sup. Figure 3: The iron relaxivity and the r1-r2* relaxivity are sensitive to the molecular type of iron for a similar iron concentration. (a-b)*** *The dependency of R1 and R2* on the estimated iron concentration for two different iron compounds: liposomal transferrin (purple) and liposomal $Fe^{2+}$ (green). Data points represent liposomal samples with varying iron ion concentrations relative to the water fraction ([mg/wet ml]). The linear relationships between relaxation rates and iron ion concentration are marked by lines. The slopes of these lines are the iron relaxivities. Dashed lines represent extrapolations of the linear fits. Shaded areas represent the 95% confidence bounds.* ***(c)*** *The iron relaxivity of R1 and R2* is different for different iron compounds ($p(ANCOVA)<10^{-4}$). Iron relaxivity is calculated by taking the slope of the linear relationships shown in (a,b), and is measured in [sec-1/(mg/wet ml)]. For each box, the central line marks the iron relaxivity, and the box shows the 95% confidence bounds of the linear fit.* ***(d)*** *The dependency of R1 on R2* for different iron compounds. Data points represent samples with varying concentrations. The linear relationships between R1 and R2* are marked by lines. The slopes of these lines are the r1-r2* relaxivities. Dashed lines represent extrapolations of the linear fits. Shaded areas represent the 95% confidence bounds.* ***(e)*** *The r1-r2* relaxivity is different for different iron compounds ($p(ANCOVA)<0.05$). For each box, the central line marks the r1-r2* relaxivity, and the box shows the 95% confidence bounds of the linear fit.*

# Supplementary Figure 4

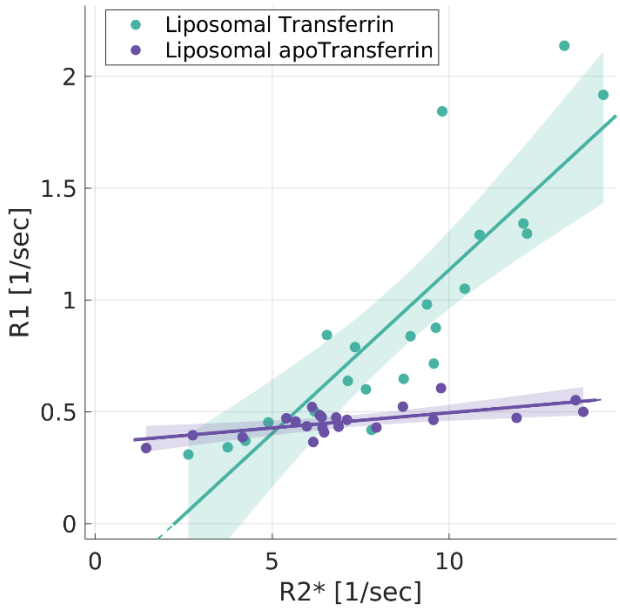


***Sup. Figure 4: Validating the sensitivity of the iron relaxivity and the r1-r2* relaxivity to the paramagnetic properties of transferrin.*** *Data points represent liposomal samples with varying concentrations of transferrin (green) and apo-transferrin (transferrin which is not bound to iron, in purple). The linear relationships between R1 and R2* are marked by lines. The slopes of these lines are the r1-r2* relaxivities. Shaded areas represent the 95% confidence bounds. Apo-transferrin with no iron has lower r1-r2* relaxivity compared to iron-bound transferrin ($p(ANCOVA)<10^{-8}$). Therefore, the r1-r2* relaxivity is sensitive to the paramagnetic properties of iron-binding proteins and not to the proteins themselves.*

## Supplementary Section 2: The dependency of the iron relaxivity on the liposomal fraction.

R1 and R2* measured in the brain are known to be sensitive to myelin content[4,19,25,29,39–41]. Myelin is composed mainly of lipids, though it also includes proteins. We tested the effect of the myelin fraction on iron relaxivity by varying the liposomal and protein (BSA) fractions in our phantoms.

In histological studies of brain iron, the iron concentrations often are reported relative to the wet weight, as this is considered more accurate[4]. To match our *in vitro* analysis to brain histology as much as possible, we calculated the iron-binding proteins' concentrations relative to the water fraction ([mg/wet ml]). This was done by computing the ratio between the iron concentration and the water fraction (which is complementary to the liposomal or protein fractions). The iron relaxivities shown in **Figure 1** were therefore calculated as the linear dependencies of relaxation rates on the iron-binding protein concentration relative to the water fraction. **Sup. Figure 5** presents the effect of the variable liposomal (or BSA) fractions on the iron relaxivity and on the r1-r2* relaxivity. When iron-binding protein concentrations were not calibrated to the water fraction (units of [mg/ml]), some variability in R1 and R2* values for different liposomal (or BSA) fractions was observed (**Sup. Figure 5a,c**). However, the iron relaxivities of different iron compounds were still distinct, despite the liposomal (or BSA) fractions' variability. Calibrating the iron-binding protein concentrations to the water fraction (units of [mg/wet ml]) further eliminated the effect of the variable liposomal (or BSA) fractions on the iron relaxivities (**Sup. Figure 5b,d**). This is evident by the alignment of the data points with different liposomal (or BSA) fractions along the iron relaxivity's linear fits. Therefore, while the non-water fraction has an effect on the relaxation rates, it does not disrupt the sensitivity of the iron relaxivities to the molecular type of iron.

We further estimated the effect of the liposomal (or BSA) fractions on the r1-r2* relaxivity. In **Sup. Figure 5e** we show the same r1-r2* relaxivities presented in **Figure 1**, but now the liposomal (or BSA) fractions are indicated by different symbols. Similarly to the iron relaxivities, the r1-r2* relaxivities of different iron compounds were distinct, even though they were calculated across varying liposomal (or BSA) fractions. Moreover, we estimated the r1-r2* relaxivity separately for

each liposomal (or BSA) fraction (**Sup. Figure 5f**). We find that the r1-r2* relaxivity differences between iron compounds are greater than the differences within each iron compound for the variable liposomal (or BSA) fractions.

The dependency of R1 on the macromolecular tissue volume (MTV) was associated with lipid composition in our previous work[68]. We tested this finding in the presence of iron by calculating the R1-MTV dependencies for different types of lipids mixed with iron (**Sup. Figure 6a-b**). Notably, in the current study we sampled only three liposomal fractions, and therefore the variation in the iron concentration between the samples was much richer than the variation in lipid concentration. Still, we were able to replicate our finding regarding the sensitivity of the R1-MTV dependency to lipid type. We find that the R1-MTV dependencies are different for two types of lipid mixtures (phosphatidylcholine (PC) and phosphatidylcholine-sphingomyelin (PC-SM)) mixed with ferrous ($Fe^{2+}$) iron (**Sup. Figure 6a**). In the presence of ferritin, the difference between the R1-MTV dependencies of the two lipids is smaller (**Sup. Figure 6b**).

Unlike the R1-MTV dependency, the r1-r2* relaxivity is insensitive to the lipid composition (**Sup. Figure 6c**): different lipids mixed with ferritin have a similar r1-r2* relaxivity (p(ANCOVA)=0.11). The variability in the r1-r2* relaxivity was much bigger when comparing these different liposomal ferritin samples to liposomal transferrin ($p(ANOCVA)<10^{-7}$). Compared to the R1-MTV dependencies, we find that the r1-r2* relaxivity provides a better distinction between iron compounds. **Sup. Figure 7** presents the r1-r2* relaxivities and the R1-MTV dependencies for different iron compounds. ANCOVA tests for the R1-MTV dependencies reveal that the only significant distinction is between the BSA-ferritin mixture and all the liposomal iron compounds ($p(ANCOVA)<10^{-5}$). The rest of the iron compounds are indistinguishable in terms of their R1-MTV dependencies. On the contrary, all iron compounds were distinguishable in terms of their r1-r2* relaxivity ($p(ANCOA)<10^{-32}$).

## Supplementary Figure 5

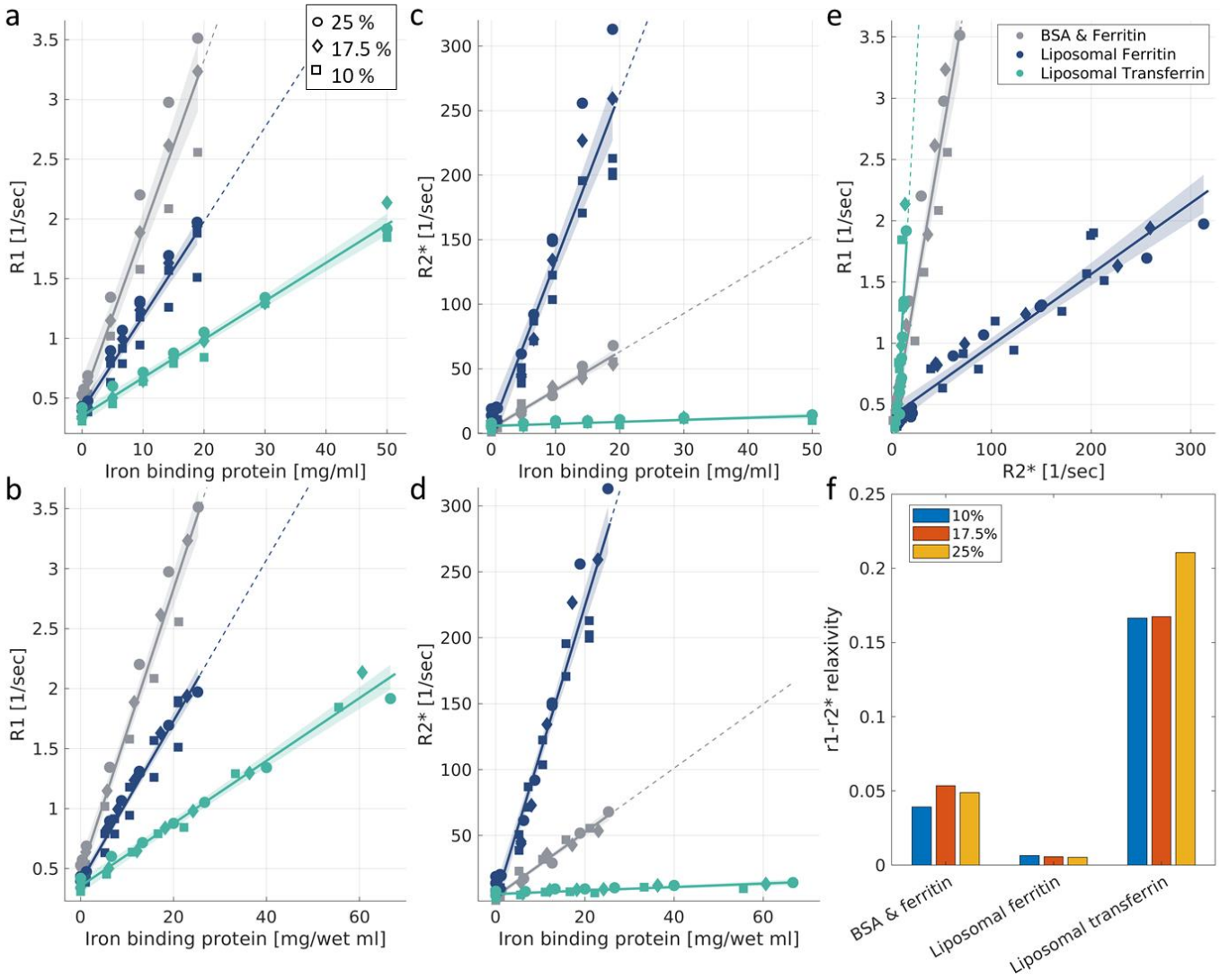


***Sup. Figure 5: Relaxivities are stable across liposomal or BSA fractions. (a)*** *The dependency of R1 on the iron-binding protein concentration for different liposomal (or BSA) fractions (different symbols) and different iron compounds (different colors). The x-axis represents the absolute concentration of iron-binding proteins (not relative to the water concentration, as in b). The linear relationships between relaxation rates and iron-binding protein concentration are marked by lines. The slopes of these lines are defined as the iron relaxivities. R1 values are affected by the variable liposomal (or BSA) fractions, but the iron relaxivities of different iron compounds are still distinct, regardless of this manipulation. Dashed lines represent extrapolations of the linear fits. Shaded areas represent the 95% confidence bounds.* ***(b)*** *The dependency of R1 on the iron-binding protein concentration for different liposomal (or BSA) fractions (different symbols) and different iron compounds (different colors). Here the x-axis represents the concentration of iron-binding proteins relative to the water fraction (which varies with the liposomal or BSA fraction). This estimation, in units of [mg/wet ml], further eliminates the effect of the liposomal (or BSA) fraction on the iron relaxivities. This is evident by the alignment of the data points with different liposomal (or BSA) fractions (different symbols) along the iron relaxivity linear fit.* ***(c-d)*** *A similar analysis for the R2*-iron relaxivity. The effect of the different liposomal (or BSA) fractions on the R2*-iron*

*relaxivity is eliminated by the calculation of the iron-binding proteins concentration relative to the water fraction ([mg/wet ml]).* ***(e)*** *The dependency of R1 on R2* for different liposomal (or BSA) fractions (different symbols) and different iron compounds (different colors). The r1-r2* relaxivities of different iron compounds are distinct even when calculated across liposomal (or BSA) fractions.* ***(f)*** *The r1-r2* relaxivity (y-axis) for different compounds of iron (liposomal ferritin, liposomal transferrin and BSA-ferritin mixture) in three different liposomal (or BSA) fractions (colors). The differences in the r1-r2* relaxivity between iron compounds are greater than the differences within each iron compound for the variable liposomal (or BSA) fractions.*

## Supplementary Figure 6

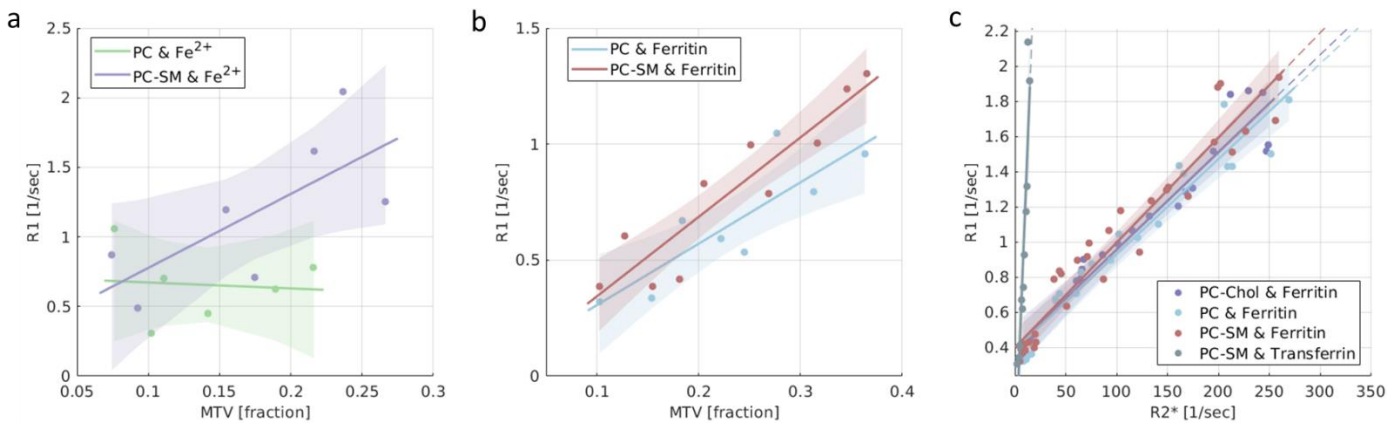


***Sup. Figure 6: The r1-r2* relaxivity is stable for different types of lipids, while the R1-MTV dependency is sensitive to the lipid type.*** ***(a)*** *The dependency of R1 on MTV for an iron ion compound ($Fe^{2+}$) mixed with two different lipids: phosphatidylcholine (PC, green) and a mixture of PC-sphingomyelin (PC-SM, blue). This result replicates the sensitivity of the MTV dependencies to lipid types[68] in $Fe^{2+}$-containing phantoms.* ***(b)*** *The dependency of R1 on MTV for a second iron compound (ferritin) mixed with the same two lipids (PC and PC-SM).* ***(c)*** *The dependency of R1 on R2* (r1-r2* relaxivity) for four different iron-lipid mixtures: ferritin-PC ferritin-PC-SM, transferrin-PC-SM and ferritin-PC-cholesterol (PC-Chol, blue). The r1-r2* relaxivity is similar for the different lipid types mixed with ferritin, and the main difference is between the iron binding proteins; i.e., transferrin sample and the ferritin samples.*

# Supplementary Figure 7

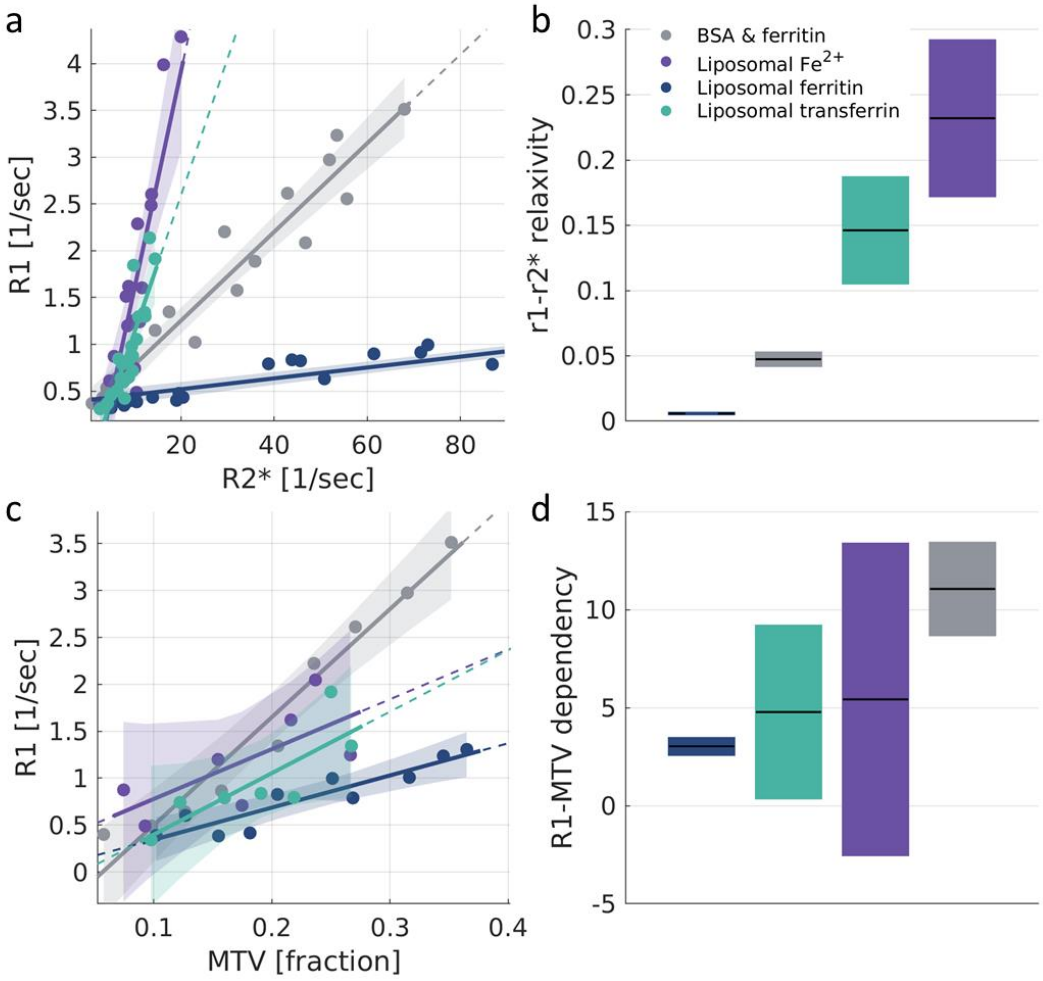


***Sup. Figure 7: Iron compounds are less distinguishable with MTV dependencies than with the r1-r2* relaxivity. (a)*** *The dependency of R1 on R2* (r1-r2* relaxivity) for different iron compounds: liposomal-ferritin, BSA-ferritin mixture, liposomal transferrin and liposomal $Fe^{2+}$. Liposomal samples are based on PC-sphingomyelin. Data points represent samples with varying iron compounds concentrations relative to the water fraction. The linear relationships between relaxation rates are marked by lines, whose slopes represent the r1-r2* relaxivities. Dashed lines represent extrapolations of the linear fits. Shaded areas represent the 95% confidence bounds. The x-axis presents only partial range of R2* values, similar to* **Figure 1d** *(for the entire R2* range, see the inset of* **Figure 1d***).* ***(b)*** *The r1-r2* relaxivities are different for these four iron compounds. For each box, the central line marks the r1-r2* relaxivity, and the box shows the 95% confidence bounds of the linear fit.* ***(c)*** *The dependency of R1 on MTV for these four iron compounds. Data points represent samples with varying iron compounds concentrations relative to the water fraction. The linear relationships between R1 and MTV are marked by lines, whose slopes represent the R1-MTV dependencies. Dashed lines represent extrapolations of the linear fits. Shaded areas represent the 95% confidence bounds.* ***(d)*** *The R1-MTV dependencies for the four iron compounds. For each box, the central line marks the R1-MTV dependency, and the box showes the 95% confidence bounds of the linear fit.*

## Supplementary Figure 8

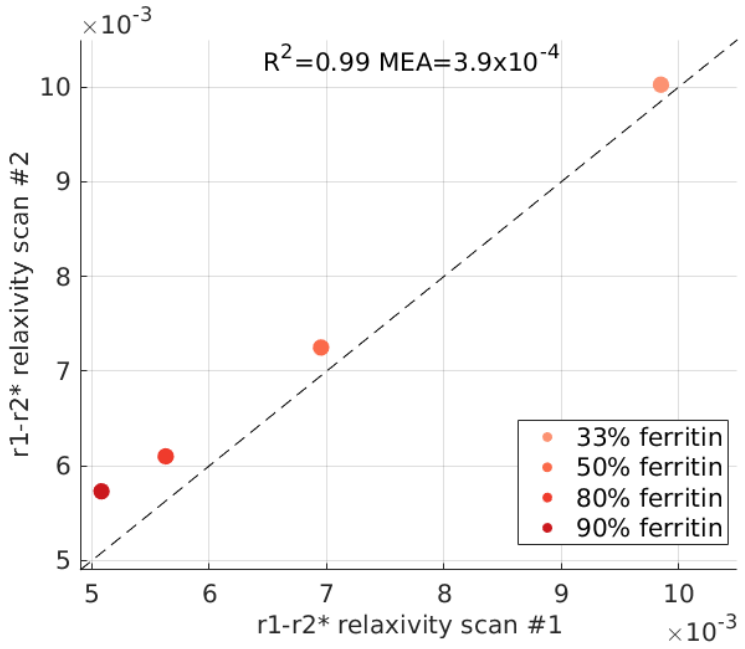


***Sup. Figure 8: The reproducibility of the r1-r2* relaxivity measurement in vitro.*** *The reproducibility of the r1-r2* relaxivity measurement for in vitro ferritin-transferrin mixtures was estimated based on scan-rescan experiments. Four different transferrin-ferritin mixtures were scanned twice (on different days). Each mixture experiment had a different transferrin-ferritin fraction (different colors, legend shows the percentage of ferritin in the mixture). The r1-r2* relaxivity of each mixture experiment was calculated over samples with the same transferrin-ferritin fraction but varying total iron-binding protein concentrations. Figure shows the r1-r2* relaxivity values measured in the first scan (x-axis) vs. the r1-r2* relaxivity values measured in the second scan (y-axis) for each in vitro experiment. Dashed line is the identity line. The measured scan-rescan mean absolute error (MAE) represents an experimental estimate of the detection limit of the r1-r2* relaxivity.*

## Supplementary Figure 9

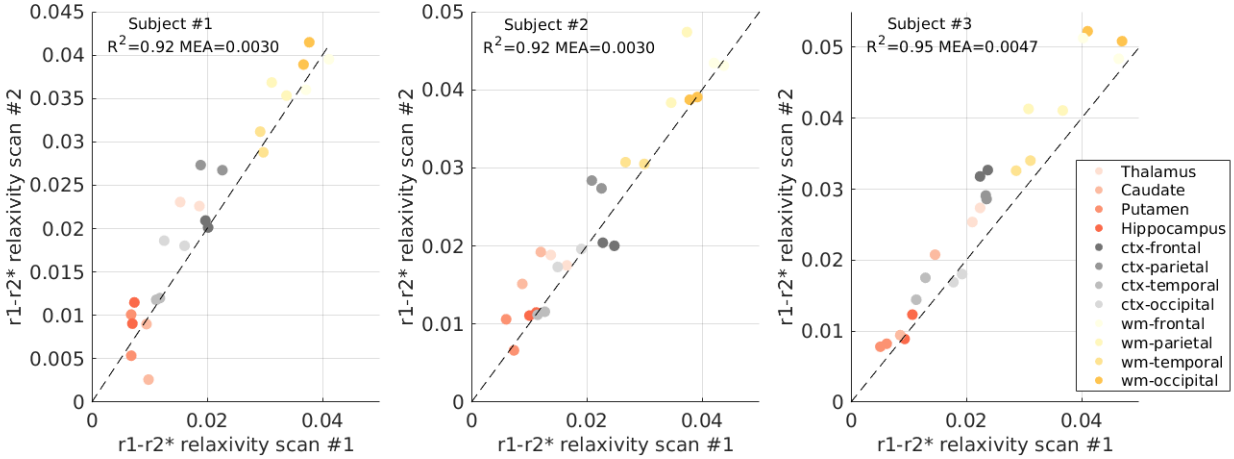


***Sup. Figure 9: The reproducibility of the r1-r2* relaxivity measurement in the in vivo brain.*** *The reproducibility of the r1-r2* relaxivity measurement in the in vivo brain was estimated based on scan-rescan experiments in three human subjects. Each subject was scanned twice in the MRI (on different days). The r1-r2* relaxivity was calculated for each scan in 12 different brain regions (different colors) in both hemispheres. Panels show the r1-r2* relaxivity values measured in the first scan (x-axis) vs. the r1-r2* relaxivity values measured in the scanned scan for each subject. Dashed line is the identity line. The measured scan-rescan mean absolute error (MAE) represents an experimental estimate of the detection limit of the r1-r2* relaxivity.*

## Supplementary Section 3: Voxel-wise r1-r2* relaxivity map.

**Figure 2** compares the contrast of R1 and R2* in the brain to the new contrast generated by the r1-r2* relaxivity. The measurement of the r1-r2* relaxivity is calculated across all the voxels of a specific ROI in the brain (see "r1-r2* relaxivity computation for ROIs in the human brain" in Methods). Therefore, the contrasts are presented across different entire brain regions. In order to demonstrate a voxel-wise comparison of the r1-r2* relaxivity contrast to the R1 and R2* contrasts, we generated a representative map of the local r1-r2* relaxivity in a healthy young subject. For this purpose, we used a moving-window approach, in which the r1-r2* relaxivity of each voxel is based on the local linear dependency of R1 on R2* in that voxel and all its neighboring voxels (125 voxels total, for more details see "Generating voxel-wise r1-r2* relaxivity maps" in Methods). A comparison of the local r1-r2* relaxivity map to the R1 and R2* maps can be seen in **Sup. Figure 10**. Similarly to the ROI-based approach (**Figure 2**), this voxel-wise comparison also shows that the r1-r2* relaxivity generates a new contrast in the brain compared to R1 and R2*. Interestingly, this local relaxivity contrast highlights the differences between superficial and deep white matter. Such contrast was previously suggested to be driven by the microscopic iron distribution[44]. Notably, the moving-window approach used for calculating the local r1-r2* relaxivity leads to inherent smoothing. As a result, this approach is sensitive to partial volume effects for voxels on the border between tissue types. In addition, the local computation of the r1-r2* relaxivity use fewer voxels compared to the ROI-based approach and is therefore less stable. As a result, some of the calculated values are negative.

## Supplementary Figure 10

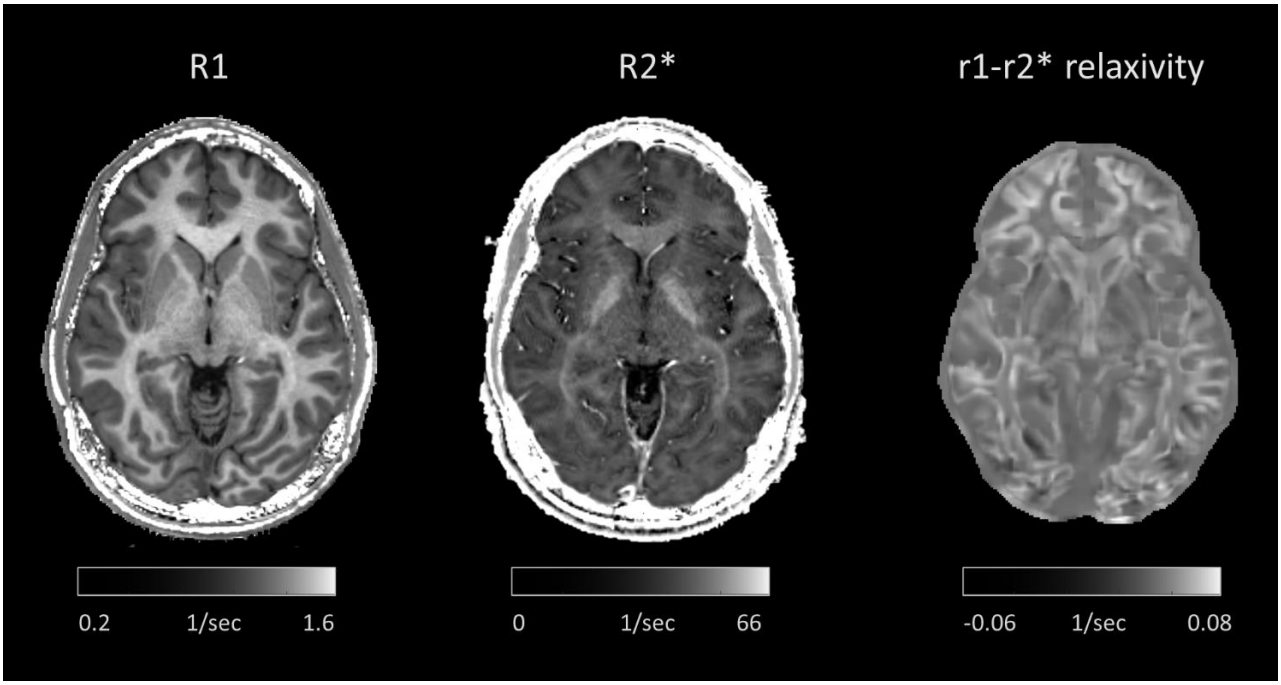


***Sup. Figure 10: Voxel-wise comparison of the r1-r2* relaxivity map to R1 and R2* maps in the in vivo brain.*** *The maps of R1 (left) and R2* (middle) are compared to the local r1-r2* relaxivity map (right) on a representative young healthy subject. The voxel-wise map of the local r1-r2* relaxivity in the brain was generated based on the local linear dependency of R1 on R2* using a moving-window approach (for more details see "Generating voxel-wise r1-r2* relaxivity maps" in Methods).*

# Supplementary Figure 11

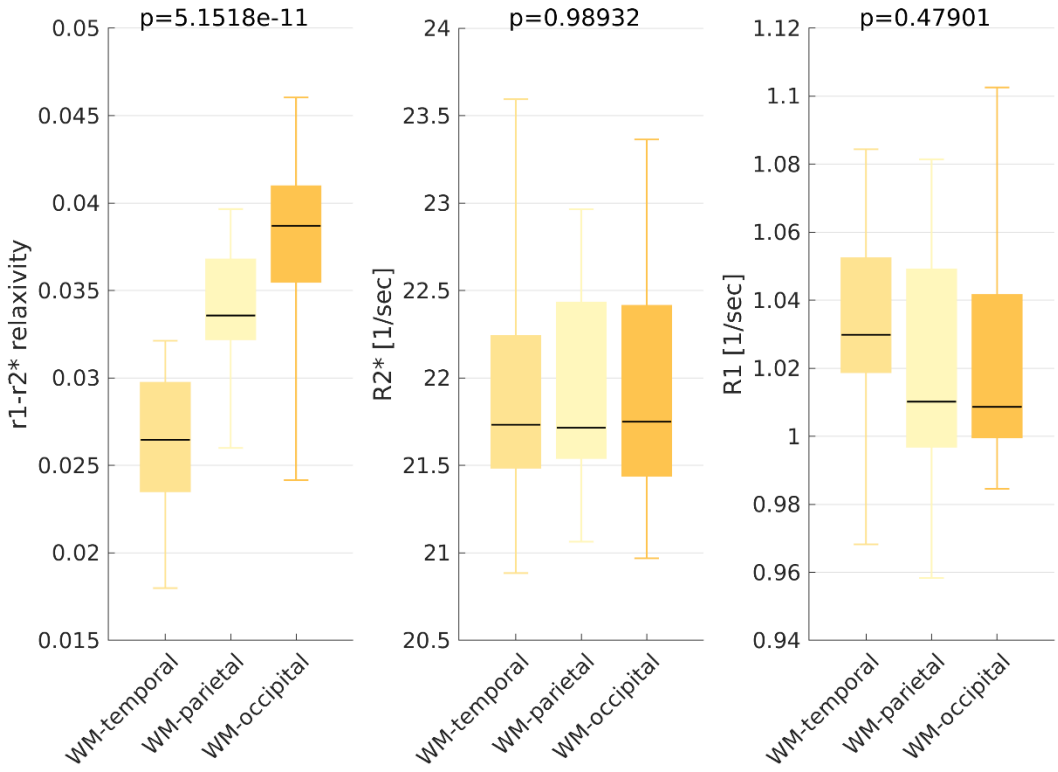


***Sup. Figure 11: The new contrast of the r1-r2* relaxivity in white matter.*** *From left to right, r1-r2* relaxivity, R2* and R1 for three different white-matter (WM) ROIs (temporal, parietal and occipital). We can separate these three WM ROIs with the r1-r2* relaxivity but not with either R2* or R1. Boxes represent the variation in the MRI parameters across normal subjects (age 27±2, N = 21). The 50$^{th}$ percentile (horizontal black lines) 25th and 75th percentiles (box edges) and extreme data points (whiskers) are shown for each box. p-values are for the ANOVA test.*

## Supplementary Figure 12

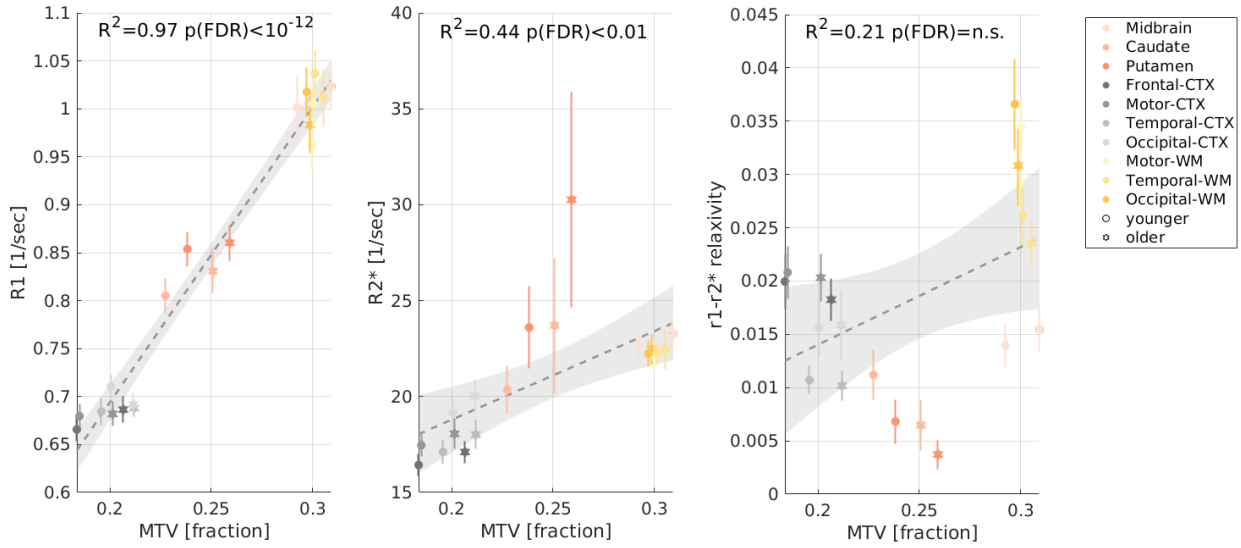


***Sup. Figure 12: The correlations of MRI parameters with MTV.*** *The qMRI measurement of the macromolecular tissue volume (MTV) vs. R1, R2* and the r1-r2* relaxivity measured in vivo across younger (aged 23-63 years, N =26) and older (aged 65-77 years, N=13) subjects (different marker shapes) in 10 brain regions (different colors). Unlike R1 and R2*, the r1-r2* relaxivity is not correlated with MTV.*

## Supplementary Figure 13

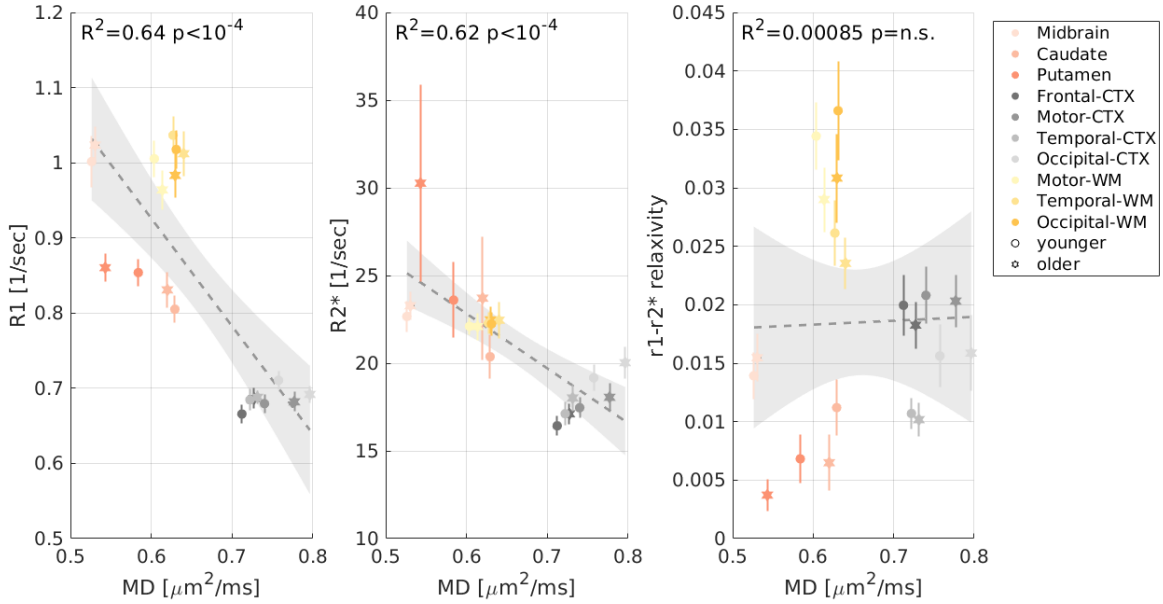


***Sup. Figure 13: The correlations of MRI parameters with MD.*** *The qMRI measurement of the mean diffusivity (MD) measured in vivo across younger (aged 23-63 years, N =25) and older (aged 65-77 years, N=12) subjects vs. R1, R2* and the r1-r2* relaxivity measured in vivo across younger (aged 23-63 years, N =26) and older (aged 65-77 years, N=13) subjects (different marker shapes) in 10 brain regions (different colors). Unlike R1 and R2*, the r1-r2* relaxivity is not correlated with MD.*

# Supplementary Figure 14

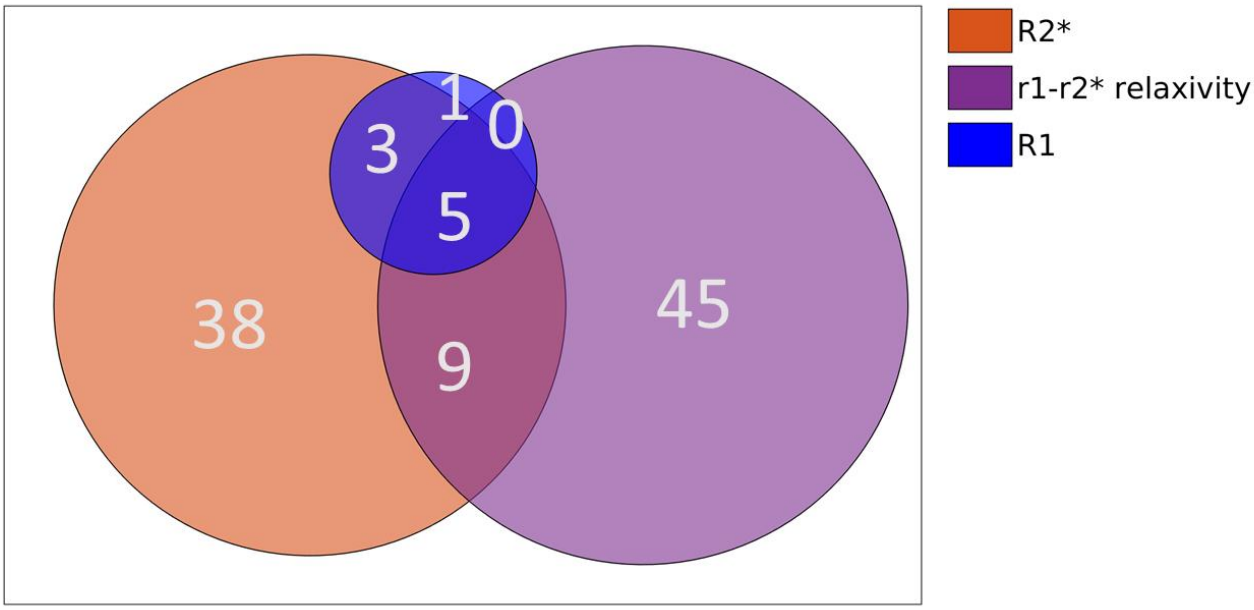


***Sup. Figure 14: The number of significantly enriched pathways associated with each qMRI parameter.*** *The Venn diagram shows the number of significantly enriched pathways (p(FWER)<0.01) for each qMRI parameter (R2*, R1 and the r1-r2* relaxivity). Almost half of the significantly enriched pathways are exclusive for the r1-r2* relaxivity. See also supplementary table 1.*

# Supplementary Table 1:

| pathway | R1 NES | R1 pval | R2* NES | R2* pval | r1-r2* relaxivity NES | r1-r2* relaxivity pval |
|---|---|---|---|---|---|---|
| GO ALPHA BETA T CELL ACTIVATION | 1.15 | 1 | 2.43 | 0.001 | -1.12 | 1 |
| GO ALPHA BETA T CELL DIFFERENTIATION | 1.26 | 1 | 2.44 | 0.001 | -1.04 | 1 |
| GO ANTIGEN BINDING | 0.79 | 1 | 2.23 | 0.024 | -2.86 | 0 |
| GO B CELL MEDIATED IMMUNITY | -0.64 | 1 | 1.48 | 1 | -2.56 | 0 |
| GO B CELL RECEPTOR SIGNALING PATHWAY | 0.97 | 1 | 2.21 | 0.038 | -2.50 | 0 |
| GO CD4 POSITIVE ALPHA BETA T CELL ACTIVATION | 0.99 | 1 | 2.32 | 0.005 | -1.22 | 1 |
| GO CD4 POSITIVE ALPHA BETA T CELL DIFFERENTIATION | 1.22 | 1 | 2.38 | 0.003 | -1.20 | 1 |
| GO COMPLEMENT ACTIVATION | -0.86 | 1 | 1.33 | 1 | -2.90 | 0 |
| GO CONDENSED NUCLEAR CHROMOSOME CENTROMERIC REGION | -2.33 | 0.004 | -1.64 | 1 | -1.46 | 1 |
| GO COTRANSLATIONAL PROTEIN TARGETING TO MEMBRANE | 2.55 | 0.001 | 2.44 | 0.001 | 3.18 | 0 |
| GO CYTOSOLIC LARGE RIBOSOMAL SUBUNIT | 2.31 | 0.019 | 2.27 | 0.012 | 2.95 | 0 |
| GO CYTOSOLIC RIBOSOME | 2.21 | 0.112 | 2.57 | 0 | 3.06 | 0 |
| GO CYTOSOLIC SMALL RIBOSOMAL SUBUNIT | 1.73 | 1 | 2.38 | 0.003 | 2.44 | 0.003 |
| GO DEFENSE RESPONSE TO BACTERIUM | 0.78 | 1 | 1.76 | 1 | -2.27 | 0.006 |
| GO ESTABLISHMENT OF PROTEIN LOCALIZATION TO ENDOPLASMIC RETICULUM | 2.11 | 0.317 | 2.08 | 0.272 | 3.14 | 0 |
| GO FC RECEPTOR MEDIATED STIMULATORY SIGNALING PATHWAY | 1.29 | 1 | 1.65 | 1 | -2.29 | 0.004 |
| GO HUMORAL IMMUNE RESPONSE | 0.72 | 1 | 1.72 | 1 | -2.43 | 0 |
| GO HUMORAL IMMUNE RESPONSE MEDIATED BY CIRCULATING IMMUNOGLOBULIN | -0.52 | 1 | 1.61 | 1 | -3.10 | 0 |
| GO IMMUNE RECEPTOR ACTIVITY | 1.27 | 1 | 2.46 | 0 | 0.71 | 1 |
| GO IMMUNOGLOBULIN COMPLEX | -1.14 | 1 | 2.52 | 0 | -3.62 | 0 |
| GO IMMUNOGLOBULIN COMPLEX CIRCULATING | 0.94 | 1 | 2.32 | 0.005 | -3.14 | 0 |
| GO IMMUNOGLOBULIN RECEPTOR BINDING | 0.72 | 1 | 2.30 | 0.008 | -3.06 | 0 |
| GO KINETOCHORE | -2.00 | 0.594 | -2.40 | 0.002 | -0.94 | 1 |
| GO LARGE RIBOSOMAL SUBUNIT | 0.91 | 1 | 1.13 | 1 | 2.59 | 0 |
| GO METAPHASE ANAPHASE TRANSITION OF CELL CYCLE | -2.10 | 0.219 | -2.55 | 0 | -0.81 | 1 |
| GO MITOCHONDRIAL GENE EXPRESSION | -2.18 | 0.067 | -2.45 | 0 | 1.57 | 1 |
| GO MITOCHONDRIAL TRANSLATION | -2.08 | 0.266 | -2.44 | 0 | 1.82 | 0.998 |
| GO MITOCHONDRIAL TRANSLATIONAL TERMINATION | -2.05 | 0.388 | -2.58 | 0 | 1.73 | 1 |
| GO MITOTIC METAPHASE PLATE CONGRESSION | -1.80 | 1 | -2.41 | 0.002 | 1.05 | 1 |
| GO MITOTIC NUCLEAR DIVISION | -2.12 | 0.156 | -2.32 | 0.009 | -0.85 | 1 |
| GO MITOTIC SISTER CHROMATID SEGREGATION | -2.19 | 0.059 | -2.36 | 0.005 | 0.85 | 1 |
| GO NEGATIVE REGULATION OF CHROMOSOME SEGREGATION | -2.01 | 0.548 | -2.35 | 0.007 | -0.84 | 1 |
| GO NEGATIVE REGULATION OF METAPHASE ANAPHASE TRANSITION OF CELL CYCLE | -2.13 | 0.155 | -2.46 | 0 | -0.98 | 1 |
| GO NUCLEAR TRANSCRIBED MRNA CATABOLIC PROCESS NONSENSE MEDIATED DECAY | 2.25 | 0.059 | 2.36 | 0.003 | 2.49 | 0.001 |
| GO PHAGOCYTOSIS RECOGNITION | -0.69 | 1 | 1.60 | 1 | -2.89 | 0 |
| GO POSITIVE REGULATION OF B CELL ACTIVATION | -0.51 | 1 | 1.50 | 1 | -2.35 | 0.001 |
| GO POSITIVE REGULATION OF LEUKOCYTE CELL CELL ADHESION | 0.91 | 1 | 2.32 | 0.003 | -1.06 | 1 |
| GO POSITIVE T CELL SELECTION | 1.14 | 1 | 2.45 | 0.001 | 0.92 | 1 |
| GO PROTEIN LOCALIZATION TO ENDOPLASMIC RETICULUM | 2.16 | 0.195 | 1.98 | 0.711 | 2.93 | 0 |
| GO PROTEIN TARGETING TO MEMBRANE | 1.83 | 0.998 | 1.71 | 1 | 2.50 | 0.001 |
| GO REGULATION OF B CELL ACTIVATION | 0.68 | 1 | 1.84 | 0.995 | -2.29 | 0.004 |
| GO REGULATION OF CHROMOSOME SEPARATION | -2.06 | 0.34 | -2.49 | 0 | -0.84 | 1 |
| GO REGULATION OF HUMORAL IMMUNE RESPONSE | -1.03 | 1 | 1.24 | 1 | -2.59 | 0 |
| GO REGULATION OF SISTER CHROMATID SEGREGATION | -1.94 | 0.878 | -2.43 | 0 | -0.80 | 1 |
| GO RIBOSOMAL SUBUNIT | 0.93 | 1 | 1.41 | 1 | 2.79 | 0 |
| GO RIBOSOME | -0.80 | 1 | 1.25 | 1 | 2.64 | 0 |
| GO SMALL RIBOSOMAL SUBUNIT | -0.91 | 1 | 1.43 | 1 | 2.40 | 0.007 |
| GO STRUCTURAL CONSTITUENT OF RIBOSOME | 1.07 | 1 | 1.49 | 1 | 2.91 | 0 |
| GO TRANSLATIONAL INITIATION | 1.93 | 0.951 | 2.05 | 0.401 | 2.47 | 0.001 |
| GO TRANSLATIONAL TERMINATION | -1.98 | 0.68 | -2.51 | 0 | 1.83 | 0.997 |
| GO T CELL ACTIVATION INVOLVED IN IMMUNE RESPONSE | 1.27 | 1 | 2.46 | 0 | -1.22 | 1 |
| GO T CELL RECEPTOR COMPLEX | -0.60 | 1 | 2.35 | 0.003 | 0.65 | 1 |
| GO T CELL SELECTION | 1.21 | 1 | 2.58 | 0 | 1.06 | 1 |
| GO UNFOLDED PROTEIN BINDING | -1.08 | 1 | -2.34 | 0.007 | 1.36 | 1 |
| KEGG LEISHMANIA INFECTION | 1.70 | 1 | 2.44 | 0.001 | 1.01 | 1 |
| KEGG RIBOSOME | 2.53 | 0.001 | 2.68 | 0 | 3.10 | 0 |
| PID IL12 2PATHWAY | 0.99 | 1 | 2.35 | 0.003 | -1.04 | 1 |
| PID PLK1 PATHWAY | -2.61 | 0 | -2.38 | 0.003 | -1.27 | 1 |
| PID TCR PATHWAY | 0.81 | 1 | 2.37 | 0.003 | -0.94 | 1 |
| REACTOME ACTIVATION OF THE MRNA UPON BINDING OF THE CAP BINDING COMPLEX AND EIFS AND SUBSEQUENT BINDING TO | 2.26 | 0.056 | 2.23 | 0.022 | 2.75 | 0 |
| REACTOME ANTIGEN ACTIVATES B CELL RECEPTOR BCR LEADING TO GENERATION OF SECOND MESSENGERS | 0.80 | 1 | 1.91 | 0.947 | -3.01 | 0 |
| REACTOME BINDING AND UPTAKE OF LIGANDS BY SCAVENGER RECEPTORS | -0.75 | 1 | 1.58 | 1 | -2.74 | 0 |
| REACTOME CD22 MEDIATED BCR REGULATION | -1.40 | 1 | 2.18 | 0.073 | -3.25 | 0 |
| REACTOME CELL CYCLE CHECKPOINTS | -2.17 | 0.073 | -2.54 | 0 | -1.00 | 1 |
| REACTOME COMPLEMENT CASCADE | -1.04 | 1 | 0.94 | 1 | -2.78 | 0 |
| REACTOME CREATION OF C4 AND C2 ACTIVATORS | -0.99 | 1 | 1.52 | 1 | -3.07 | 0 |
| REACTOME CYCLIN A B1 B2 ASSOCIATED EVENTS DURING G2 M TRANSITION | -2.34 | 0.004 | -2.45 | 0 | -0.97 | 1 |
| REACTOME EUKARYOTIC TRANSLATION ELONGATION | 2.67 | 0 | 2.80 | 0 | 3.19 | 0 |
| REACTOME EUKARYOTIC TRANSLATION INITIATION | 2.56 | 0.001 | 2.60 | 0 | 3.23 | 0 |
| REACTOME FCERI MEDIATED CA 2 MOBILIZATION | 1.18 | 1 | 2.11 | 0.172 | -2.91 | 0 |
| REACTOME FCERI MEDIATED MAPK ACTIVATION | 0.89 | 1 | 1.78 | 1 | -2.88 | 0 |
| REACTOME FCGAMMA RECEPTOR FCGR DEPENDENT PHAGOCYTOSIS | 1.40 | 1 | 1.61 | 1 | -2.41 | 0 |
| REACTOME FCGR3A MEDIATED IL10 SYNTHESIS | 0.76 | 1 | 1.93 | 0.891 | -2.86 | 0 |
| REACTOME FCGR ACTIVATION | 0.97 | 1 | 2.01 | 0.558 | -3.27 | 0 |
| REACTOME GENERATION OF SECOND MESSENGER MOLECULES | 1.34 | 1 | 2.57 | 0 | 1.17 | 1 |
| REACTOME IMMUNOREGULATORY INTERACTIONS BETWEEN A LYMPHOID AND A NON LYMPHOID CELL | 0.52 | 1 | 2.39 | 0.003 | -2.21 | 0.02 |
| REACTOME INFLUENZA INFECTION | 1.42 | 1 | 1.79 | 1 | 2.70 | 0 |
| REACTOME INITIAL TRIGGERING OF COMPLEMENT | -0.86 | 1 | 1.42 | 1 | -3.05 | 0 |
| REACTOME INTERLEUKIN 10 SIGNALING | 0.72 | 1 | 1.92 | 0.929 | -2.45 | 0 |
| REACTOME MITOCHONDRIAL TRANSLATION | -2.06 | 0.339 | -2.48 | 0 | 1.80 | 1 |
| REACTOME MITOTIC METAPHASE AND ANAPHASE | -1.99 | 0.624 | -2.46 | 0 | 1.20 | 1 |
| REACTOME MITOTIC PROMETAPHASE | -1.89 | 0.969 | -2.34 | 0.007 | -0.83 | 1 |
| REACTOME MITOTIC SPINDLE CHECKPOINT | -2.21 | 0.042 | -2.69 | 0 | -0.71 | 1 |
| REACTOME NONSENSE MEDIATED DECAY NMD | 2.28 | 0.039 | 2.42 | 0.001 | 2.66 | 0 |
| REACTOME PARASITE INFECTION | 0.90 | 1 | 1.39 | 1 | -2.59 | 0 |
| REACTOME REGULATION OF EXPRESSION OF SLITS AND ROBOS | 1.49 | 1 | 1.83 | 0.999 | 2.52 | 0.001 |
| REACTOME RESOLUTION OF D LOOP STRUCTURES THROUGH SYNTHESIS DEPENDENT STRAND ANNEALING SDSA | -2.15 | 0.101 | -2.43 | 0 | -1.38 | 1 |
| REACTOME RESOLUTION OF SISTER CHROMATID COHESION | -2.31 | 0.005 | -2.71 | 0 | -0.72 | 1 |
| REACTOME RESPONSE OF EIF2AK4 GCN2 TO AMINO ACID DEFICIENCY | 2.21 | 0.111 | 2.55 | 0 | 2.73 | 0 |
| REACTOME ROLE OF LAT2 NTAL LAB ON CALCIUM MOBILIZATION | 1.12 | 1 | 1.94 | 0.852 | -3.13 | 0 |
| REACTOME ROLE OF PHOSPHOLIPIDS IN PHAGOCYTOSIS | 1.41 | 1 | 2.25 | 0.016 | -3.04 | 0 |
| REACTOME RRNA PROCESSING | 0.91 | 1 | 1.32 | 1 | 2.69 | 0 |
| REACTOME SCAVENGING OF HEME FROM PLASMA | 1.37 | 1 | 2.20 | 0.038 | -3.27 | 0 |
| REACTOME SELENOAMINO ACID METABOLISM | 1.87 | 0.993 | 2.31 | 0.008 | 2.95 | 0 |
| REACTOME SEPARATION OF SISTER CHROMATIDS | -2.05 | 0.363 | -2.54 | 0 | 1.10 | 1 |
| REACTOME SIGNALING BY ROBO RECEPTORS | 1.61 | 1 | 1.90 | 0.961 | 2.40 | 0.007 |
| REACTOME SRP DEPENDENT COTRANSLATIONAL PROTEIN TARGETING TO MEMBRANE | 2.30 | 0.027 | 2.24 | 0.021 | 3.14 | 0 |
| REACTOME TRANSLATION | -1.14 | 1 | -1.34 | 1 | 2.93 | 0 |
| WP CYTOPLASMIC RIBOSOMAL PROTEINS | 2.71 | 0 | 2.77 | 0 | 3.17 | 0 |
| WP MICROGLIA PATHOGEN PHAGOCYTOSIS PATHWAY | 1.79 | 0.999 | 2.61 | 0 | 1.63 | 1 |
| WP TYROBP CAUSAL NETWORK | 2.30 | 0.024 | 2.83 | 0 | 1.16 | 1 |

***Sup. Table 1: Significantly enriched pathways for R1, R2* and the r1-r2* relaxivity.*** *For each of the 101 gene sets, we show the normalized enrichments score (NES) for each of the three qMRI parameters, along with the FWER-corrected p-value. This table was used for the clustering shown in* Figure 3g.

## Supplementary Figure 15

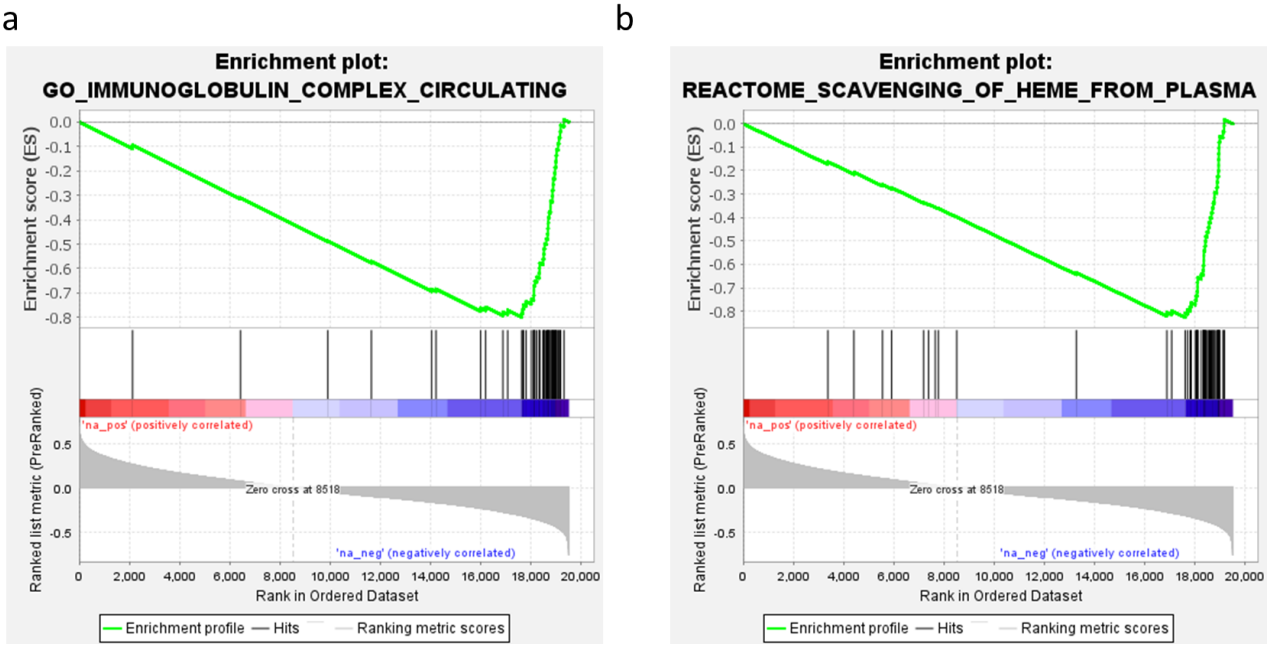


***Sup. Figure 15: Enrichment plots of the two most enriched pathways for the r1-r2* relaxivity.*** *Gene enrichment plots of the two most enriched pathways for the r1-r2* relaxivity "Immunoglobulin complex"* ***(a)*** *and "scavenging of heme from plasma"* ***(b)****. The top portion of each panel shows the running enrichment score for the gene set as the analysis goes over the ranked list of genes. The list is based on the genes' correlation with the r1-r2* relaxivity. The middle portion of each panel shows where the members of the gene set appear in the ranked list of genes. The bottom portion of each panel shows the r value of the correlation between genes and the r1-r2* relaxivity. The two gene sets preferentially fall toward the negative end of the correlation spectrum, indicating their significant association with the r1-r2* relaxivity.*

## Supplementary Figure 16

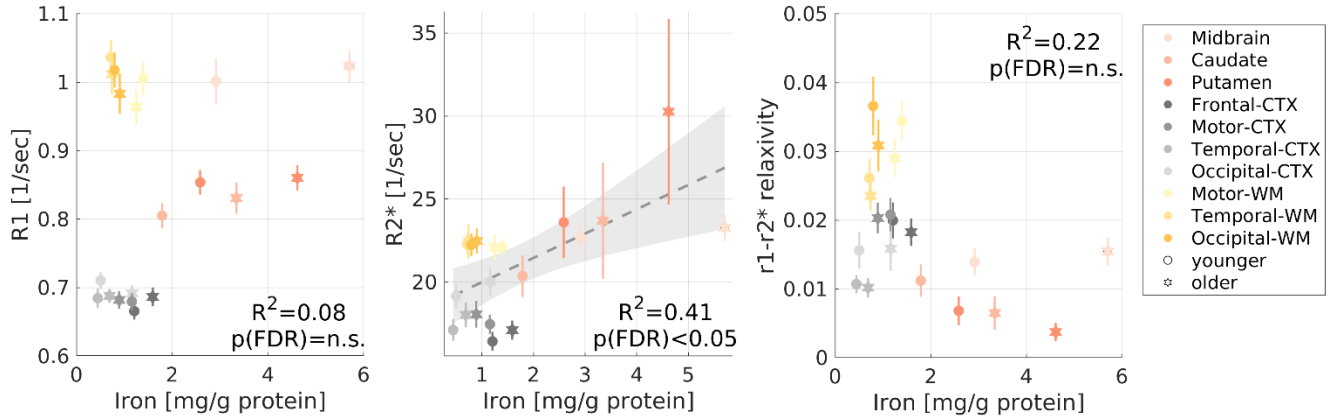


***Sup. Figure 16: The correlations of MRI parameters with iron concentration.*** *The iron concentration (postmortem, from the literature[5,7,9]) in different brain regions of younger (aged 27-64 years, N>=7) and older (aged 65-88 years, N>=8) subjects vs. R1, R2* and the r1-r2* relaxivity measured in vivo across younger (aged 23-63 years, N =26) and older (aged 65-77 years, N=13) subjects (different marker shapes) in 10 brain regions (different colors). Only R2* is significantly correlated with the iron concentration.*

## Supplementary Figure 17

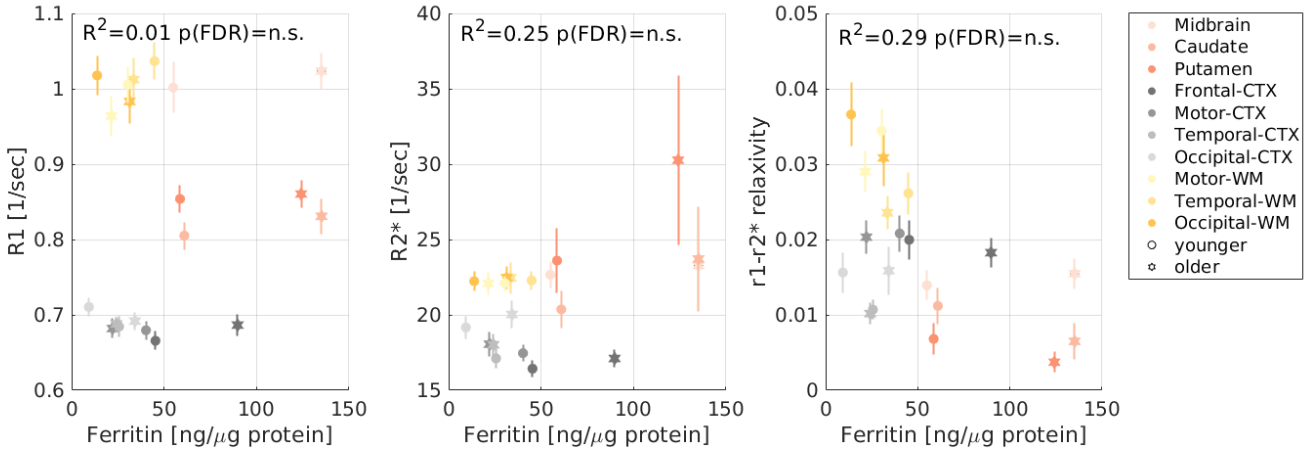


***Sup. Figure 17: The correlations of MRI parameters with ferritin concentration.*** *The ferritin concentration (postmortem, from the literature[5,7,9]) in different brain regions of younger (aged 27-64 years, N>=7) and older (aged 65-88 years, N>=8) subjects vs. R1, R2* and the r1-r2* relaxivity measured in vivo across younger (aged 23-63 years, N =26) and older (aged 65-77 years, N=13) subjects (different marker shapes) in 10 brain regions (different colors). None of the MRI parameters tested is significantly correlated with the ferritin concentration.*

## Supplementary Figure 18

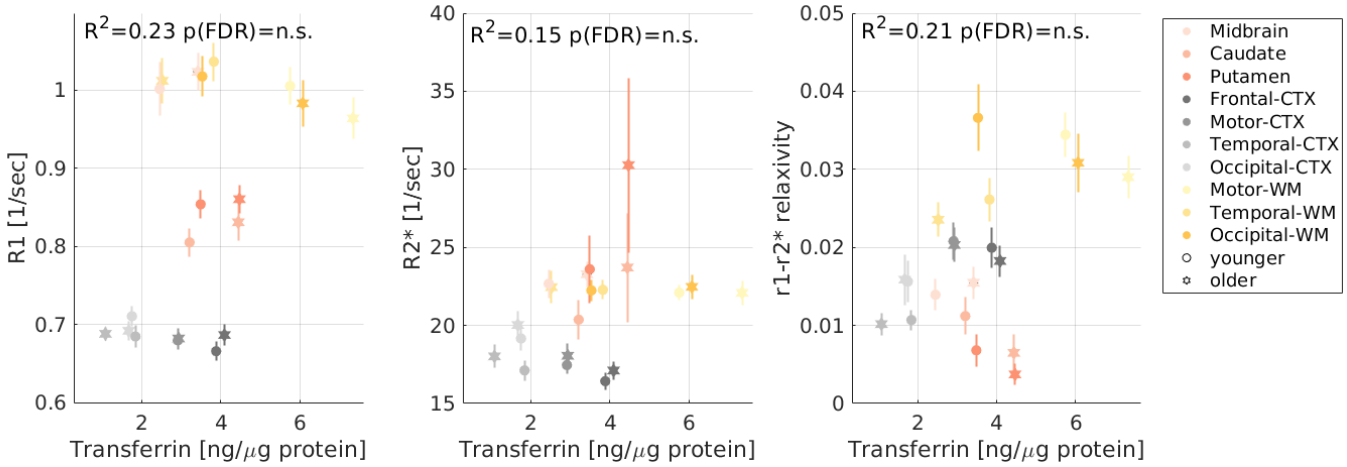


***Sup. Figure 18: The correlations of MRI parameters with transferrin concentration.*** *The transferrin concentration (postmortem, from the literature[5,7,9]) in different brain regions of younger (aged 27-64 years, N>=7) and older (aged 65-88 years, N>=8) subjects vs. R1, R2* and the r1-r2* relaxivity measured in vivo across younger (aged 23-63 years, N =26) and older (aged 65-77 years, N=13) subjects (different marker shapes) in 10 brain regions (different colors). None of the MRI parameters tested is significantly correlated with the transferrin concentration.*

# Supplementary Section 4: Exploring the biophysical sources of the r1-r2* relaxivity.

## Supplementary Section 4.1: The theoretical basis for the r1-r2* relaxivity of brain tissue.

The theoretical basis for the r1-r2* relaxivity presented in the results describes the relaxivity effect on the MR relaxation rates when only a single iron compound is present (for more details, see "*In vivo* iron relaxivity model" in Methods). While this is the case in our phantom experiments (**Figure 1**), brain tissue contains multiple iron compounds and includes myelin. When ferritin, transferrin and myelin are present, and under the assumption that water can freely diffuse, the MR relaxation rates can be expressed as[79,80]:

$$S1) \qquad R_1 = r_{(1,Ft)}[Ft] + r_{(1,Tf)}[Tf] + r_{(1,M)}[M]$$

$$S2) \qquad R_2^* = r_{(2,Ft)}[Ft] + r_{(2,Tf)}[Tf] + r_{(2,M)}[M]$$

Where $[Ft]$, $[Tf]$ and $[M]$ are the ferritin, transferrin and myelin concentrations respectively. $r_{(1,Ft)}$, $r_{(1,Tf)}$ and $r_{(1,M)}$ are the R1-relaxivities of ferritin, transferrin and myelin respectively. $r_{(2,Ft)}$, $r_{(2,Tf)}$ and $r_{(2,M)}$ are the R2*-relaxivities of ferritin, transferrin and myelin respectively.

The r1-r2* relaxivity measurement is defined as the linear dependency of R1 on R2* within an ROI in the brain (or across *in vitro* samples). This is equivalent to the total change in R1 relative to the total change in R2* ($\frac{\Delta R_1}{\Delta R_2^*}$):

$$\text{S3)} \qquad \frac{\Delta R_1}{\Delta R_2^*} = \frac{r_{(1,Ft)}[\Delta Ft] + r_{(1,Tf)}[\Delta Tf] + r_{(1,M)}[\Delta M]}{r_{(2,Ft)}[\Delta Ft] + r_{(2,Tf)}[\Delta Tf] + r_{(2,M)}[\Delta M]}$$

Where $[\Delta Ft]$, $[\Delta Tf]$, and $[\Delta M]$ are the changes in the ferritin, transferrin and myelin concentrations within an ROI (or across *in vitro* samples), respectively.

Defining $[\Delta Tf] = Tf_1 - Tf_0$ and $[\Delta Ft] = Ft_1 - Ft_0$, we will require that the transferrin-ferritin fraction ($f$) remains fixed within the ROI (or *in vitro* samples) over which the r1-r2* relaxivity is calculated:

$$f = \frac{Tf_1}{Tf_1 + Ft_1} = \frac{Tf_0}{Tf_0 + Ft_0}$$

Under this condition:

$$\text{S4)} \qquad f = \frac{[\Delta Tf]}{[\Delta Ft] + [\Delta Tf]} = \frac{[Tf]}{[Ft] + [Tf]}$$

And therefore eq. S3 can be expressed as:

$$\text{S5)} \qquad \frac{\Delta R_1}{\Delta R_2^*} = \frac{(f * r_{(1,Tf)} + (1-f) r_{(1,Ft)})[\Delta iron] + r_{(1,M)}[\Delta M]}{(f * r_{(2,Tf)} + (1-f) r_{(2,Ft)})[\Delta iron] + r_{(2,M)}[\Delta M]}$$

Where $[\Delta Ft] + [\Delta Tf] = [\Delta iron]$.

## Supplementary Section 4.2: The r1-r2* relaxivity of ferritin and transferrin mixtures *in vitro*.

First, we tested the theoretical formulation presented in eq. S*1*-S5 in an artificial environment of multiple iron compounds. For this aim, we constructed phantom experiments containing both ferritin and transferrin in a liposomal environment. We tested four different transferrin-ferritin fractions ($f = \frac{[Tf]}{[Ft]+[Tf]}$). For each fraction, we prepared samples with varying ferritin and transferrin concentrations, while keeping the fixed fraction between them (eq. S4, **Sup. Figure 19**). This allowed us to fit the linear relationship between R1 and R2* (the r1-r2* relaxivity) for each transferrin-ferritin fraction (**Sup. Figure 20**). In these experiments, the liposomal fraction, which mimics the effect of myelin, was fixed at 17.5%. Therefore, in this case $[\Delta M] = 0$ and eq. S5 reduces to:

$$\text{S6)} \qquad \frac{\Delta R_1}{\Delta R_2^*} = \frac{(f * r_{(1,Tf)} + (1-f) r_{(1,Ft)})[\Delta iron]}{(f * r_{(2,Tf)} + (1-f) r_{(2,Ft)})[\Delta iron]} = \frac{(f * r_{(1,Tf)} + (1-f) r_{(1,Ft)})}{(f * r_{(2,Tf)} + (1-f) r_{(2,Ft)})}$$

Using the ferritin and transferrin relaxivities ($r_{(1/2,Tf/Ft)}$) measured for each liposomal iron compound individually (Figure 1a-c), we could test the prediction of this model. Notably, the theoretical r1-r2* relaxivities calculated with eq. S6 were in agreement with the experimental r1-r2* relaxivities (**Sup. Figure 21**), validating the presented biophysical framework *in vitro*. Moreover, the differences in the r1-r2* relaxivities measured for different transferrin-ferritin fractions were above the detection limit of this MRI measurement as estimated in a scan-rescan experiment (MAE=3.9*10$^{-4}$, **Sup. Figure 8**). This implies that under the condition of fixed myelin concentration within an ROI, the r1-r2* relaxivity is independent of the changes in myelin and iron concentration ($[\Delta iron]$, $[\Delta M]$) and is only sensitive to the transferrin-ferritin fraction ($f$).

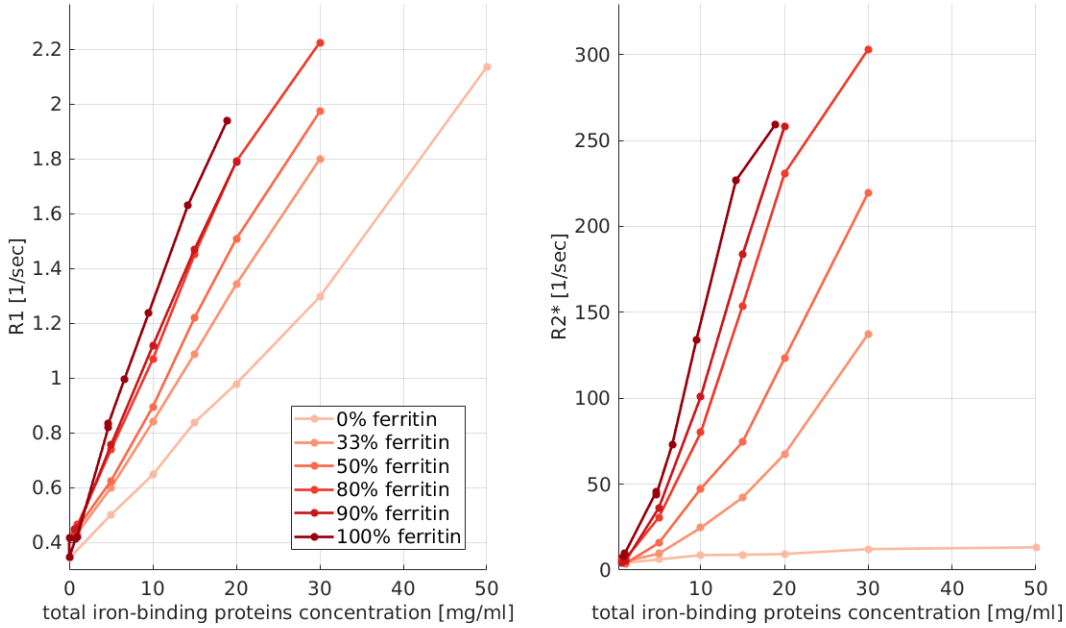


***Sup. Figure 19: The dependency of R1 (left) and R2* (right) on the total iron-binding proteins concentration for four transferrin-ferritin mixtures.*** *Each mixture has a different transferrin-ferritin fraction (different colors, legend shows the percentage of ferritin in the mixture). Data points are different transferrin-ferritin samples, line connect between samples with the same transferrin-ferritin fraction and varying total iron-binding protein concentrations.*

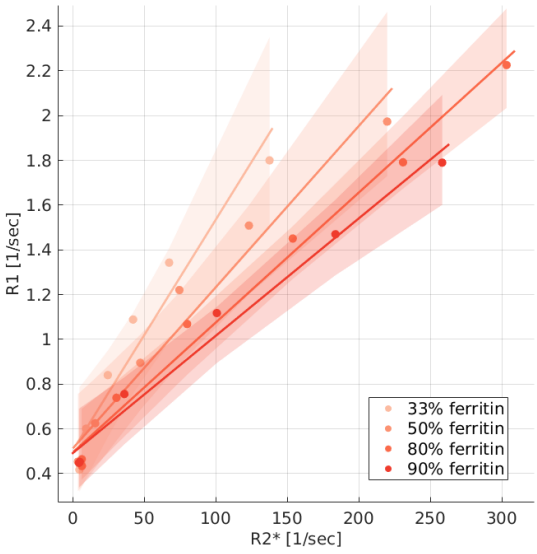


***Sup. Figure 20: The dependency of R1 on R2* for four transferrin-ferritin mixtures.*** *Each mixture has a different transferrin-ferritin fraction (different colors, legend shows the percentage of ferritin in the mixture). Data points represent samples with varying total iron-binding proteins concentrations. The linear relationships of R1 and R2* are marked by lines. The slopes of these lines are the r1-r2* relaxivities. Shaded areas represent the 95% confidence bounds.*

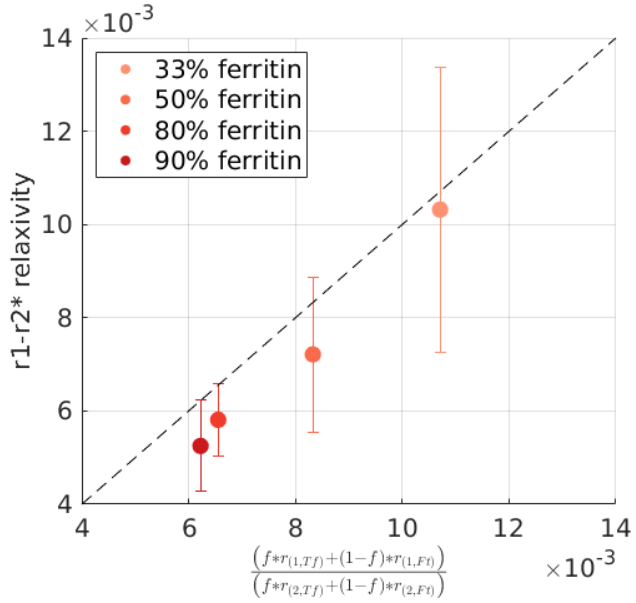


***Sup. Figure 21: The theoretical r1-r2* relaxivities calculated with eq.*** S6 ***are in agreement with the experimental r1-r2* relaxivities.*** *The y-axis shows the r1-r2* relaxivity calculated for four transferrin-ferritin mixtures with different transferrin-ferritin fractions (different colors, Sup. Figure 20). Errorbars show the 95% confidence bounds. The x-axis shows the prediction for the r1-r2* relaxivity based on eq.* S6*. The ferritin and transferrin relaxivities in the equation were plugged in based on our experimental results for liposomal ferritin and liposomal transferrin samples (*Figure 1a-c*). f represents the transferrin-ferritin fractions and varies between data points. Dashed line is the identity line.*

## Supplementary Section 4.3: Numerical simulations of the r1-r2* relaxivity.

The phantom experiments of ferritin and transferrin mixtures allowed us to establish a theoretical framework for the r1-r2* relaxivity in an *in vitro* environment where only the iron concentration changes, and the liposomal fraction mimicking the myelin is fixed ($[\Delta M] = 0$). In the brain, we estimate the r1-r2* relaxivity across all voxels of an anatomically-defined ROI. Within brain tissue ROIs, both the iron and the myelin concentration may vary[44].

Importantly, rearranging eq. S5 we find that the strength of the myelin effect on the r1-r2* relaxivity depends on how variable is the myelin content within an ROI relative to how variable is the iron content ($\frac{[\Delta M]}{[\Delta iron]}$):

$$\frac{\Delta R_1}{\Delta R_2^*} = \frac{\left(f * r_{(1,Tf)} + (1-f) r_{(1,Ft)}\right) + r_{(1,M)} \frac{[\Delta M]}{[\Delta iron]}}{\left(f * r_{(2,Tf)} + (1-f) r_{(2,Ft)}\right) + r_{(2,M)} \frac{[\Delta M]}{[\Delta iron]}}$$

In order to evaluate how the r1-r2* relaxivity is modulated by the transferrin-ferritin fraction ($f$) and by the myelin and iron variability within an ROI in the brain, we performed a set of numerical simulations.

In these analyses we aim to simulate realistic concentrations of ferritin, transferrin and myelin, in order to achieve brain-like R1 and R2* values. Next, we follow our analysis pipeline; binning of the R2* and R1 measurements, excluding bins with small number of voxels, and assessing the r1-r2* relaxivity across the binned values. By varying the simulated content of the myelin and iron compounds we test to what extent each biological source contributes to the measurement of the r1-r2* relaxivity. First, we will examine our hypothesis that changes in the transferrin-ferritin fraction, but not in their concentrations, affect the r1-r2* relaxivity. We will then evaluate how the r1-r2* relaxivity is modulated by myelin. We will show that non-physiological conditions are required in order for the myelin by itself to fully explain the r1-r2* relaxivity changes measured in the brain.

Each numerical simulation was designed to mimic an ROI in the brain containing 1M voxels, with a fixed transferrin-ferritin fraction ($f$) across all voxels and varying myelin, transferrin and ferritin concentrations (**Sup. Table 2**). We synthetically generated R1 and R2* values for each voxel based on eq. S1-S2. The relaxivities of ferritin and transferrin ($r_{(1/2,Ft)}$, $r_{(1/2,Tf)}$) were taken from the results of our phantom experiments (**Figure 1**). In order to generate simulations that are as realistic as possible, the rest of the parameters were adapted from the human brain. The mean ferritin and transferrin concentrations (across all voxels of the ROI) were estimated based on post-mortem findings[5,7,9]. The myelin

characteristics were simulated based on the qMRI measurement of the macromolecular tissue volume (MTV)[45], defined as 1-water fraction, which was shown to approximate the myelin content [46–50]. The myelin relaxivity ($r_{(1/2,M)}$) is defined as the dependency of relaxation rates on the myelin concentration[68]. We estimated the myelin relaxivity as the linear dependency of R1 and R2* on MTV, averaged across 16 ROIs in the brains of 21 young subjects. In order to assess the changes in myelin content within brain ROIs ($[\Delta M]$), we calculated the range of MTV values within white-matter (WM) or gray-matter (GM) regions averaged across 8 ROIs in the brains of 21 young subjects (**Sup. Figure 22**). Finally, the changes in ferritin and transferrin concentrations within brain ROIs ($[\Delta iron]$) were determined based on the range of R2* values within 16 WM and GM regions in the brains of 21 young subjects. We assumed that the changes in R2* not explained by MTV are related to changes in iron concentration (**Sup. Figure 23**):

$$\Delta(iron)R_2^* = \Delta(total)R_2^* - r_{(2,M)}[\Delta M]$$

We found that the total change in R2* within ROIs in the human brain is on average $\Delta(total)R_2^*$=9.0 1/sec, from which about 61% ($\Delta(iron)R_2^*$=5.6 1/sec) could be related to changes in iron concentration. Therefore, the simulated variably in the ferritin and transferrin concentrations were set to satisfy this requirement.

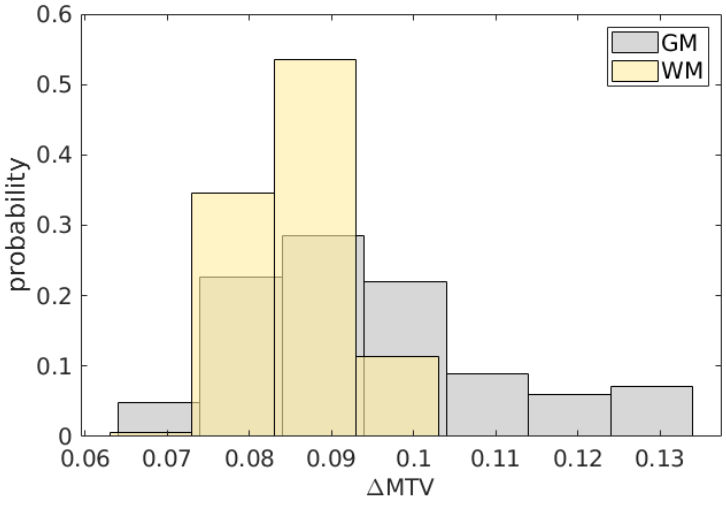


***Sup. Figure 22: Change in MTV values ($[\Delta MTV]$) within white-matter (WM) or gray-matter (GM) regions.*** *ΔMTV values for gray matter (GM) and white matter (WM) are presented across 16 ROIs in the brains of 21 young subjects. For each ROI, we extracted the MTV values from all voxels and pooled them into 36 bins spaced equally between 0.05 and 0.40 [fraction]. We removed any bins in which the number of voxels was smaller than 4% of the total voxel count in the ROI. This was done so that the calculation will not be heavily affected by outlier voxels with extreme values. The median MTV of each bin was computed, and the difference between the highest and lowest binned MTV values was set as ΔMTV ([fraction]) in the ROI.*

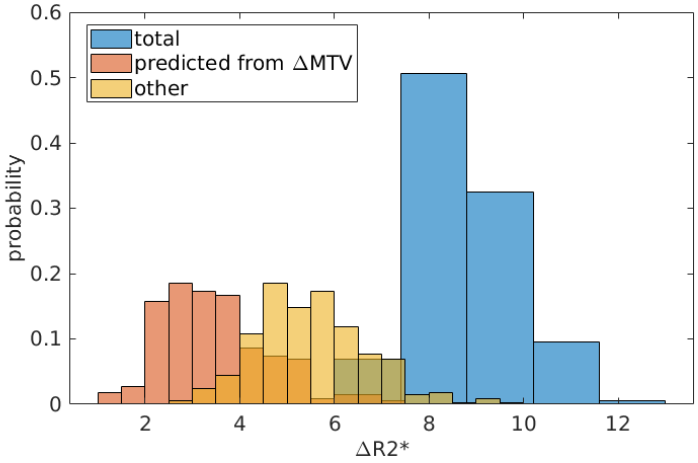


***Sup. Figure 23: Myelin- and iron- related changes in R2* within brain regions. Total change in R2* values*** *($[\Delta R2*]$)* ***within brain regions (blue histogram)*** *is presented across 16 ROIs in the brains of 21 young subjects. For each ROI, we extracted the R2* values from all voxels and pooled them into 36 bins spaced equally between 0 and 50. We removed any bins in which the number of voxels was smaller than 4% of the total voxel count in the ROI. This was done so that the calculation will not be heavily affected by outlier voxels with extreme values. The median R2* of each bin was computed, and the difference between the highest and lowest binned R2* values was set as ΔR2* in the ROI (in [1/sec]).* ***R2* changes related to myelin (orange histogram)*** *were estimated based on MTV; the change in R2* predicted from the change in MTV (ΔMTV) within each ROI was calculated as the linear dependency of R2* on MTV in the ROI multiplied by ΔMTV in the ROI ($r_{(2,M)}[\Delta M]$).* ***R2* changes related to iron (yellow histogram)*** *were estimated as the change in R2* not explained by the change in MTV.*

| *Parameter* | *Value* | *Estimation method* |
|---|---|---|
| *Transferrin-ferritin fraction ($f$)* | 0.1 or 0.2 | Based on literature values[5,7,9]. |
| *R1-ferritin relaxivity ($r_{(1,Ft)}$)* | 0.067 [(sec$^{-1}$)/(mg/wet ml)] | *In vitro* linear dependency of R1 on ferritin concentration |
| *R2*-ferritin relaxivity ($r_{(2,Ft)}$)* | 11.2 [(sec$^{-1}$)/(mg/wet ml)] | *In vitro* linear dependency of R2* on ferritin concentration |
| *R1-transferrin relaxivity ($r_{(1,Tf)}$)* | 0.026 [(sec$^{-1}$)/(mg/wet ml)] | *In vitro* linear dependency of R1 on transferrin concentration |
| *R2*-transferrin relaxivity ($r_{(2,Tf)}$)* | 0.13 [(sec$^{-1}$)/(mg/wet ml)] | *In vitro* linear dependency of R2* on transferrin concentration |
| *Transferrin concentration ($[Tf]$)* | 0.025±0.025 [mg/wet ml] | Median is based on literature values[5,7,9]. Range across voxels was set so that the total change in R2* will mimic the physiological change of 6-12 [1/sec] (Sup. Figure 23) |
| *Ferritin concentration ($[Ft]$)* | $\left(\frac{1}{f}-1\right)[Tf]$ | Set to satisfy the requirement for fixed transferrin-ferritin fraction ($f$) across all voxels. |
| *Myelin concentration in WM ($[M]_{WM}$)* | 0.29±0.047 [fraction] | Brain *in vivo* MTV values |
| *Myelin concentration in GM ($[M]_{GM}$)* | 0.19±0.043 [fraction] | Brain *in vivo* MTV values |
| *R2*-myelin relaxivity ($r_{(2,M)}$)* | 38.8 [(sec$^{-1}$)/fraction] | Brain *in vivo* linear dependency of R2* on MTV |
| *R1-myelin relaxivity ($r_{(1,M)}$)* | 2.6 [(sec$^{-1}$)/fraction] | Brain *in vivo* linear dependency of R1 on MTV |

***Sup. Table 2: simulation parameters.***

An example result of the numerical simulation is presented in **Sup. Figure 24A**. It is evident that both the changes in myelin concentration across voxels of the simulated ROI (represented by different colors) and the changes in ferritin and transferrin concentrations across voxels (represented by the symbols size) affect the measured r1-r2* relaxivity. In our analysis pipeline we first bin the R1 and R2* values within the ROI and next calculate r1-r2* relaxivity over the binned values. Therefore, the variability in R1 for a given R2* bin is collapsed to an average R1 value (black data points). We assume that this approach eliminates some of the variability related to myelin.

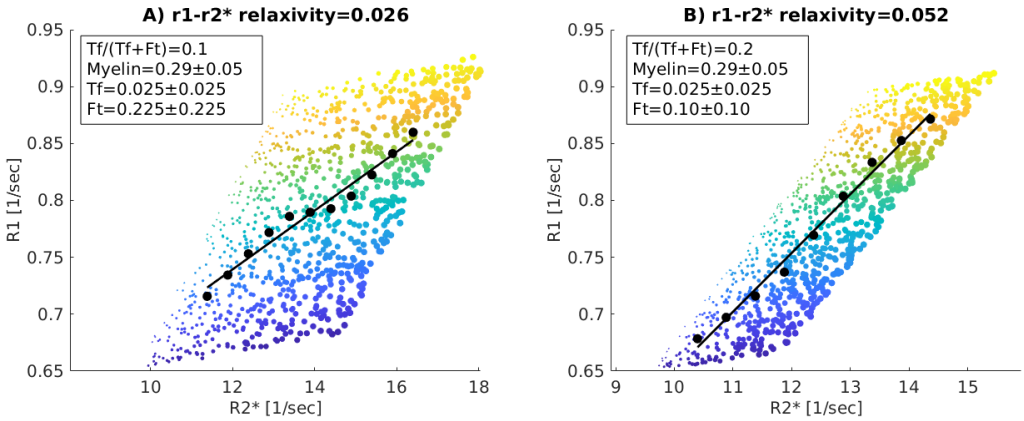


***Sup. Figure 24: The r1-r2* relaxivity in two simulated ROIs with different transferrin-ferritin fractions (Tf/(Tf+Ft))****; (A) the transferrin-ferritin fraction is 0.1; (B) the transferrin-ferritin fraction is 0.2. Each figure shows the dependency of R1 on R2* for 1,000 representative simulated voxels. The colors of the data points indicate the variability in myelin concentration across voxels, and their sizes indicate the variability in iron compounds concentration across voxels (the simulated concentrations are shown in the text box, myelin is in units of [fraction] as MTV, transferrin and ferritin are in units of [mg/ml]). As in our in vivo pipeline, R2* and R1 values were binned (black data points represent the bins' median), and a linear fit was calculated (black line). The slopes of the linear fit (shown in the title) represent the dependency of R1 on R2* (r1-r2* relaxivity) and vary with the transferrin-ferritin fraction.*

We hypothesized that the r1-r2* relaxivity is sensitive to iron compounds. Indeed, in our simulations we find that by setting different physiological transferrin-ferritin fractions and leaving the myelin parameters constant, the r1-r2* relaxivity changes considerably (**Sup. Figure 24**).

In addition, we hypothesized that the r1-r2* relaxivity is independent of the concentration of iron compounds and is only sensitive to the ratio between them. To test this, we run two numerical simulations with the same transferrin-ferritin fraction but with different transferrin and ferritin concentrations. As expected, R1 and R2* values changed with increased ferritin and transferrin concentrations but the r1-r2* relaxivity did not change (**Sup. Figure 25**). This indicates that the r1-r2* relaxivity measurement is indifferent to absolute changes in the ferritin and transferrin concentrations and is mostly sensitive to the transferrin-ferritin fraction.

In the brain, changes in the myelin content between GM and WM are known to substantially affect the measurements of R1 and R2*[4,19,25,29,39–43]. To test the potential contribution of the myelin to the r1-r2* relaxivity, we changed the myelin concentration in our simulation while keeping the rest of the parameters fixed. Setting the myelin concentration to that typical for GM or WM (as estimated *in vivo* by MTV) led to considerable changes in R1 and R2*, but did not produce any change in the r1-r2* relaxivity (**Sup. Figure 26**).

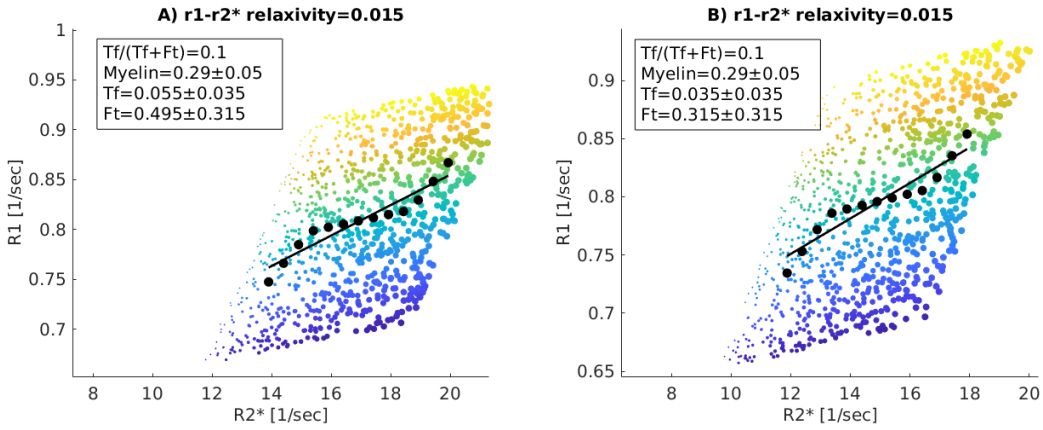


***Sup. Figure 25: The r1-r2* relaxivity in two simulated ROIs with different transferrin and ferritin concentrations and a similar transferrin-ferritin fraction (Tf/(Tf+Ft));*** *(A) a higher transferrin and ferritin concentrations and a transferrin-ferritin fraction of 0.1; (B) a lower transferrin and ferritin concentrations and a transferrin-ferritin fraction of 0.1. Each figure shows the dependency of R1 on R2* for 1,000 representative simulated voxels. The colors of the data points indicate the variability in myelin concentration across voxels, and their sizes indicate the variability in iron compounds concentration across voxels (the simulated concentrations are shown in the text box, myelin is in units of [fraction] as MTV, transferrin and ferritin are in units of [mg/ml]). As in our in vivo pipeline, R2* and R1 values were binned (black data points represent the bins' median), and a linear fit was calculated (black line). The slopes of the linear fit (shown in the title) represent the dependency of R1 on R2* (r1-r2* relaxivity) and do vary with the change in transferrin and ferritin concentrations.*

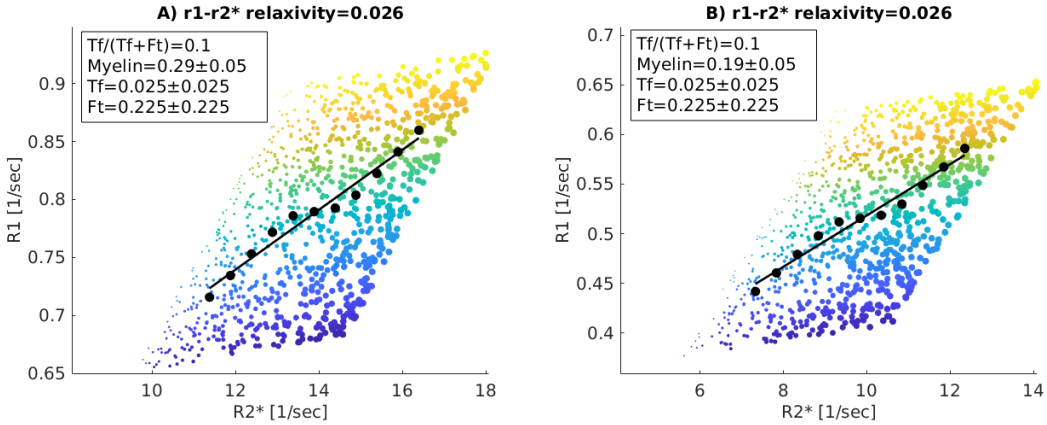


***Sup. Figure 26: The r1-r2* relaxivity in two simulated ROIs with different myelin concentrations and similar transferrin-ferritin fractions (Tf/(Tf+Ft))****; (A) a higher myelin concentration and transferrin-ferritin fraction of 0.1; (B) a lower myelin concentration and transferrin-ferritin fraction of 0.1. Each figure shows the dependency of R1 on R2* for 1,000 representative simulated voxels. The colors of the data points indicate the variability in myelin concentration across voxels, and their sizes indicate the variability in iron compounds concentration across voxels (the simulated concentrations are shown in the text box, myelin is in units of [fraction] as MTV, transferrin and ferritin are in units of [mg/ml]). As in our in vivo pipeline, R2* and R1 values were binned (black data points represent the bins' median), and a linear fit was calculated (black line). The slopes of the linear fit (shown in the title) represent the dependency of R1 on R2* (r1-r2* relaxivity) and does not vary with the change in myelin concentration.*

The theoretical formulation presented here indicates that it is not the myelin concentration, but the variability in myelin within an ROI ($[\Delta M]$), that is important for determining the r1-r2* relaxivity (eq. S5). Setting both the range and concentration of myelin to the ones typical for WM or GM (as estimated by MTV, **Sup. Figure 22**), slightly changed the r1-r2* relaxivity (0.002, **Sup. Figure 27**). Importantly, changing the transferrin-ferritin fraction between the physiological values of 0.1-0.2 led to a change of 0.026 in the r1-r2* relaxivity (**Sup. Figure 24**). Therefore, the simulated changes related to the transferrin-ferritin fraction were one order of magnitude bigger (**Sup. Figure 24**).

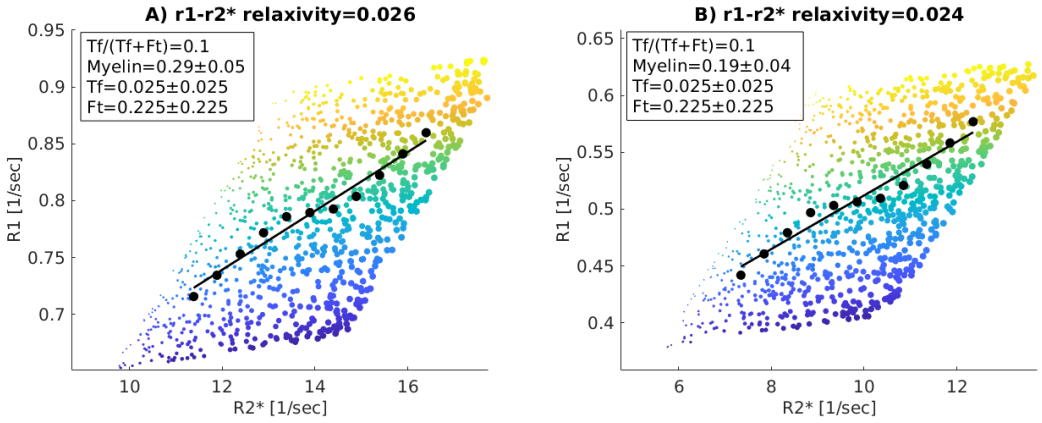


***Sup. Figure 27: The r1-r2* relaxivity in two simulated ROIs with different myelin concentrations, different ranges of myelin concentrations ($[\Delta M]$), and similar transferrin-ferritin fractions (Tf/(Tf+Ft))****; (A) WM; a higher myelin concentration and a larger range of myelin variability, the transferrin-ferritin fraction is 0.1; (B) GM; a lower myelin concentration and a lower range of myelin variability, the transferrin-ferritin fraction is 0.1. Each figure shows the dependency of R1 on R2* for 1,000 representative simulated voxels. The colors of the data points indicate the variability in myelin concentration across voxels, and their sizes indicate the variability in iron compounds concentration across voxels (the simulated concentrations are shown in the text box, myelin is in units of [fraction] as MTV, transferrin and ferritin are in units of [mg/ml]). As in our in vivo pipeline, R2* and R1 values were binned (black data points represent the bins' median), and a linear fit was calculated (black line). The slopes of the linear fit (shown in the title) represent the dependency of R1 on R2* (r1-r2* relaxivity) and vary slightly with the range of myelin variability ($[\Delta M]$).*

We further tested what are the myelin properties that would generate similar r1-r2* relaxivity effect as the effect observed when changing the transferrin-ferritin fraction (a change of 0.026 in the r1-r2* relaxivity, **Sup. Figure 24**). As changing the myelin concentration does not change the r1-r2* relaxivity (**Sup. Figure 26**), we changed the variability in myelin concentration within the ROI ($[\Delta M]$, **Sup. Figure 27**). We found that in order to generate a change of 0.026 in the r1-r2* relaxivity only through myelin-related changes (when the iron-related properties are fixed), the variability in MTV within the simulated ROI should be in the order of 0.187 [fraction] (**Sup. Figure 28**). Evaluating the *in vivo* variability in MTV within WM, GM and subcortical ROIs across 21 young subjects, the typical variability is ~ 0.09 [fraction], and the most extreme variability that was measured was 0.13 [fraction] (in the WM, **Sup. Figure 22**). Even this atypical value is still much lower than that required to generate a change of 0.026 in the r1-r2* relaxivity (0.187 [fraction] in MTV). Thus, there are no physiological myelin properties that would generate the r1-r2* relaxivity effect caused by the transferrin-ferritin properties.

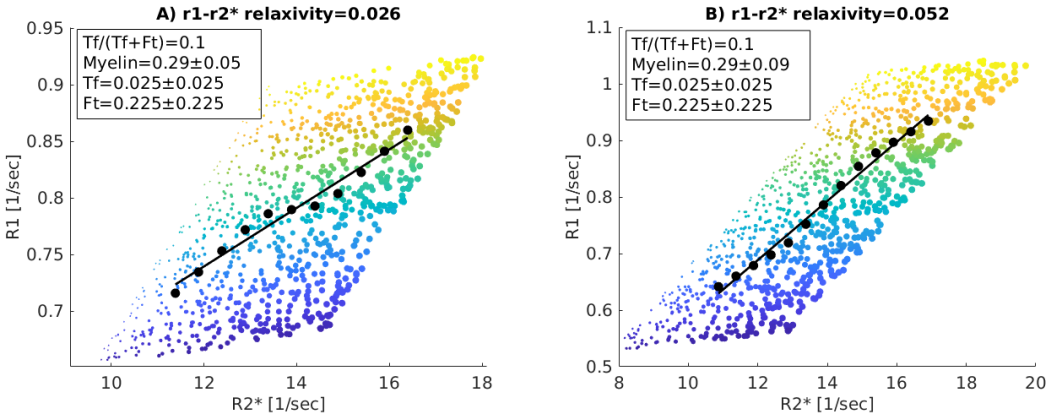


***Sup. Figure 28: The r1-r2* relaxivity in two simulated ROIs with different extreme ranges of myelin concentrations ($[\Delta M]$) and similar transferrin-ferritin fractions (Tf/(Tf+Ft));*** *(A) a physiological range of myelin variability, and a transferrin-ferritin fraction of 0.1; (B) the range of myelin variability is almost doubled, and the transferrin-ferritin fraction is 0.1. Each figure shows the dependency of R1 on R2* for 1,000 representative simulated voxels. The colors of the data points indicate the variability in myelin concentration across voxels, and their sizes indicate the variability in iron compounds concentration across voxels (the simulated concentrations are shown in the text box, myelin is in units of [fraction] as MTV, transferrin and ferritin are in units of [mg/ml]). As in our in vivo pipeline, R2* and R1 values were binned (black data points represent the bins' median), and a linear fit was calculated (black line). The slopes of the linear fit (shown in the title) represent the dependency of R1 on R2* (r1-r2* relaxivity) and change considerably under this condition of extreme variability in myelin concentration ($[\Delta M]$).*

The iron and myelin contents of brain tissue are tightly related, as iron is required for the formation of myelin[4]. To test how this affects the r1-r2* relaxivity measurement, we simulated a case where iron and myelin are completely correlated. Importantly, even in this extreme case, different transferrin-ferritin fractions exhibited different r1-r2* relaxivity (**Sup. Figure 29**).

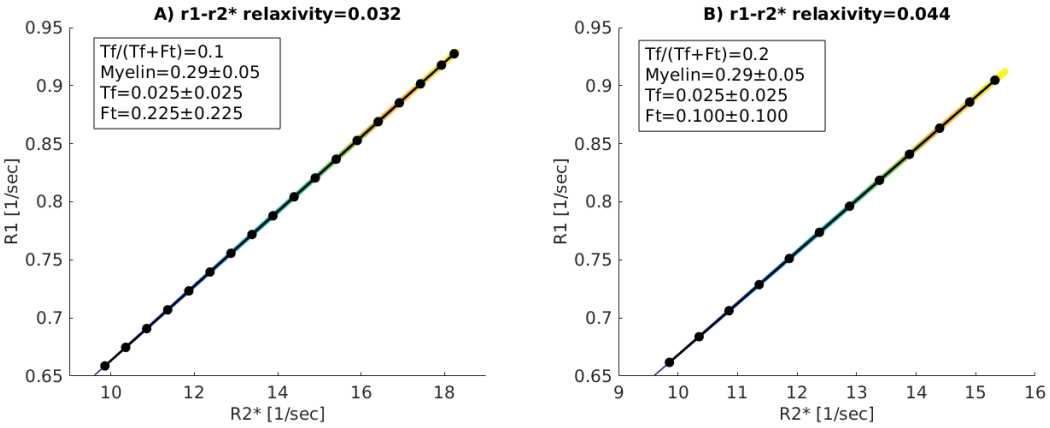


***Sup. Figure 29: The r1-r2* relaxivity in two simulated ROIs with different transferrin-ferritin fractions (Tf/(Tf+Ft)) and a correlation between iron and myelin concentrations across voxels****; (A) The transferrin-ferritin fraction is 0.1; (B) the transferrin-ferritin fraction is 0.2. In both A and B iron and myelin are correlated. Each figure shows the dependency of R1 on R2* for 1,000 representative*

*simulated voxels. The colors of the data points indicate the variability in myelin concentration across voxels, and their sizes indicate the variability in iron compounds concentration across voxels (the simulated concentrations are shown in the text box, myelin is in units of [fraction] as MTV, transferrin and ferritin are in units of [mg/ml]). As in our in vivo pipeline, R2* and R1 values were binned (black data points represent the bins' median), and a linear fit was calculated (black line). The slopes of the linear fit (shown in the title) represent the dependency of R1 on R2* (r1-r2* relaxivity) and change considerably with the transferrin-ferritin fraction even when iron and myelin are correlated.*

To conclude, we simulated a brain-like environment in order to test the biological sources affecting the r1-r2* relaxivity measurement. We found that physiological changes in the ferritin-transferrin fraction led to considerable changes in the r1-r2* relaxivity (0.026). This effect could not be attributed to the absolute concentrations of ferritin and transferrin, only to the ratio between them. To estimate whether the effect of changing the transferrin-ferritin fraction is measurable *in vivo*, we assessed the detection limit of the r1-r2* relaxivity measurement using scan-rescan experiments (**Sup. Figure 9**). We found that the changes in the r1-r2* relaxivity produced by different physiological transferrin-ferritin ratios are well above the detection limit of this MRI measurement *in vivo* (MEA~0.0035). Next, we confirmed that changes in the myelin concentration affect the measurements of R1 and R2*, but not the r1-r2* relaxivity. Setting the myelin variability within an ROI to typical GM and WM values led to a slight change in the r1-r2* relaxivity. However, we found that unrealistic myelin variability is required in order to produce the r1-r2* relaxivity effect observed for realistic changes in the transferrin-ferritin fraction. Therefore, while the myelin substantially affects the measurements of R1 and R2*, it is not the main component governing the measurement of the r1-r2* relaxivity, and under physiological conditions it cannot by itself explain the measured variability in the r1-r2* relaxivity across the brain.

## Supplementary Section 4.4: Comparison of the biophysical model to *in vivo* data of the human brain.

Predicting different features of the *in vivo* iron environment based on the r1-r2* relaxivity requires biophysical modeling of this MRI measurement. In our *in vitro* experiments with transferrin and ferritin mixtures (**Sup. Section 4.2**), we were able to accurately predict the r1-r2* relaxivity using the following model:

$$\text{S7)} \qquad \frac{\Delta R_1}{\Delta R_2^*} = \frac{[\Delta Ft]*r_{(1,Ft)}+[\Delta Tf]*r_{(1,Tf)}}{[\Delta Ft]*r_{(2,Ft)}+[\Delta Tf]*r_{(2,Tf)}} = \frac{(f*r_{(1,Tf)}+(1-f)*r_{(1,Ft)})}{(f*r_{(2,Tf)}+(1-f)*r_{(2,Ft)})}$$

Where $f = \frac{[\Delta Tf]}{[\Delta Ft]+[\Delta Tf]} = \frac{[Tf]}{[Ft]+[Tf]}$ (see eq. S4)

To implement the same model for human brain data, we used the transferrin-ferritin fraction ($f$) measured post-mortem for different brain regions of young and aged subjects[5,7,9]. The ferritin and transferrin relaxivities ($r_{(1/2,Tf/Ft)}$) were estimated based on the values measured *in vitro* for liposomal samples. While we find that the r1-r2* relaxivity measured *in vivo* is significantly correlated with the prediction of this biophysical model ($R^2$=0.55, p<0.001), the predicted r1-r2* relaxivities are not on the same order of magnitude as the measured r1-r2* relaxivities (MEA=0.012, **Sup. Figure 30**).

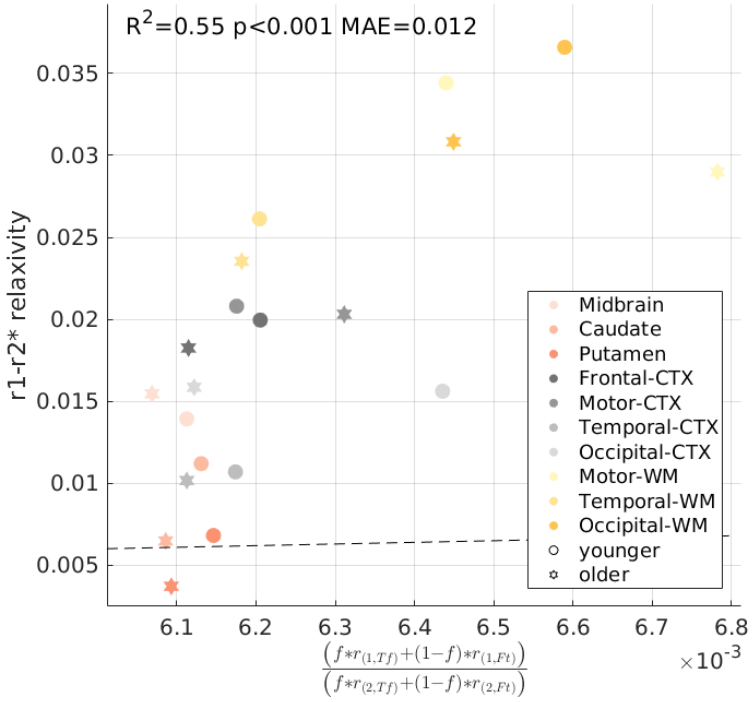


***Sup. Figure 30: Testing the r1-r2* relaxivity model presented in eq.* S7 *against in vivo data.*** *The y-axis shows the r1-r2* relaxivity measured in vivo across younger (aged 23-63 years, N =26) and older (aged 65-77 years, N=13) subjects (different marker shapes) in 10 brain regions (different colors). The x-axis shows the r1-r2* relaxivity predicted from the model (eq.* S7*); the transferrin-ferritin fractions (f) used in the model were measured post-mortem for different brain regions of young and aged subjects[5,7,9], the different relaxivities ($r_{(1/2,Tf/Ft)}$) were estimated based on the values measured in vitro for liposomal transferrin and ferritin samples (**Figure 1**). Dashed line is the identity line. MAE=mean absolute error.*

Therefore, while eq. S7 describes well the *in vitro* r1-r2* relaxivity (**Sup. Figure 21**), in the brain it provides a much lower estimation for the r1-r2* relaxivity compared to the measured *in vivo* values (**Sup. Figure 30**). An explanation for this result could be that in our *in vitro* mixtures experiments (**Sup. Section 4.2**) the liposomal fraction, which mimics the myelin content, was fixed. In eq. S5 and in our numerical simulations we find that the variability in myelin and iron within an ROI can contribute to the measurement of the r1-r2* relaxivity. We tested whether adding the myelin and iron variability to the

model can improve the estimation of the *in vivo* r1-r2* relaxivities. Rearranging eq. S5 we find that the strength of the myelin effect on the r1-r2* relaxivity depends on how variable is the myelin content within an ROI relative to how variable is the iron content ($\frac{[\Delta M]}{[\Delta iron]}$):

$$S8) \quad \frac{\Delta R_1}{\Delta R_2^*} = \frac{(f*r_{(1,Ft)}+(1-f)r_{(1,Tf)})+r_{(1,M)}\frac{[\Delta M]}{[\Delta iron]}}{(f*r_{(2,Ft)}+(1-f)r_{(2,Tf)})+r_{(2,M)}\frac{[\Delta M]}{[\Delta iron]}}$$

In order to incorporate the myelin into the model, we estimated the myelin relaxivities ($r_{(1/2,M)}$) based on the linear dependency of R1 and R2* on MTV, averaged across WM and GM regions in the brains of 21 young subjects (as was done in the numerical simulations). The iron-related parameters were similar to the ones used for the modeling in eq. S7. The ratio of myelin to iron variability ($\frac{[\Delta M]}{[\Delta iron]}$) was fitted as a free parameter. Notably, due to the added free parameter, the model is no longer fully-constrained. Adding a parameter to account for the myelin relaxivity improved the model's ability to capture the magnitude of the measured r1-r2* relaxivity in the brain (MEA=0.006), but reduced the correlation between the model's predictions and the measured r1-r2* relaxivities ($R^2$=0.38, p<0.01, **Sup. Figure 31**). To estimate the contribution of myelin to the r1-r2* relaxivity more directly, we used the myelin marker MTV and found that it is not correlated with the r1-r2* relaxivity ($R^2$=0.21, p(FDR)=n.s., **Sup. Figure 12**). These results imply that the myelin is not the main component governing the r1-r2* relaxivity measurement in the brain.

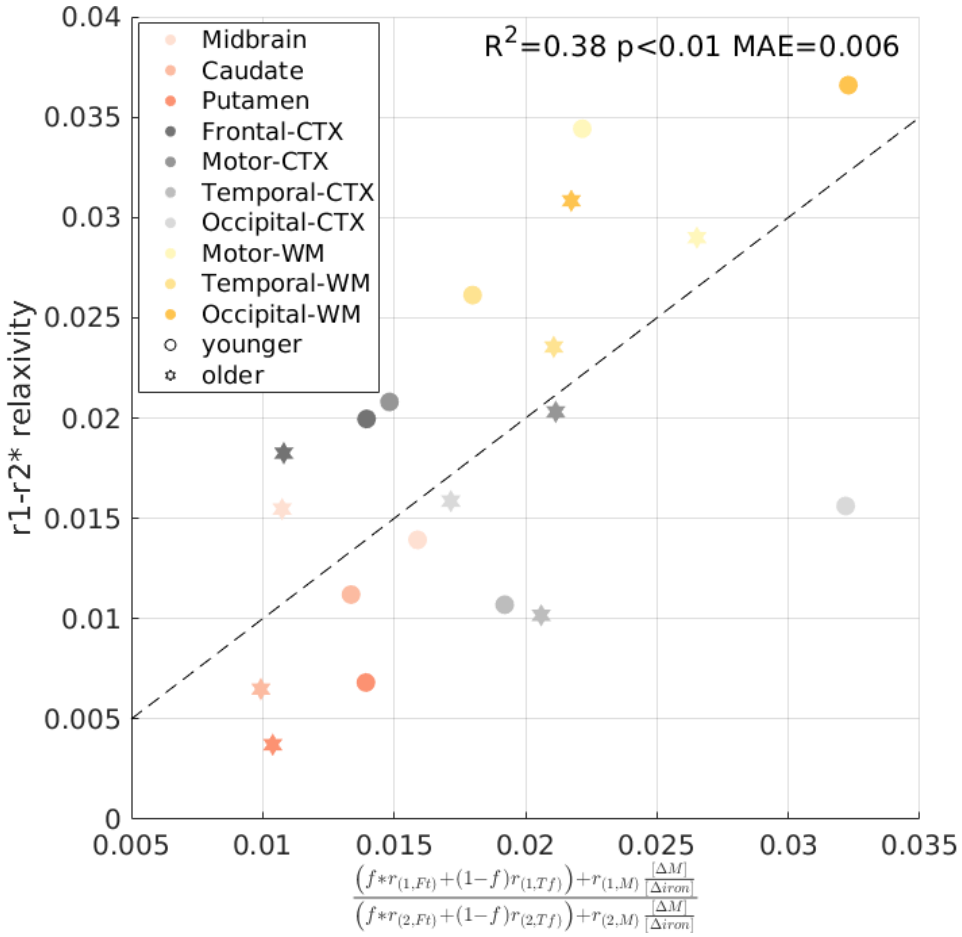


***Sup. Figure 31:** Testing the r1-r2* relaxivity model including myelin (eq. S8) against in vivo data.* *The y-axis shows the r1-r2* relaxivity measured in vivo across younger (aged 23-63 years, N =26) and older (aged 65-77 years, N=13) subjects (different marker shapes) in 10 brain regions (different colors). The x-axis shows the r1-r2* relaxivity predicted from the model (eq. S8); the transferrin-ferritin fractions (f) used in the model were measured post-mortem for different brain regions of young and aged subjects[5,7,9], the ferritin and transferrin relaxivities ($r_{(1/2,Tf/Ft)}$) were estimated based on the values measured in vitro for liposomal transferrin and ferritin samples (Figure 1), the myelin relaxivities ($r_{(1/2,M)}$) were estimated based on the in vivo linear dependency of R1 and R2* on the myelin marker MTV (averaged across WM and GM regions in the brains of 21 young subjects). The ratio of myelin to iron variability ($\frac{[\Delta M]}{[\Delta iron]}$) was fitted as a free parameter. Dashed line is the identity line. MAE=mean absolute error.*

Next, we tested whether biophysical considerations could explain the fact that eq. S7 describes well the *in vitro* r1-r2* relaxivity (**Sup. Figure 21**), but in the brain it provides much lower estimation for the r1-r2* relaxivity compared to the measured *in vivo* values (**Sup. Figure 30**). One of the assumptions of the described model (eq. S7) is that water can freely diffuse. While this assumption seems valid for *in vitro* samples, brain tissue is often characterized by compartmentalization[79,81]. Under the fast exchange limit, it is assumed that each compartment displays a single relaxation rate, and that the rate of water exchange

between compartments is much faster than the difference between the compartmental relaxation rates[81]. In this case, the observed relaxation rate ($R_{1/2}$) is obtained by the weighted sum of the compartmental relaxation rates:

$$R_{1/2} = \sum_{i=1}^{n} P_i \, R_{1/2}^i$$

Where $R_{1/2}^i$ is the relaxation rate of the i'th compartment, and $P_i$ is its fractional water population ($\sum_{i=1}^{n} P_i = 1$).

We hypothesized that under the fast exchange limit, the r1-r2* relaxivity is also obtained by the weighted sum of the compartmental relaxivities:

$$S9) \qquad \frac{\Delta R_1}{\Delta R_2^*} = (1-f) * \frac{r_{(1,Ft)}}{r_{(2,Ft)}} + f * \frac{r_{(1,Tf)}}{r_{(2,Tf)}}$$

Where $\frac{r_{(1,Ft)}}{r_{(2,Ft)}}$ and $\frac{r_{(1,Tf)}}{r_{(2,Tf)}}$ are the r1-r2* relaxivities of ferritin and transferrin respectively and $f = \frac{[Tf]}{[Ft]+[Tf]}$.

In the next section, we will show that eq. S9 follows directly from the assumptions of compartmentalization and fast-exchange. In brain tissue, ferritin is known to have a patchy spatial distribution, while transferrin's distribution in space is more uniform[3]. We will therefore assume that ferritin is biologically compartmentalized. This situation can be described by a two-compartment model, similar to the case of compartmentalized contrast agent[79]. The ferritin compartment (FC) includes both ferritin and transferrin, with relaxation rate:

$$R_{(1/2,FC)} = r_{(1/2,Ft)}[Ft] + r_{(1/2,Tf)}[Tf]$$

As ferritin is compartmentalized, the non-ferritin compartment (NC) only includes transferrin:

$$R_{(1/2,NC)} = r_{(1/2,Tf)}[Tf]$$

Assuming fast-exchange between the FC and NC compartments, the total relaxation rate:

$$\begin{aligned} R_{1/2} &= P_{FC} R_{(1/2,FC)} + P_{NC} R_{(1/2,NC)} \\ &= P_{FC}\left(r_{(1/2,Ft)}[Ft] + r_{(1/2,Tf)}[Tf]\right) + P_{NC}\left(r_{(1/2,Tf)}[Tf]\right) \\ &= P_{FC} r_{(1/2,Ft)}[Ft] + r_{(1/2,Tf)}[Tf] \end{aligned}$$

Where $P_{FC}$ is the fractional water population in the ferritin compartment and $P_{NC}$ represent the rest of the water in the non-ferritin compartment ($P_{FC} + P_{NC} = 1$).

The r1-r2* relaxivity in this case:

$$S10) \qquad \frac{\Delta R_1}{\Delta R_2^*} = \frac{r_{(1,Tf)}[\Delta Tf] + P_{FC} * r_{(1,Ft)}[\Delta Ft]}{r_{(2,Tf)}[\Delta Tf] + P_{FC} * r_{(2,Ft)}[\Delta Ft]} = \frac{f * r_{(1,Tf)} + P_{FC}(1-f) * r_{(1,Ft)}}{f * r_{(2,Tf)} + P_{FC}(1-f) * r_{(2,Ft)}}$$

Where $f = \frac{[\Delta Tf]}{[\Delta Ft]+[\Delta Tf]} = \frac{[Tf]}{[Ft]+[Tf]}$ (eq. S4).

The presented biophysical model (eq. S10) is very similar to free-diffusion model (eq. S7), only with the factor $P_{FC}$ which limits the effect of ferritin due to its compartmentalization. We found that the fast-exchange limit for the r1-r2* relaxivity (eq. S9) is, in fact, a private case of the compartmental fast-exchange model (eq. 10) with $P_{FC} = \frac{r_{(2,Tf)}}{r_{(2,Ft)}} = 0.012$ (for the full derivation see **Sup. Section 4.5**):

$$S11) \qquad \frac{\Delta R_1}{\Delta R_2^*} = (1-f) * \frac{r_{(1,Ft)}}{r_{(2,Ft)}} + f * \frac{r_{(1,Tf)}}{r_{(2,Tf)}} = \frac{f * r_{(1,Tf)} + \left(\frac{r_{(2,Tf)}}{r_{(2,Ft)}}\right)(1-f) * r_{(1,Ft)}}{f * r_{(2,Tf)} + \left(\frac{r_{(2,Tf)}}{r_{(2,Ft)}}\right)(1-f) * r_{(2,Ft)}}$$

Importantly, by employing this compartmental fast-exchange model (eq. S9) we were able to accurately predict the r1-r2* relaxivity measured *in vivo* across brain regions and age groups ($R^2$=0.57, p<0.001, **Sup. Figure 32**). Unlike the free diffusion model (eq. S7), the predictions from the compartmental fast-exchange model were correlated with the *in vivo* r1-r2* relaxivity and were also in the same order of magnitude (MEA=0.0067). Moreover, while adding the myelin to the free diffusion model required a fitting of a free parameter (**Sup. Figure 31**), the fast-exchange model which is only based on iron-related features is fully-constrained and provides a better prediction for the r1-r2* relaxivities. Notably, rearranging this model allows to successfully predict the transferrin-ferritin fraction in the brain without any free parameter (**Figure 4c,** Eq. 8 in Methods):

$$f = \frac{\frac{\Delta R_1}{\Delta R_2^*} - \frac{r_{(1,Ft)}}{r_{(2,Ft)}}}{\frac{r_{(1,Tf)}}{r_{(2,Tf)}} - \frac{r_{(1,Ft)}}{r_{(2,Ft)}}}$$

These results imply that the compartmentalized nature of brain tissue may be the biophysical source for the fact that the one model was accurate for *in vitro* samples (free diffusion, **Sup. Figure 21**, eq. S7), while a different model accurately described *in vivo* data (compartmental fast-exchange model, **Sup. Figure 32**, eq. S11).

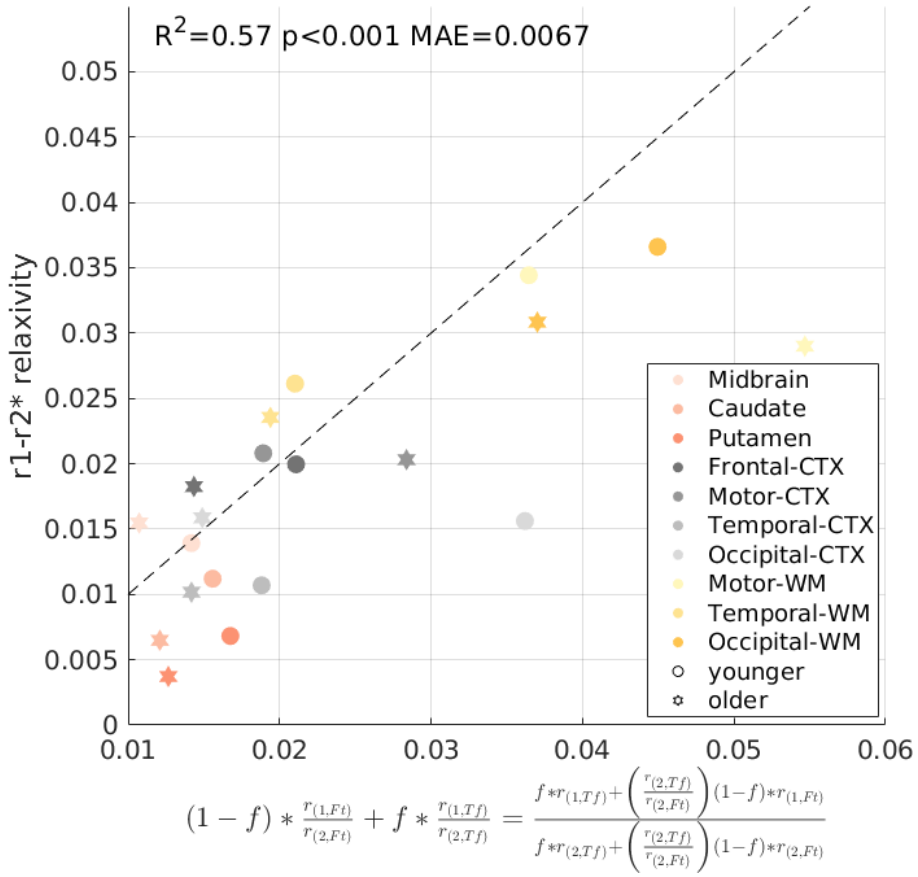


***Sup. Figure 32:** Testing the fast-exchange r1-r2* relaxivity model (eq.* S11*) against in vivo data.* *The y-axis shows the r1-r2* relaxivity measured in vivo across younger (aged 23-63 years, N =26) and older (aged 65-77 years, N=13) subjects (different marker shapes) in 10 brain regions (different colors). The x-axis shows the r1-r2* relaxivity predicted from the fast-exchange model (eq.* S11*); the transferrin-ferritin fractions (f) used in the model were measured post-mortem for different brain regions of young and aged subjects*[5,7,9]*, the different relaxivities ($r_{(1/2,Tf/Ft)}$) were estimated based on the values measured in vitro for liposomal transferrin and ferritin samples (**Figure 1**). Dashed line is the identity line. MAE=mean absolute error.*

Interestingly, though describing different biophysical settings, both models (eq. S7, **Sup. Figure 30** ; eq. S11, **Sup. Figure 32**) were correlated with the r1-r2* relaxivities in the brain. We noticed that both models can be approximated as a linear function of the transferrin-ferritin ratio ($\frac{[Tf]}{[Ft]}$, for the full derivation see **Sup. Section 4.6**):

$$\frac{\left(f*r_{(1,Tf)}+(1-f)r_{(1,Ft)}\right)}{\left(f*r_{(2,Tf)}+(1-f)r_{(2,Ft)}\right)}\cong\frac{r_{(1,Ft)}}{r_{(2,Ft)}}+\frac{[Tf]}{[Ft]}*\frac{1}{r_{(2,Ft)}}\left(r_{(1,Tf)}-\frac{r_{(2,Tf)}*r_{(1,Ft)}}{r_{(2,Ft)}}\right)$$

$$(1-f)*\frac{r_{(1,Ft)}}{r_{(2,Ft)}}+f*\frac{r_{(1,Tf)}}{r_{(2,Tf)}}\cong\frac{r_{(1,Ft)}}{r_{(2,Ft)}}+\frac{[Tf]}{[Ft]}*\left(\frac{r_{(1,Tf)}}{r_{(2,Tf)}}-\frac{r_{(1,Ft)}}{r_{(2,Ft)}}\right)$$

Under this linear approximation the only difference between the models is that they have different slopes. This can explain why both models were correlated with the r1-r2* relaxivity measured *in vivo*.

The proposed biophysical frameworks (eq. S11) provides a rather good prediction for the measured r1-r2* relaxivity only based on iron-related features without modeling the myelin contribution. We further assessed whether adding the myelin content to this model can improve the r1-r2* relaxivity prediction. For this aim we used the form of the compartmental fast-exchange model described in eq. S11, and added the myelin contribution:

$$\text{S12)} \qquad \frac{\Delta R_1}{\Delta R_2^*} = \frac{f*r_{(1,Tf)}+\left(\frac{r_{(2,Tf)}}{r_{(2,Ft)}}\right)(1-f)*r_{(1,Ft)}+r_{(1,M)}\frac{[\Delta M]}{[\Delta iron]}}{f*r_{(2,Tf)}+\left(\frac{r_{(2,Tf)}}{r_{(2,Ft)}}\right)(1-f)*r_{(2,Ft)}+r_{(2,M)}\frac{[\Delta M]}{[\Delta iron]}}$$

The myelin relaxivities ($r_{(1/2,M)}$) were estimated as the linear dependency of R1 and R2* on MTV, averaged across WM and GM regions in the brains of 21 young subjects (as was done in the numerical simulations). The ratio of myelin to iron variability ($\frac{[\Delta M]}{[\Delta iron]}$) was fitted as free parameter. Notably, due to the added free parameter the model is no longer fully-constrained. Still, we only found slight improvement in the mean absolute error (MEA) compared to the model without the myelin (MEA=0.0059, **Sup. Figure 33**). Nonetheless, the measurements of R1 and R2* are highly sensitive to myelin[4,19,25,29,39–43] and correlate with MTV (**Sup. Figure 12**). We hypothesized that when combining these two measurements for calculating the r1-r2* relaxivity of liposomal ferritin and transferrin, the effect of myelin might be already included in the relaxivities. Indeed, testing the compartmental fast-exchange model (eq. S9) using the r1-r2* relaxivities of ferritin and transferrin without liposomes, the prediction is much less accurate in terms its ability to capture the magnitude of the measured r1-r2* relaxivities in the brain (MEA=0.043, **Sup. Figure 34**). Therefore, we assume that by using the r1-r2* relaxivities of liposomal ferritin and liposomal transferrin in the model, the myelin contribution might be accounted for.

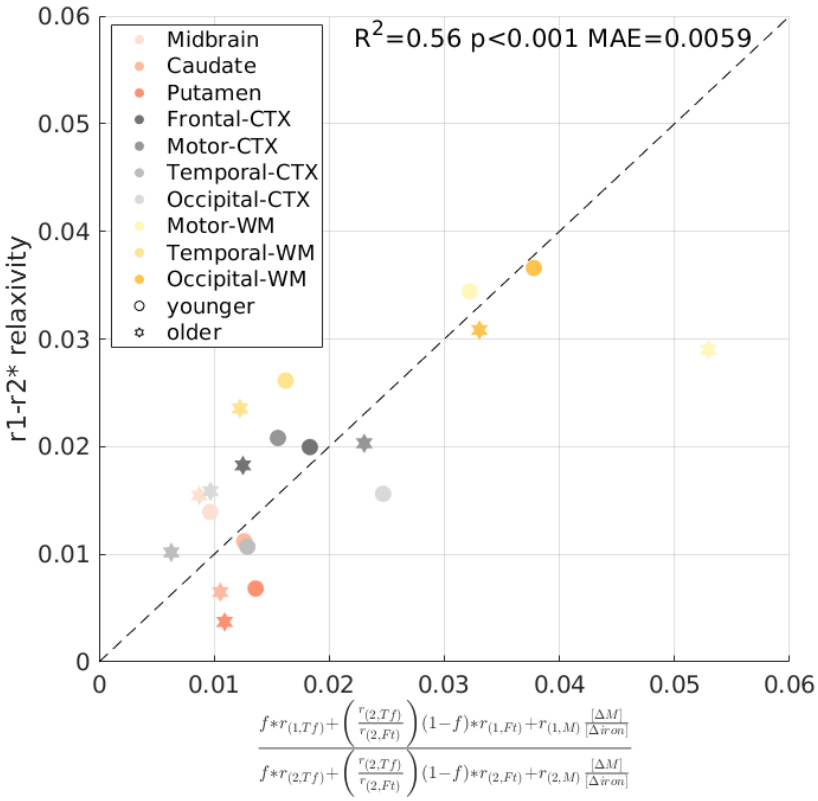


***Sup. Figure 33:** Testing the fast exchange r1-r2* relaxivity model including myelin (eq.* S12*) against in vivo data. The y-axis shows the r1-r2* relaxivity measured in vivo across younger (aged 23-63 years, N =26) and older (aged 65-77 years, N=13) subjects (different marker shapes) in 10 brain regions (different colors). The x-axis shows the r1-r2* relaxivity predicted from the fast exchange model (eq.* S12*); the transferrin-ferritin fractions (f) used in the model were measured post-mortem for different brain regions of young and aged subjects[5,7,9], the ferritin and transferrin relaxivities ($r_{(1/2,Tf/Ft)}$) were estimated based on the values measured in vitro for liposomal transferrin and ferritin samples (**Figure 1**), the myelin relaxivities ($r_{(1/2,M)}$) were estimated based on the in vivo linear dependency of R1 and R2* on the myelin marker MTV (averaged across WM and GM regions in the brains of 21 young subjects). The ratio of myelin to iron variability ($\frac{[\Delta M]}{[\Delta iron]}$) was fitted as free parameter. Dashed line is the identity line. MAE=mean absolute error.*

To conclude, these results imply that compartmentalization of ferritin in brain tissue, which does not occur in solutions[32,82], can explain the discrepancies between the successful prediction of the *in vitro* r1-r2* relaxivity by the free-diffusion model (eq. S7, **Sup. Figure 21**) to the successful prediction of the *in vivo* r1-r2* relaxivity by the compartmental fast-exchange model (**Sup. Figure 32**, eq. S11). Interestingly, we found that the fractional compartmentalization of ferritin can be described solely by the ratio of the ferritin and transferrin R2* relaxivities ($\frac{r_{(2,Tf)}}{r_{(2,Ft)}}$, eq. S11). This indicates, as previously suggested, that the ferritin compartmentalization might be due to magnetic susceptibility effects rather than to pure

anatomical divisions[32,82,83]. Ghugre et. al.[83] describe this phenomena by a combined inner-sphere and outer-sphere relaxation, in which the boundaries between these relaxation mechanisms are not physical but rather depend upon the iron load, particle size, inter-echo spacing, and proton mobility.

While adding the myelin contribution to the model can also improve its performances, it requires parameter fitting (**Sup. Figure 31**). Notably, we find that the myelin content by itself does not allow to predict the r1-r2* relaxivity (**Sup. Figure 12**). The prediction abilities of the combined iron and myelin model are equivalent to the compartmental fast-exchange model which is only based on iron-related features, but the latter is fully-constrained (no free parameters) and is more compact. Therefore, we choose to use the compartmental fast-exchange model for predicting the transferrin-ferritin fraction in the *in vivo* brain (**Figure 4c**). This model's successful predictions abilities were even replicated on an independent data set (**Sup. Figure 39**). Yet, further experiments are needed in order to fully determine which of the proposed biophysical models provides the most accurate description of brain tissue r1-r2* relaxivity.

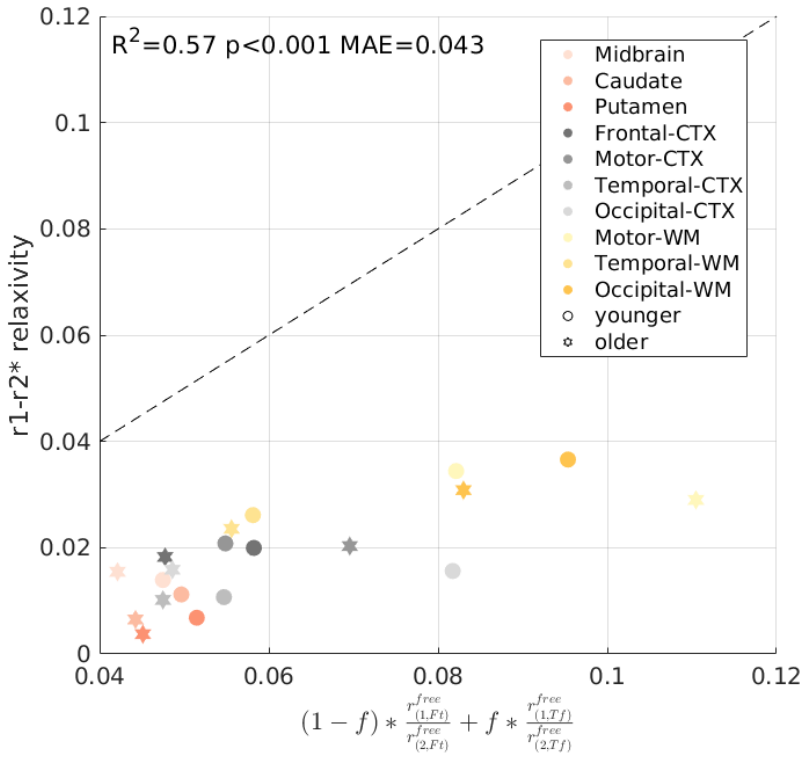


***Sup. Figure 34:** Testing the fast-exchange r1-r2* relaxivity model with the relaxivities of free transferrin and ferritin (eq.* S9*) against in vivo data. The y-axis shows the r1-r2* relaxivity measured in vivo across younger (aged 23-63 years, N =26) and older (aged 65-77 years, N=13) subjects (different marker shapes) in 10 brain regions (different colors). The x-axis shows the r1-r2* relaxivity predicted from the fast-*

*exchange model (eq.* S9*); the transferrin-ferritin fractions (f) used in the model were measured post-mortem for different brain regions of young and aged subjects[5,7,9], the different relaxivities ($r_{(1/2,Tf/Ft)}$) were estimated based on the values measured in vitro for free transferrin and ferritin samples (without liposomes,* ***Figure 1****). Dashed line is the identity line. MAE=mean absolute error.*

## Supplementary Section 4.5: Development of the compartmental fast-exchange model for predicting the r1-r2* relaxivities.

Here we show that the fast-exchange limit for the r1-r2* relaxivity (eq. S9), is in fact a private case of the compartmental fast-exchange model (eq. S10) with $P_{FC} = \frac{r_{(2,Tf)}}{r_{(2,Ft)}}$ (eq. S11):

$$\frac{r_{(1,Ft)}[Ft]\left(\frac{r_{(2,Tf)}}{r_{(2,Ft)}}\right) + [Tf]r_{(1,Tf)}}{r_{(2,Ft)}[Ft]\left(\frac{r_{(2,Tf)}}{r_{(2,Ft)}}\right) + [Tf] * r_{(2,Tf)}} = \frac{[Ft]r_{(1,Ft)}r_{(2,Tf)} + [Tf]r_{(1,Tf)}r_{(2,Ft)}}{[Ft]r_{(2,Ft)}r_{(2,Tf)} + [Tf] * r_{(2,Tf)}r_{(2,Ft)}}$$

$$= \frac{\frac{[Ft]r_{(1,Ft)}r_{(2,Tf)}}{[Ft]r_{(2,Ft)}r_{(2,Tf)}} + \frac{[Tf]r_{(1,Tf)}r_{(2,Ft)}}{[Ft]r_{(2,Ft)}r_{(2,Tf)}}}{1 + \frac{[Tf]}{[Ft]}}$$

$$= \left(\frac{1}{1 + \frac{[Tf]}{[Ft]}}\right)\left(\frac{r_{(1,Ft)}}{r_{(2,Ft)}} + \frac{[Tf]r_{(1,Tf)}}{[Ft]r_{(2,Tf)}}\right)$$

$$= \frac{[Ft]}{[Ft] + [Tf]}\left(\frac{r_{(1,Ft)}}{r_{(2,Ft)}} + \frac{[Tf]r_{(1,Tf)}}{[Ft]r_{(2,Tf)}}\right)$$

$$= \frac{[Ft]}{[Ft] + [Tf]}\frac{r_{(1,Ft)}}{r_{(2,Ft)}} + \frac{[Ft]}{[Ft] + [Tf]} * \frac{[Tf]r_{(1,Tf)}}{[Ft]r_{(2,Tf)}}$$

$$= \frac{[Ft]}{[Ft] + [Tf]}\frac{r_{(1,Ft)}}{r_{(2,Ft)}} + \frac{[Tf]}{[Ft] + [Tf]} * \frac{r_{(1,Tf)}}{r_{(2,Tf)}}$$

$$= (1 - f)\frac{r_{(1,Ft)}}{r_{(2,Ft)}} + f * \frac{r_{(1,Tf)}}{r_{(2,Tf)}}$$

## Supplementary Section 4.6: Linear approximation of the biophysical relaxivity models.

Eq. S7 can be approximated to show linear relationship with the transferrin-ferritin ratio ($\frac{[Tf]}{[Ft]}$):

As $\left|\frac{[Tf]*r_{(2,Tf)}}{[Ft]*r_{(2,Ft)}}\right| < 1$, we can use the Taylor approximation:

$$\frac{1}{1 + \frac{[Tf] * r_{(2,Tf)}}{[Ft] * r_{(2,Ft)}}} \cong 1 - \frac{[Tf] * r_{(2,Tf)}}{[Ft] * r_{(2,Ft)}}$$

And the linear approximation of eq. S7:

$$\frac{[Ft]*r_{(1,Ft)}+[Tf]*r_{(1,Tf)}}{[Ft]*r_{(2,Ft)}+[Tf]*r_{(2,Tf)}} = \frac{\frac{[Ft]*r_{(1,Ft)}}{[Ft]*r_{(2,Ft)}}+\frac{[Tf]*r_{(1,Tf)}}{[Ft]*r_{(2,Ft)}}}{1+\frac{[Tf]*r_{(2,Tf)}}{[Ft]*r_{(2,Ft)}}}$$

$$= \frac{\frac{r_{(1,Ft)}}{r_{(2,Ft)}}+\frac{[Tf]*r_{(1,Tf)}}{[Ft]*r_{(2,Ft)}}}{1+\frac{[Tf]*r_{(2,Tf)}}{[Ft]*r_{(2,Ft)}}}$$

$$= \frac{1}{1+\frac{[Tf]*r_{(2,Tf)}}{[Ft]*r_{(2,Ft)}}} * \left(\frac{r_{(1,Ft)}}{r_{(2,Ft)}}+\frac{[Tf]*r_{(1,Tf)}}{[Ft]*r_{(2,Ft)}}\right)$$

$$\cong \left(1-\frac{[Tf]*r_{(2,Tf)}}{[Ft]*r_{(2,Ft)}}\right)\left(\frac{r_{(1,Ft)}}{r_{(2,Ft)}}+\frac{[Tf]*r_{(1,Tf)}}{[Ft]*r_{(2,Ft)}}\right)$$

$$\cong \frac{r_{(1,Ft)}}{r_{(2,Ft)}}+\frac{[Tf]*r_{(1,Tf)}}{[Ft]*r_{(2,Ft)}}-\frac{[Tf]*r_{(2,Tf)}}{[Ft]*r_{(2,Ft)}}*\frac{r_{(1,Ft)}}{r_{(2,Ft)}}-\left(\frac{[Tf]}{[Ft]}\right)^2\frac{r_{(2,Tf)}*r_{(1,Tf)}}{r_{(2,Ft)}*r_{(2,Ft)}}$$

$$\cong \frac{r_{(1,Ft)}}{r_{(2,Ft)}}+\frac{[Tf]}{[Ft]}*\frac{1}{r_{(2,Ft)}}\left(r_{(1,Tf)}-\frac{r_{(2,Tf)}*r_{(1,Ft)}}{r_{(2,Ft)}}\right)-\left(\frac{[Tf]}{[Ft]}\right)^2\frac{r_{(2,Tf)}*r_{(1,Tf)}}{r_{(2,Ft)}*r_{(2,Ft)}}$$

$$\cong \frac{r_{(1,Ft)}}{r_{(2,Ft)}}+\frac{[Tf]}{[Ft]}*\frac{1}{r_{(2,Ft)}}\left(r_{(1,Tf)}-\frac{r_{(2,Tf)}*r_{(1,Ft)}}{r_{(2,Ft)}}\right)$$

We show that this linear approximation is valid by plugging the literature values of $[Tf]$ and $[Ft]$[5,7,9] and the relaxivities of ferritin and transferrin measured *in vitro* (**Sup. Figure 35**).

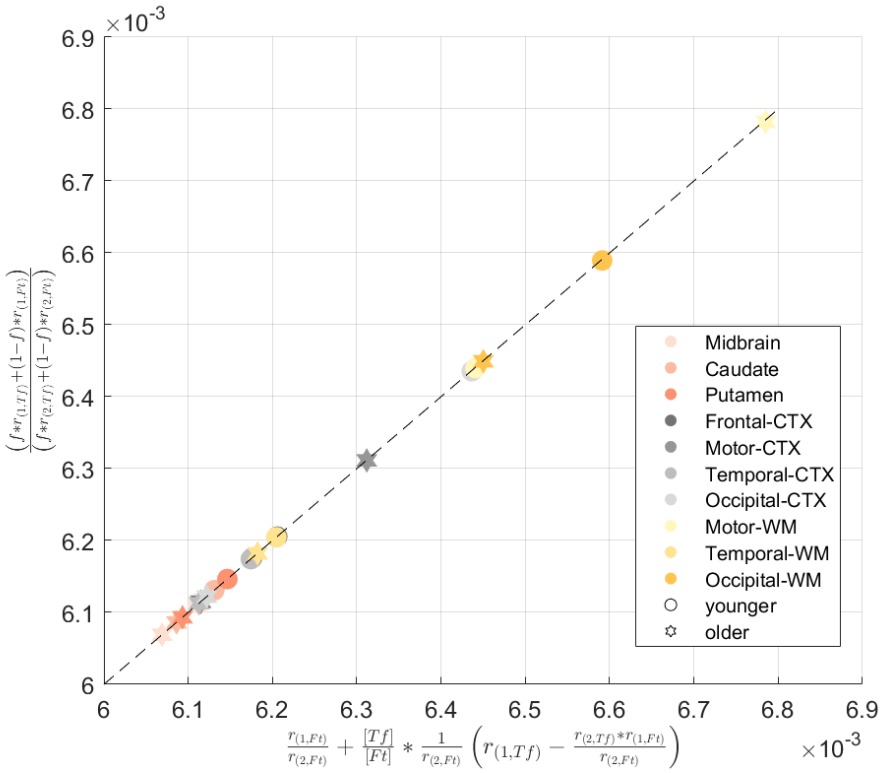


***Sup. Figure 35:** Testing the linear approximation of the r1-r2* relaxivity model (eq.* S7*) against the full model.* *The y-axis shows the r1-r2* relaxivity predicted from the model (eq.* S7*); the transferrin-ferritin fractions (f) used in the model were measured post-mortem for different brain regions of young and aged subjects[5,7,9], the different relaxivities ($r_{(1/2,Tf/Ft)}$) were estimated based on the values measured in vitro for liposomal transferrin and ferritin samples (**Figure 1**). The x-axis shows the r1-r2* relaxivity predicted from the linear approximation of the model. Dashed line is the identity line.*

Eq. S11 can also be approximated to show linear relationship with the transferrin-ferritin ratio ($\frac{[Tf]}{[Ft]}$):

As $\left|\frac{[Tf]}{[Ft]}\right| < 1$, the Taylor approximation:

$$\frac{[Ft]}{[Tf]+[Ft]} = \frac{1}{\frac{[Tf]}{[Ft]}+1} \cong 1 - \frac{[Tf]}{[Ft]}$$

$$\frac{[Tf]}{[Tf]+[Ft]} = 1 - \frac{[Ft]}{[Tf]+[Ft]} \cong 1 - \left(1 - \frac{[Tf]}{[Ft]}\right) = \frac{[Tf]}{[Ft]}$$

And the linear approximation of eq. S11:

$$\frac{[Ft]}{[Tf]+[Ft]} * \frac{r_{(1,Ft)}}{r_{(2,Ft)}} + \frac{[Tf]}{[Tf]+[Ft]} * \frac{r_{(1,Tf)}}{r_{(2,Tf)}} \cong \left(1 - \frac{[Tf]}{[Ft]}\right)\frac{r_{(1,Ft)}}{r_{(2,Ft)}} + \left(\frac{[Tf]}{[Ft]}\right) * \frac{r_{(1,Tf)}}{r_{(2,Tf)}}$$
$$\cong \frac{r_{(1,Ft)}}{r_{(2,Ft)}} + \frac{[Tf]}{[Ft]} * \left(\frac{r_{(1,Tf)}}{r_{(2,Tf)}} - \frac{r_{(1,Ft)}}{r_{(2,Ft)}}\right)$$

We show that this linear approximation is valid by plugging the literature values of $[Tf]$ and $[Ft]$[5,7,9] and the relaxivities of ferritin and transferrin measured *in vitro* (**Sup. Figure 36**).

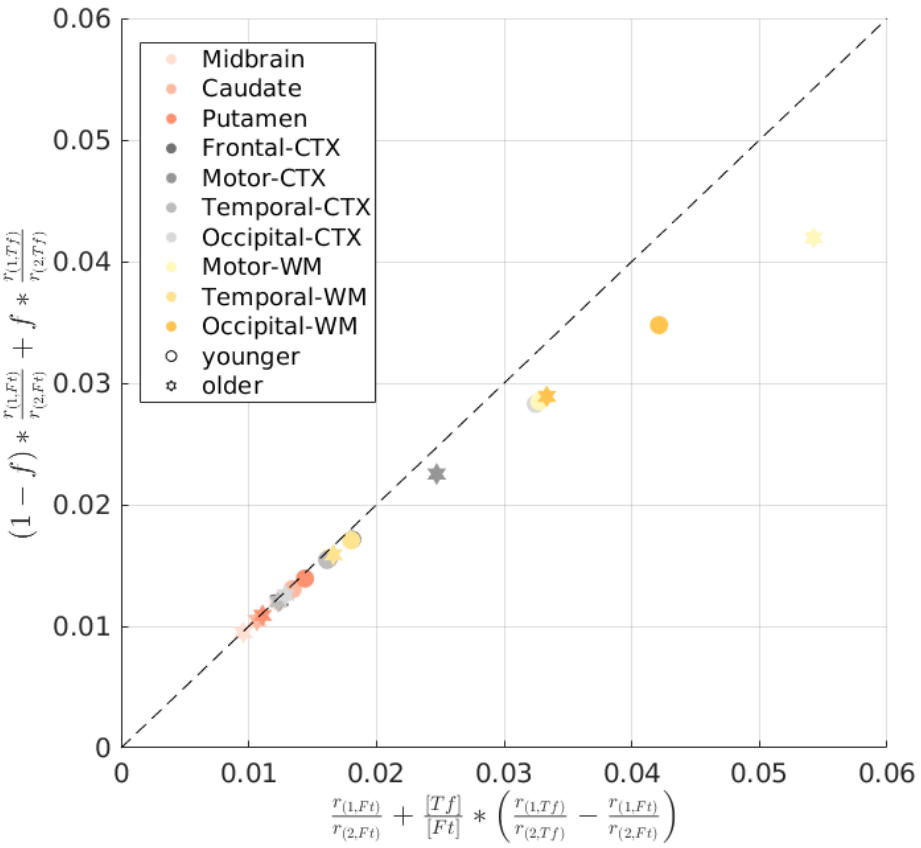


***Sup. Figure 36:** Testing the linear approximation of the fast-exchange r1-r2* relaxivity model (eq. $S11$) against the full model. The y-axis shows the r1-r2* relaxivity predicted from the fast-exchange model (eq. S11); the transferrin-ferritin fractions (f) used in the model were measured post-mortem for different brain regions of young and aged subjects[5,7,9], the different relaxivities ($r_{(1/2,Tf/Ft)}$) were estimated based on the values measured in vitro for liposomal transferrin and ferritin samples (**Figure 1**). The x-axis shows the r1-r2* relaxivity predicted from the linear approximation of the fast-exchange model. Dashed line is the identity line.*

## Supplementary Section 5: The r1-r2* relaxivity in the pallidum.

The pallidum is unique in terms of its paramagnetic properties: it is highly rich in iron, but also contains iron oxides and metal depositions[3,84,85] which might affect the measurement of the r1-r2* relaxivity.

While our biophysical model for prediction the transferrin fraction (**Figure 4c**) was successful in most brain regions, it failed to explain the r1-r2* relaxivity in the pallidum. For young subjects, R1 and R2* values in the pallidum were the highest among all regions tested, and the r1-r2* relaxivity was the lowest. By definition, as our model is based on the weighted sum of ferritin and transferrin, its predictions span between the r1-r2* relaxivities measured *in vitro* for ferritin and transferrin. The low r1-r2* relaxivity in the pallidum was lower than this range, leading to a negative prediction for its transferrin- ferritin fraction (**Sup. Figure 37**). This prediction is very different from the literature value[5,7,9], especially for young subjects.

As a result of the outlier values in the pallidum, we excluded it from the comparisons between MRI and histology we show for R2* and the iron concentration and foe the *r1-r2** relaxivity and the transferrin/iron ratio (**Figure 4b**, **Sup. Figure 16**). However, these correlations remain significant even when the pallidum is included in the analysis (**Sup. Figure 38**).

When the pallidum was included in the analysis, we found additional, weaker correlations between MRI measurements and the concentrations of iron, ferritin and transferrin. However, these correlations were driven mostly by the distinct behavior of the pallidum, and they did not survive after this outlier was removed from the analysis. Only the correlation between R2* and the iron concentration and between the r1-r2* relaxivities and the transferrin/iron ratio remained significant after excluding the pallidum. We therefore decided to exclude the pallidum from the main analysis.

## Supplementary Figure 37

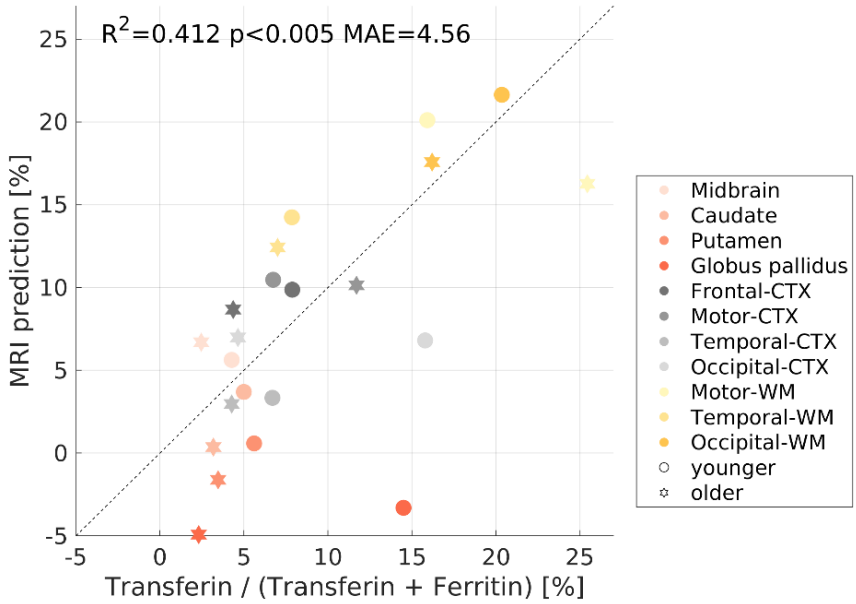


***Sup. Figure 37: The prediction of the transferrin-to-ferritin fraction is inaccurate in the pallidum.*** *The measured r1-r2* relaxivity in each brain area was modeled as a weighted sum of the r1-r2* relaxivities of transferrin and ferritin (Eq.* S11*, similar to* Figure 4c*). Rearranging the model allows for the MRI prediction of the transferrin fraction (y-axis) for younger and older subjects in different brain regions. There are no free parameters in this model. The x-axis shows the transferrin fraction measured postmortem*[5,7,9]*. MAE=mean absolute error. The prediction in the globus pallidus (red) is negative and is very different from the literature value, especially for young subjects.*

## Supplementary Figure 38

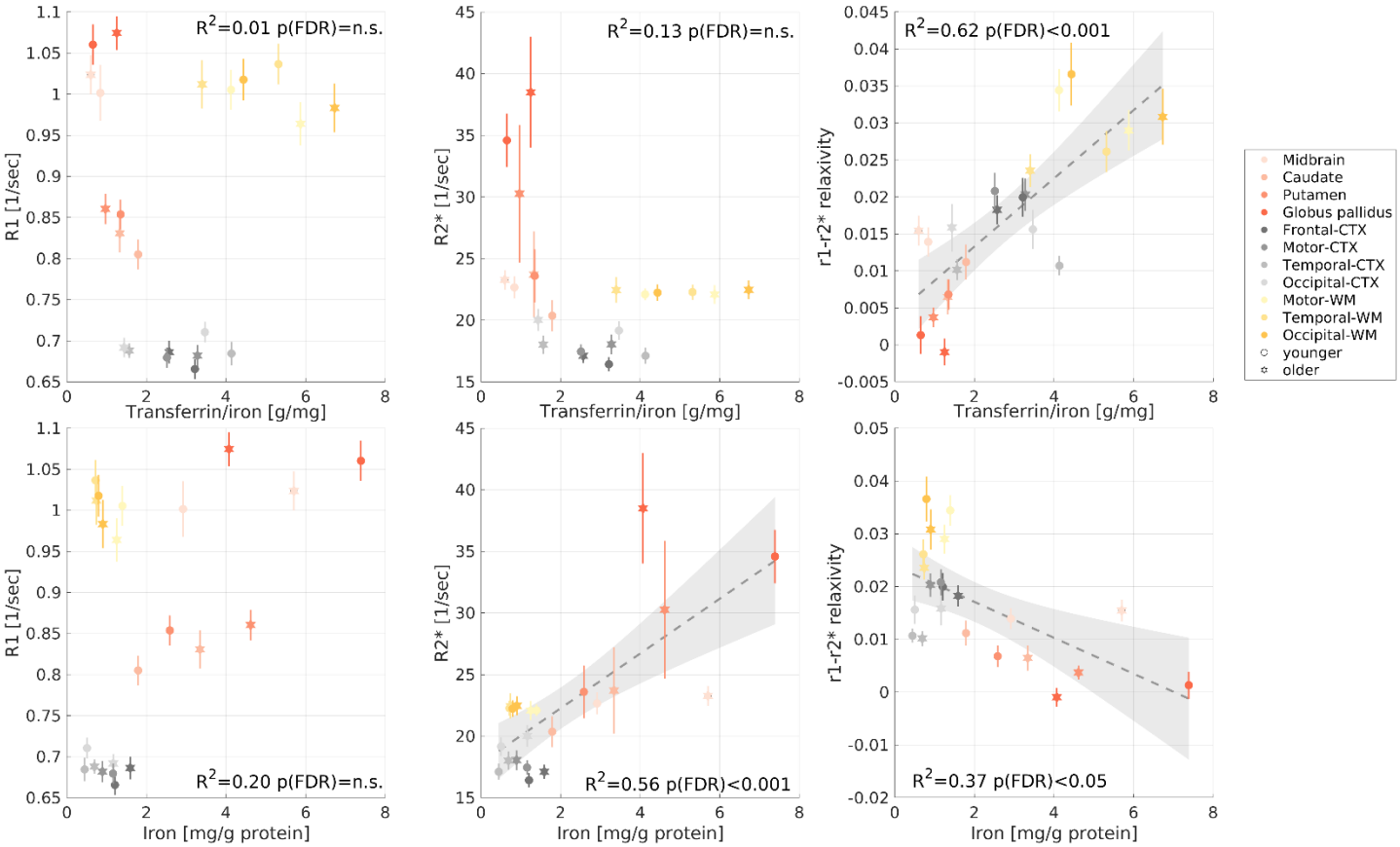


***Sup. Figure 38: The correlations of MRI parameters with the iron environment when including the pallidum. (a)*** *Replication of* Figure 4b *including the globus pallidus (red). The transferrin/iron ratio (postmortem, from the literature[5,7,9]) in different brain regions of younger (aged 27-64 years, N>=7) and older (aged 65-88 years, N>=8) subjects vs. R1, R2* and the r1-r2* relaxivity measured in vivo across younger (aged 23-63 years, N =26) and older (aged 65-77 years, N=13) subjects (different marker shapes) in 11 brain regions (different colors), including the pallidum. Only the r1-r2* relaxivity shows a statistically significant correlation with transferrin/iron ratio, even when including the pallidum.* ***(b)*** *Replication of* ***Sup. Figure 16*** *including the pallidus. Both R2* and the r1-r2* relaxivity are significantly correlated with iron concentration. However, the correlation with the r1-r2* relaxivity does not survive after the removal of the outlier values of the pallidum (****Sup. Figure 16****).*

## Supplementary Figure 39

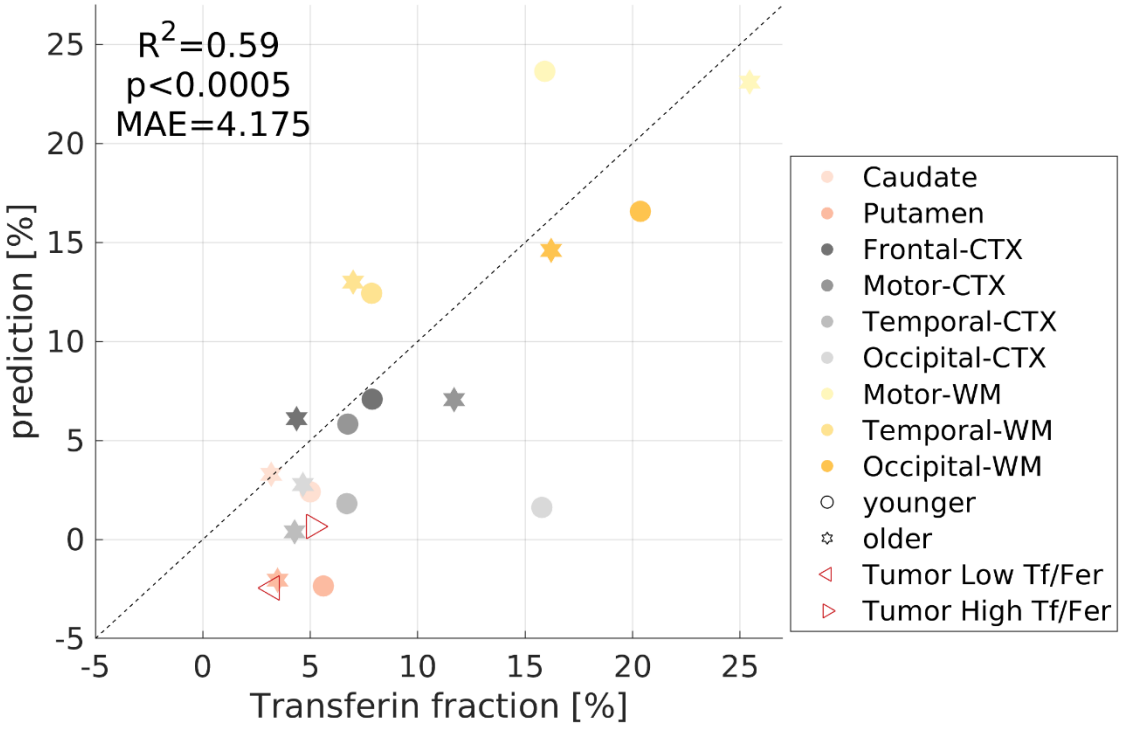


***Sup. Figure 39: Replication of the transferrin fraction prediction on an independent MRI dataset.*** *The fully-constrained model presented in* Figure 4c *predicts the fractions of iron-binding proteins on a second, independent MRI dataset, consisting of meningioma patients. The measured r1-r2* relaxivity in each brain area was modeled as a weighted sum of the r1-r2* relaxivities of transferrin (Tf) and ferritin (Fer), both of which were estimated in liposomal phantoms. The Tf and Fer fractions sum to one. Rearranging the model allows for the MRI prediction of the transferrin fraction (Tf/(Tf+Fer), y-axis) for younger (<64) and older subjects (different symbols) in 10 brain regions (different colors). There are no free parameters. In the x-axis is the Tf fraction as reported in postmortem analyses*[5,7,9]*. MAE=mean absolute error. The MRI predictions for the tumors with low and high transferrin/ferritin ratios are based on the r1-r2* relaxivities of the two groups as shown in* Figure 4a*. As the western-blot analysis of the two groups does not provide the Tf/(Tf+Fer) fraction exactly, the transferrin fraction in the x-axis for these two groups is estimated based on the linear fit of the other data points. Tumors with higher Tr/Fer values (based on western-blot analysis) are predicted (based on the r1-r2* relaxivities) to have higher Tf/(Tf+Fer) values. This result provides additional evidence for the ability of our MRI biophysical model to predict the transferrin-to-ferritin fraction in tissue.*

# Supplementary methods

## R1-MTV dependency computation for phantoms.

We computed the linear dependency of R1 on MTV across samples with varying iron-binding protein concentrations and liposomal fractions[68]. This process was implemented in MATLAB. We extracted the MTV values from all voxels and pooled them into 12 bins spaced equally between 0.05 and 0.40. This was done so that the linear fit would not be heavily affected by the density of the samples in different MTV regimes. The median MTV of each bin was computed, along with the median R1. We fitted the following linear model across samples:

$$R1 = a * MTV + b$$

The slope of this linear model ($a$) represents the R1-MTV dependency. $b$ is constant.